

Control of noise-induced spatio-temporal dynamics in superlattices

von Diplom-Physikerin
Ioanna Chitzanidi
aus Athen

der Fakultät II – Mathematik und Naturwissenschaften
der Technischen Universität Berlin
zur Erlangung des akademischen Grades

Doktor der Naturwissenschaften,
Doctor rerum naturalium

genehmigte Dissertation

Promotionsausschuss:

Vorsitzender: Prof. Dr. C. Thomsen
Berichter/Gutachter: Prof. Dr. E. Schöll, PhD
Berichter/Gutachter: Prof. Dr. H. Engel

Tag der wissenschaftlichen Aussprache: 10. Januar 2008

Berlin 2008
D 83

Zusammenfassung

Die vorliegende Arbeit behandelt den Einfluss von Gauß'schem weißen Rauschen und zeitverzögerter Rückkopplungskontrolle auf den nichtlinearen Transport in einem Halbleiterübergitter. Die Systemparameter sind auf zwei verschiedene dynamische Bereiche beschränkt, wobei der Übergang von stationären zu laufenden Fronten der Elektronendichte entweder durch eine Hopf-Bifurkation oder eine globale Sattel-Knoten-Bifurkation auf einem Grenzyklus stattfindet.

Wir zeigen, dass Rauschen Schwingungen der Stromdichte induziert, die mit Frontbewegungen in der Umgebung um den Fixpunkt unterhalb der Hopf-Bifurkation einhergehen. Während die deterministischen Zeitskalen nur gering vom Rauschen beeinflusst werden, nimmt die Regularität dieser Oszillationen mit steigender Rauschintensität ab. Dicht unterhalb der globalen Bifurkation wird die Dynamik des Systems hingegen stark durch das Rauschen beeinflusst. Es findet eine globale Änderung statt, die bewirkt, dass Ladungsträgerfronten durch das gesamte Bauteil laufen. In diesem Bereich ist das System anregbar. Wir bestätigen das Auftreten von Kohärenzresonanz, d. h. bei optimaler Wahl der Rauschintensität wird die Regularität maximal. Die charakteristischen Zeitskalen des Systems zeigen eine starke Abhängigkeit vom Rauschen, was die zugrunde liegende deterministische Konstellation widerspiegelt.

Des Weiteren wenden wir eine zeitverzögerte Rückkopplungskontrolle an, die bisher hauptsächlich für die Kontrolle von rein zeitlichen, rauschinduzierten Oszillationen genutzt wurde. Wir zeigen, dass Kontrolle die Regularität von raumzeitlichen Mustern nicht nur verstärken oder abschwächen kann, sondern mit variierender Verzögerungszeit auch die Manipulation der Zeitskalen in beiden untersuchten Parameterbereichen ermöglicht. Durch die Wirkung der Kontrolle im rein deterministischen Modell ergeben sich Bifurkationen, die allein von der Zeitverzögerung induziert werden.

Schließlich verwenden wir ein generisches Modell für eine Sattel-Knoten-Bifurkation, um dessen qualitatives Verhalten unter dem Einfluss von Rauschen und zeitverzögerter Rückkopplung mit dem des Übergittermodells zu vergleichen. Wir bestätigen das Auftreten der grundlegenden kontrollinduzierten Dynamik in beiden

Systemen. Weitere Untersuchungen des kontrollierten generischen Modells offenbaren die Multistabilität zwischen unterschiedlichen periodischen Orbits und dem Fixpunkt. Entsprechend Shilnikovs Theorie treten homokline Bifurkationen, Periodenverdopplung und Sattel-Knoten-Bifurkation von Grenzzyklen auf.

Abstract

The effect of random fluctuations and time-delayed feedback control on nonlinear transport in a semiconductor superlattice is studied. The system's parameters are fixed in the two different dynamical regimes where the transition from stationary to moving electron charge density fronts takes place either through a Hopf bifurcation or a global bifurcation, namely a saddle-node bifurcation on a limit cycle.

It is shown that noise can induce current density oscillations which are associated with localized front motion around the stable fixed point below the Hopf bifurcation. The regularity of the noise-induced motion decreases with increasing noise level, while the deterministic time scales of the system are robust against the noise. In the vicinity of the global bifurcation noise has a dramatic effect inducing a global change in the dynamics of the system forcing stationary fronts to move through the entire device. In this regime, the system is excitable and we are therefore able to demonstrate the effect of coherence resonance in our model, i.e. there is an optimal level of noise at which the regularity of front motion is enhanced. The characteristic time scales of the system show a strong dependence on the noise level reflecting the underlying deterministic configuration.

Furthermore, we apply a time-delayed feedback control scheme that was previously used to control purely temporal oscillations induced by noise. We show that control can not only enhance or deteriorate the regularity of stochastic spatio-temporal patterns but also allows for the manipulation of the system's time scales with varying time delay, in both dynamical regimes. Moreover, the effect of control on the pure deterministic model uncovers delay-induced bifurcation scenarios which result in the birth of oscillations that are mediated by the addition of noise.

Finally, we employ a prototype (generic) model for a saddle-node bifurcation on a limit cycle and compare the qualitative behaviour under noise and delay to the superlattice model. We manage to verify the basic delay-induced dynamics in both systems. By further investigation of the controlled generic model we are able to reveal delay-induced multistability of periodic orbits and the fixed point. Homoclinic bifurcations, period-doubling and saddle-node bifurcations of limit cycles are found in accordance with Shilnikov's theorems.

Contents

1	Introduction	1
2	The superlattice model	5
2.1	The sequential tunneling model	5
2.2	The superlattice parameters	8
2.3	The model equations	9
3	Deterministic dynamics	13
3.1	Stationary fronts	13
3.2	Moving fronts	14
3.3	The role of the boundary	15
3.4	Stationary to moving fronts: Bifurcation scenarios	16
3.4.1	The (σ, U) plane	17
3.4.2	Hopf bifurcation	18
3.4.3	Saddle-node bifurcation on a limit cycle: <i>SNIPER</i>	20
4	Noise-induced dynamics	29
4.1	Noise in the superlattice model	30
4.2	Regime I: Below the Hopf bifurcation	30
4.2.1	Noise-induced current oscillations	32
4.2.2	Effect of noise on the coherence	32
4.2.3	Effect of noise on the time scales	37
4.3	Regime II: Below the <i>SNIPER</i>	37
4.3.1	Noise-induced front motion	37
4.3.2	Coherence Resonance	39
4.3.3	Coherence Resonance in the superlattice	39
4.3.4	Application as noise sensor	44
4.4	Comparison of the results obtained in Regimes I and II	44

5	Control of noise-induced dynamics	47
5.1	Time-delayed feedback	47
5.2	Regime I: Below the Hopf bifurcation	49
5.2.1	Delay-induced Hopf instability	50
5.2.2	Influence of the control on the coherence	51
5.2.3	Control of time scales	56
5.3	Regime II: Below the <i>SNIPER</i>	56
5.3.1	Delay-induced homoclinic bifurcation	57
5.3.2	Influence of the control on the coherence	60
5.3.3	Control of the time scales	62
6	A generic model for excitability	67
6.1	Global bifurcations	67
6.1.1	Saddle-node bifurcation on a limit cycle	67
6.1.2	Homoclinic Bifurcation	68
6.2	Other bifurcations of periodic orbits	69
6.2.1	Saddle-node bifurcations of cycles	70
6.2.2	Period-doubling bifurcation of cycles	70
6.3	A paradigm for the <i>SNIPER</i>	71
6.3.1	Excitability and the influence of noise	75
6.3.2	Connection to the superlattice	78
7	Delay-induced multistability in the generic model	79
7.1	The delay equations	80
7.1.1	Linear stability analysis	80
7.2	Global bifurcation analysis	82
7.2.1	Delay-induced homoclinic bifurcation	82
7.2.2	The role of the saddle quantity	85
7.3	Delay-induced multistability	87
7.3.1	Negative saddle quantity $\sigma_0 < 0$	88
7.3.2	Positive saddle-quantity $\sigma_0 > 0$	88
7.4	Summary and comparison to the superlattice	90
8	Conclusions and outlook	93
	Acknowledgments	97
	List of Figures	99
	Bibliography	103

1 Introduction

Semiconductor nanostructures represent prominent examples of nonlinear dynamic systems which exhibit a variety of complex spatio-temporal patterns [Sch87, Sch01]. A superlattice is such a nanostructure which consists of alternating layers of two semiconductor materials with different band gaps. This leads to (periodic) spatial modulations of the conduction and valence band of the material, and thus forms an energy band scheme consisting of a periodic sequence of potential barriers and quantum wells.

Those structures can be tailored by modern epitaxial growth technologies with high precision on a nanometer scale. If the potential barriers are sufficiently thick, the electrons are localized in the individual quantum wells. In such a situation the superlattice can be treated as a series of weakly coupled quantum wells, and sequential resonant tunneling of electrons between different wells leads to strongly nonlinear charge transport phenomena, if a dc voltage is applied across the superlattice [Wac02, Bon02, Bon05, Sch03c]. For instance, negative differential conductance can appear [Esa70]. Thus, semiconductor superlattices can be used as generators of current oscillations, whose frequency depends on the parameters of the superlattice structure and the applied voltage, and thus, can be varied in a wide range from some hundred kHz [Cad94, Kas95, Hof96, Wan00] to hundreds of GHz [Sch99h], which makes this system very promising for practical applications.

On the other hand, the inherent nonlinearity gives rise to complex spatio-temporal dynamics of the charge density and the field distribution within the device, including the formation of travelling charge accumulation and depletion fronts and field domains associated with current oscillations. The interaction between multiple moving fronts may lead to sophisticated self-organized patterns, which are typical of a large variety of spatially extended systems [Kap95a, Ama03, Sco04]. Even chaotic scenarios have been found experimentally [Zha96, Luo98b] and described theoretically in periodically driven [Bul95] as well as in undriven superlattices [Ama02a].

Another source of irregularity, apart from deterministic chaotic motion, is noise. In reality any physical system is inevitably influenced by random fluctuations. In

semiconductor nanostructures, in particular, microscopic noise sources affect the charge transport [Bla00, Son03, Zha00, Kie03b, Kie07b]. The noise arises naturally, due to the probabilistic nature of the tunneling current, thermal fluctuations, etc.

In the past it was believed that noise plays a destructive role deteriorating a system's performance. However, theoretical and experimental research has recently shown that noise can have surprisingly constructive effects in many physical systems. Already since the early 1980's, the counterintuitive fact that noise can help rather than hinder the performance of a nonlinear system is known. The phenomena of stochastic [Ben81, Nic81] and coherence [Hu93a, Pik97] resonance have well been established and verified in numerous models both theoretically and experimentally [Gam98, Ani99, Lin04]. In particular, an optimal noise level may give rise to ordered behavior and even produce new dynamical states.

Moreover, for a large class of extended systems of reaction-diffusion type it has been shown that noise can induce quite coherent dynamical space-time patterns [Gar99, Sag07]. It was shown, for instance, that random fluctuations are able to induce coherent patterns in extended media, to maintain existing patterns [Alo01], and even to support wave propagation [Kad98]. Noise-induced patterns were also found in another semiconductor nanostructure, namely a double barrier resonant tunneling diode described by a reaction-diffusion model for the current density distribution [Ste05]. In spite of considerable progress on a fundamental level, useful applications of noise-induced phenomena in technologically relevant devices like semiconductor devices, are still scarce.

An essential issue that arises in such systems is how one can deliberately influence and control the regularity of the noise-induced dynamics. Recently it was shown for two general classes of simple nonlinear systems with temporal degrees of freedom only, that the coherence properties and the time scales of noise-induced oscillations can be changed by applying a time-delayed feedback [Jan03, Bal04, Sch04b] in the form which was introduced earlier by Pyragas [Pyr92] for chaos control of deterministic dynamics. The Pyragas scheme is an alternative to the famous OGY method developed earlier by Ott, Grebogi and Yorke [Ott90]. The idea is to achieve stabilization of unstable periodic orbits (UPOs) by adding, to a chaotic system, a control force in the form of the difference between a system variable and its delayed counterpart. In [Jan03, Bal04, Sch04b, Pom05a, Pom07] noisy temporal motion was considered within the example of a Van-der-Pol oscillator, i. e. a system close to but below a Hopf bifurcation, and in a FitzHugh-Nagumo model [Jan03, Bal04, Hau06, Pra07], i. e. an excitable system.

Apart from the deliberate application of a control force to a system in order to be able to manipulate its behaviour, delay may also enter naturally in a system's dynamics. Typical examples of such systems are lasers where the delay enters

through the coupling to external cavities (optical feedback) [Sch06a, Tro06] and neurons, where the signal propagation yields a delay time [Car88, Man91].

Moreover, the interest in time-delayed feedback lies also on the mathematical aspect. Delay differential equations require the use of tools other than those used to handle ordinary differential equations. The delay renders the system infinite-dimensional and the interplay with nonlinearity uncovers complex dynamic behaviour. In this spirit, elegant analytical theories have been developed [Jus97, Ama05, Fie07]. Another issue is that time-delayed feedback may not only be used for controlling a system but also for creating new dynamics. Delay-induced multistability was already predicted in the first paper by Pyragas [Pyr92]. Nevertheless, the investigation of delay-induced bifurcations and multistability is still a growing field [Xu04, Bal05, Ste05a].

In this work we consider the effect of random fluctuations on a semiconductor superlattice. Note that the modelling of noise is based on a classical approach, with Gaussian white noise sources added to the system yielding, thus, Langevin-type equations. We show that noise is able to induce oscillations and front motion when the system is prepared in two different dynamical regimes, namely in the vicinity of a Hopf bifurcation and near a global bifurcation where the system is excitable.

The next task is to apply a time-delayed feedback force and study to what extent control can affect the noise-induced dynamics in both dynamical regimes. For deeper understanding of the observed behaviour in the excitable regime, we reduce the system's dynamics in order to obtain some universal qualitative characteristics. We do that by introducing a generic model undergoing the same global bifurcation and study it both with and without control.

This thesis is organized as follows: The sequential tunneling approach for the superlattice model is briefly introduced in Chapter 2. In Chapter 3 we look at the deterministic dynamics of the system and, in particular, study the two bifurcation scenarios that govern the transition from stationary to moving fronts. We provide both a dynamical description and a physical interpretation for the observed dynamics and its dependence on the bifurcation parameters. In Chapter 4, the influence of stochastic fluctuations in the two dynamical regimes presented in Chapter 3 is considered. Properties such as temporal coherence and time scales are quantified in dependence on the noise level. The effect of a time-delayed feedback force on the noisy dynamics is investigated in Chapter 5. In addition, the role of control on the purely deterministic system is examined. In Chapter 6 we employ the generic simple model exhibiting the same global bifurcation found in the superlattice model. We present its basic dynamical features and motivate the connection to the corresponding dynamics of the superlattice. The time-delayed

version of the generic model is studied in Chapter 7 and direct comparison to the superlattice is made. Finally, in Chapter 8 we give a brief summary and an outlook for possible further research.

2 The superlattice model

First suggested by Esaki and Tsu in 1970 [Esa70], the semiconductor superlattice is a nanostructure which typically consists of alternating layers of two semiconductor materials with different band gaps, such as *AlAs* and *GaAs* or *Al_xGa_{1-x}As* and *GaAs*. This leads to periodic spatial modulations of the conduction and valence band of the material, and thus forms an energy band scheme consisting of a periodic sequence of potential barriers and quantum wells (see Fig. 2.1). *GaAs*, having a lower conduction band edge, will act as the quantum well, whereas *AlAs* acts as the quantum barrier, since its conduction band edge lies higher. Those structures can be tailored by modern epitaxial growth technologies with high precision on a nanometer scale [Gra95d]. The analogy to the atomic lattice, albeit with a much larger period, yielded the name “superlattice”.

The superlattice is a periodic structure and therefore the energy spectrum may be calculated analogously to the Kronig-Penney model [Kro31] resulting in the appearance of energy bands (instead of discrete levels characteristic for atoms and molecules) and energy gaps. The corresponding eigenfunctions are the Bloch functions characterized by the band index ν and the Bloch vector \mathbf{k} , which is restricted to the Brillouin zone $-\pi/d \leq k \leq \pi/d$, where d is the superlattice period. This range is much smaller than the Brillouin zone for the atomic lattice with lattice constant a_L , since $d \gg a_L$, and therefore the new bands are called minibands. The external voltage drop U applied perpendicularly to the quantum well layers gives rise to vertical electron current in the z -direction.

2.1 The sequential tunneling model

In this thesis we are interested in the superlattice from the viewpoint of a nonlinear dynamical system. In the following, however, we will take a brief look into the microscopic model.

Assuming ideal interfaces, the semiconductor superlattice is translational invariant in the x - and y - direction perpendicular to the growth direction. In each quantum

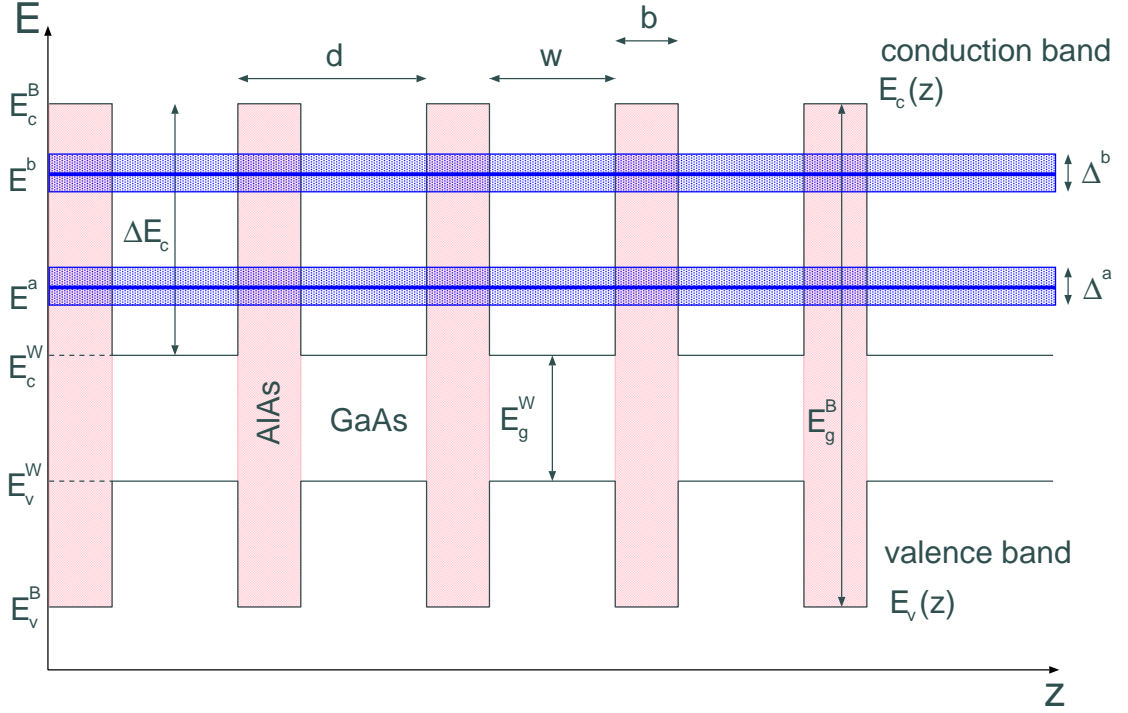


Figure 2.1: Schematic band structure of the conduction band $E_c(z)$ and the valence band $E_v(z)$ in an *AlAs/GaAs* superlattice with barrier width b , well width w , and period $d = b + w$. $E_{c/v}^B$ and $E_{c/v}^W$ are the maximum/minimum energies of the conduction band and valence band for the barrier (B) and well (W) material, respectively. E_g^B and E_g^W are the respective energy gaps between valence and conduction band. $\Delta E_c = E_c^B - E_c^W$ is the difference in the conduction band energy of the well and the barrier material. Δ^a and Δ^b denote the widths of the first and the second minibands, which are located at the energies E^a and E^b , respectively. (After Figure 2.1 in [Ama03c]).

well m we have a basis set of wave functions. The solutions of the wave equation for the x - y plane are given by plane waves $e^{i\mathbf{k}\mathbf{r}}$ (\mathbf{k} and \mathbf{r} being the vectors within the x - y plane). In the z -direction we have a periodicity of period d leading to energy states $E_{\mathbf{k}}^\nu$ characterized by the miniband index ν and the vector \mathbf{k} . The energies as well as the Bloch functions $\phi_{\mathbf{k}}^\nu(z)$ can be calculated analogously to the Kronig-Penney model. From the Bloch functions $\phi_{\mathbf{k}}^\nu(z)$ the Wannier functions $\Psi^\nu(z - md)$ [Wan37] are defined, where ν is the miniband index and m is the number of the well at which the Wannier function is localized. One-dimensional Wannier functions serve to describe localized electrons.

Here we consider a superlattice with thick barriers (i. e. narrow minibands). Thus we obtain a series of weakly coupled quantum wells with localized eigenstates. When a voltage is applied to the device, tunneling processes through the barriers are possible and the electron transport results from sequential tunneling from one well to the next. Other approaches for superlattice transport include miniband conduction and Wannier-Stark hopping. For a thorough review see [Wac02]. The electric field F_m caused by the applied voltage creates a shift of the miniband levels $E_m^\nu + eF_m d = E_{m+1}^\nu$. For aligned miniband levels ($E_m^\nu = E_{m+1}^\mu$) in two neighbouring wells, resonant tunneling is possible. The tunneling current $J_{m \rightarrow m+1}$ is then calculated by a Fermi's Golden Rule-like expression [Wac98]:

$$\begin{aligned}
 J_{m \rightarrow m+1}(F_m, n_m, n_{m+1}) &= \sum_{\nu} \frac{e}{\hbar} |H_{m,m+1}^{1,\nu}|^2 \\
 &\times \frac{\Gamma^1 + \Gamma^\nu}{(E^\nu - E^1 - eF_m d)^2 + \left(\frac{\Gamma^1 + \Gamma^\nu}{2}\right)^2} \\
 &\times \left\{ n_m - \rho_0 k_B T \ln \left[\left(e^{\frac{n_{m+1}}{\rho_0 k_B T}} - 1 \right) e^{-\frac{eF_m d}{k_B T}} + 1 \right] \right\},
 \end{aligned} \tag{2.1}$$

where $e < 0$ is the charge of the electron, n_m is the two-dimensional electron density in well m , F_m is the electric field between the wells m and $m + 1$, E^ν is the energy level of the miniband ν , T is the temperature, $\rho_0 = m^*/\hbar^2\pi$ is the two-dimensional electron density of states, and m^* is the effective electron mass. The matrix elements $H_{m,m+1}^{1,\nu}$ between the Wannier state 1 in well m and ν in well $m + 1$ are calculated numerically for a given superlattice from the Wannier functions [Wac98]. Γ^ν is the scattering-induced broadening of the energy level ν . We restrict ourselves to the lowest two levels $\nu = a, b$.

For the homogeneous case, i. e. $n_m = n_{m+1}$, shown in Fig. 2.2, the tunneling current density as a function of the electric field, $J(F)$, exhibits a strongly nonlinear dependence. If there is no electric field, naturally no current can flow through the device. With increasing field the current density rises achieving a first local maximum which corresponds to electron tunneling between equal energy levels. This local peak is a result of the competition between two opposing effects: The smaller the field, the better the alignment between the subbands in the two quantum wells is. On the other hand, the driving force is stronger for higher field. For further increase of the field, there is no alignment of the subbands and electron transport becomes very inefficient. The current, thus, decreases and the current-field characteristic exhibits a drop. At higher field (the superlattice potential is tilted), however, we can have the situation that the ground level in one well is aligned with the second level in the neighbouring well and the relation $eFd = \Delta E$ is satisfied, ΔE being the intersubband spacing. Resonant tunneling then produces a large

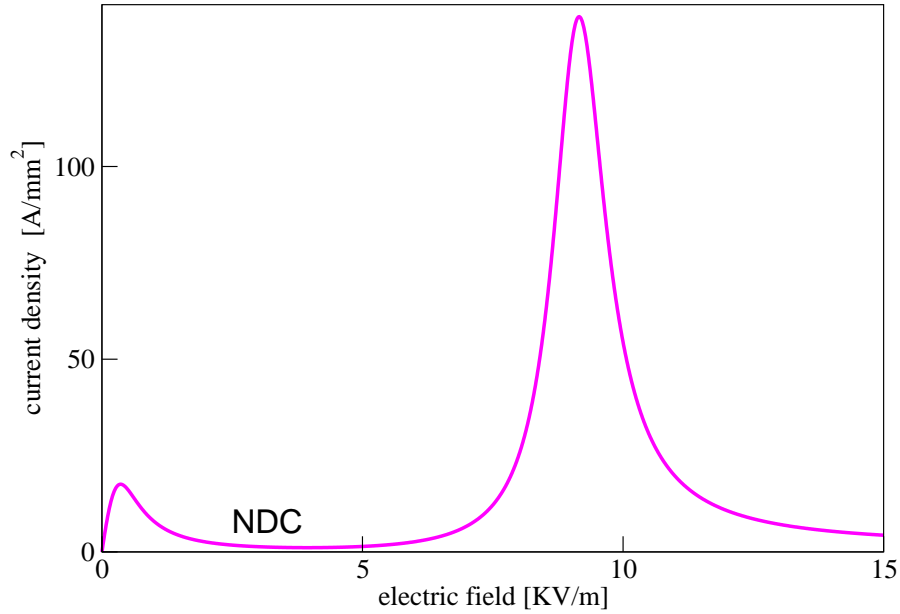


Figure 2.2: Homogeneous current-field characteristic of the superlattice calculated from Eq. (2.1). Parameters as in Table 2.1. NDC marks the region of negative differential conductivity.

current and transport is accomplished. Off-resonance settings lead to negative differential conductivity (NDC).

The $J(F)$ characteristic (Fig. 2.2) describes the local transport properties of the superlattice. It is N -shaped and there is a region of NDC in which an increase in the electric field leads to a decrease of the electric current. This strongly nonlinear behaviour may lead to instabilities.

2.2 The superlattice parameters

The superlattice studied here has been treated in earlier theoretical works including [Sch02r, Kil03, Ama03c]. The parameters of the model are listed in Table 2.1. The use of these parameters is motivated by real experiments on lattices of the same number of wells [Zeu96a] or smaller samples [Kas95, Rog02a].

Parameter	Notation and Units	Value
Number of wells	N	100
2D doping density	$N_D^{2D} [10^9 cm^{-2}]$	100
3D doping density	$N_D^{3D} [10^{15} cm^{-3}]$	77
Barrier width	$b [nm]$	5.0
Well width	$w [nm]$	8.0
Superlattice period	$d [nm]$	13
Temperature	$T [K]$	20
Scattering width	$\Gamma^a = \Gamma^b [meV]$	8.0
Matrix element for transition $a \rightarrow a$	$H_{m \rightarrow m+1}^{a,a} [meV]$	-0.688
Matrix element for transition $b \rightarrow b$	$H_{m \rightarrow m+1}^{b,b} [meV]$	1.263
Matrix element for transition $a \rightarrow b$	$H_{m \rightarrow m+1}^{a,b} [meV]$	$-eF_m \times 0.0127m$
Energy of miniband a	$E^a [meV]$	41.5
Energy of miniband b	$E^b [meV]$	160
Effective electron mass in <i>GaAs</i>	$m_{GaAs}^* [m_e]$	0.067
Effective electron mass in <i>AlAs</i>	$m_{AlAs}^* [m_e]$	0.15
Relative permittivity of <i>GaAs</i>	ϵ_r	13.18

Table 2.1: Parameters of superlattice similar to experimental lattice in [Zeu96a], but with a different doping density.

Symbol	Description
U	Voltage across the superlattice
n_m	Electron density in well m
$J_{m \rightarrow m+1}$	Current density flowing from well m to $m + 1$
J	Global current density
F_m	Electric field across barrier m
F_0	Electric field at emitter
σ	Conductivity at emitter

Table 2.2: List of symbols used throughout this work.

2.3 The model equations

As dynamical variable we consider the electron densities in each well n_m , the evolution of which is given by the continuity equation:

$$e \frac{dn_m}{dt} = J_{m-1 \rightarrow m} - J_{m \rightarrow m+1} \quad \text{for } m = 1, \dots, N, \quad (2.2)$$

with $[n] = cm^{-2}$ and $[J] = A/cm^2$. We thus obtain N coupled ordinary differential equations (ODEs) with right hand sides containing complicated nonlinear dependencies on the electron densities n_m and the fields F_m , according to Eq. (2.1). The electron densities and the electric fields are coupled by the following discrete Poisson equation:

$$\epsilon_r \epsilon_0 (F_m - F_{m-1}) = e(n_m - N_D) \quad \text{for } m = 1, \dots, N, \quad (2.3)$$

where ϵ_r and ϵ_0 are the relative and absolute permittivities, $e < 0$ is the electron charge, N_D is the donor density, and F_0 and F_N are the fields at the emitter and collector barrier, respectively. Equation (2.3) is derived by considering Gauss's law in the integral formulation, with the integration volume being a well, modelled by an infinite layer with finite width w . The applied voltage between emitter and collector gives rise to a global constraint

$$U = - \sum_{m=0}^N F_m d, \quad (2.4)$$

where d is the superlattice period. The fields across the barriers must, therefore, be distributed such, that the above sum remains constant. In the chapters to come we will see how the voltage U plays a decisive role in the observed dynamics.

Boundary conditions

Real contacts consist of a number of layers differing in composition and doping. A microscopic contact modeling would, however, be a complicated task. For our purpose it is sufficient to use simple Ohmic boundary conditions:

$$J_{0 \rightarrow 1} = \sigma F_0 \quad (2.5)$$

$$J_{N \rightarrow N+1} = \sigma F_N \frac{n_N}{N_D}, \quad (2.6)$$

where σ is the Ohmic contact conductivity, and the factor n_N/N_D is introduced in order to avoid negative electron densities at the collector. Other boundary conditions (Dirichlet and Neumann) have been used in earlier works [Pre94, Wac95c, Sch96a, Sch96b, Pat98]. An exponential boundary current density of the form $J_{0 \rightarrow 1} = a \exp(bF_0)$ was considered in [Ama03a]. There it was found that for suitable parameters a and b the dynamical behaviour of the superlattice is equivalent to that under Ohmic boundary currents.

Together with the voltage U , the boundary current $J_{0 \rightarrow 1}$ (and therefore the contact conductivity σ) will prove to strongly influence the system's dynamics. From

the experimental aspect the voltage is easily accessible and tunable as it is applied externally. The conductivity can be adjusted by changing the thickness of the contact, the doping level or the temperature [Bon00, Rog01]. The contact conductivity may also be adjusted optically by illumination [Luo99].

The total current through the device is given by the sum over all local current densities:

$$J = \frac{1}{N+1} \sum_{m=0}^N J_{m \rightarrow m+1}. \quad (2.7)$$

From Eq. (2.3) one can express the field across each barrier in the following way:

$$\begin{aligned} F_1 &= \frac{e}{\epsilon}(n_1 - N_D) + F_0 \\ F_2 &= \frac{e}{\epsilon}(n_2 - N_D) + \frac{e}{\epsilon}(n_1 - N_D) + F_0 \\ &\dots \\ F_m &= \frac{e}{\epsilon} \sum_{k=1}^m (n_k - N_D) + F_0, \end{aligned}$$

with $\epsilon = \epsilon_0 \epsilon_r$, obtaining, thus, a recursive formula for the fields as a function of the electron densities. The global constraint Eq. (2.4) requires the sum of all fields to equal $-U/d$. Applying this to the above recursive formula for F_m we gain an expression for F_0 :

$$F_0 = \frac{1}{N+1} \left(-\frac{U}{d} - \frac{e}{\epsilon} \sum_{k=1}^N (N-k+1)(n_k - N_D) \right). \quad (2.8)$$

Thus, the fields F_m with $m = 0, \dots, N$, can be eliminated from the dynamic equations Eq. (2.2). The numerical integration of the system of N ODEs (Eq. (2.2)) requires an initial electron density distribution (n_1, n_2, \dots, n_N) (as default taken to be equal to the doping density N_D , i.e. a homogeneous superlattice). The right hand sides of the continuity equations (Eq. (2.2)) depend on the electron densities and the fields, which in turn are also functions of the electron densities. The field across each barrier, F_m , contains the term F_0 , which is determined by the electron densities and the voltage according to Eq. (2.8) derived above. The last two ingredients in order to fully obtain the right hand sides of our system's equations are the boundary currents, which require the knowledge of the contact conductivity σ . We then are able to simulate the system.

For an extension of the model to two spatial dimensions including lateral diffusion see [Ama05a].

3 Deterministic dynamics

In the regime of negative differential conductivity (NDC), an increase of the electric field strength leads to a decrease of the current. That means that electrons can enter the superlattice in the low-field region faster than they can leave it through the high field region. This results in spontaneous accumulation of charge in the superlattice. The branch of NDC is unstable and therefore the system, when slightly perturbed (due to impurities), will jump to either lower or upper branch of positive differential conductivity (PDC). The lower and upper branch of the PDC regime associates the NDC current density with a low- and high-field value, respectively (Fig. 2.2). This is the mechanism of field domain formation.

Low-field domains form when transport from the ground level of one well to the ground level in the adjacent well takes place. Transport between the ground level of one quantum well to the upper level in the next well is associated with high-field domains. From the Poisson equation (2.3) it is clear how the difference in the field between two wells is connected to charge accumulation or depletion. This charge accumulation / depletion forms the boundary between low-/ high- and high-/low-field, which is nothing but a front.

Fronts may either be stationary, oscillating or even chaotic, depending on the applied voltage U and the contact conductivity σ [Ama03, Ama04, Ama02a]. In [Ama03, Ama04] a reduced model for the superlattice was developed to explain the front dynamics. Here we will briefly review the cases of stationary and moving fronts and focus more on the transition between those two dynamical scenarios.

3.1 Stationary fronts

For certain combinations of the contact conductivity and the applied voltage, stationary fronts are observed. They correspond to a constant stationary current flowing through the device. The position of the front (the front extends over two or three wells) in the device is determined by σ and U .

Assume that for a given choice of parameters an accumulation front essentially is

localized at well m separating a region of high- and low-field, above and below well m , respectively. With increase of the voltage this front will move to well $m+1$. Due to the global constraint, the high-field domain expands and moves one well further “dragging” the front with it. Plotting the global current density over the voltage, we obtain a typical current-voltage sawtooth characteristic [Pre94, Kas94, Ama01] in which the number of branches is approximately equal to the number of wells in the superlattice. Up- and down-sweep of the voltage produce a different sawtooth characteristic resulting, thus, in hysteresis. In addition, the multi-branched I - V curve is responsible for multistability. Finally, one should note that the occurrence of stationary field domains is a result of the discreteness of the superlattice.

3.2 Moving fronts

For other choice of boundary conditions oscillatory behavior may be obtained, where front motion and associated current oscillations occur. The fronts are generated at the emitter and move through the device until they reach the collector.

A single front is a monopole, a pair of one accumulation and one depletion front form a dipole, whereas two accumulation / depletion fronts and one depletion / accumulation front form a tripole. In Fig. 3.1 one can see the electron charge density in space and time (top panel), the corresponding electric field evolution (middle panel) and the global current density time series (bottom panel), for certain parameter values. At the beginning, there is a dipole of one accumulation and one depletion front moving with equal velocities (top panel). The region between the depletion front and the accumulation front corresponds to a high-field domain, shaded by red colour in the middle panel. In the bottom panel, the current (neglecting the high-frequency small-amplitude oscillations due to well-to-well hopping) is constant during the lifetime of the dipole. When the depletion front reaches the collector and vanishes, there is only one accumulation front in the device (a monopole). The monopole slows down while the global current increases. When a certain maximum threshold is achieved, the accumulation front disappears and at the same time a new dipole is generated at the emitter. The same scenario is then repeated over and over.

The velocities of accumulation and depletion fronts may, in general, differ. Their dependence on the total current density has been studied in depth and explains the relevance between the spatio-temporal charge density propagation and the global current density oscillations in time [Ama02, Ama02a, Ama04]. The mechanism of the generation of a dipole at the emitter has also been investigated in detail [Ama02a]. The role of the critical current density value J_c will be discussed next.

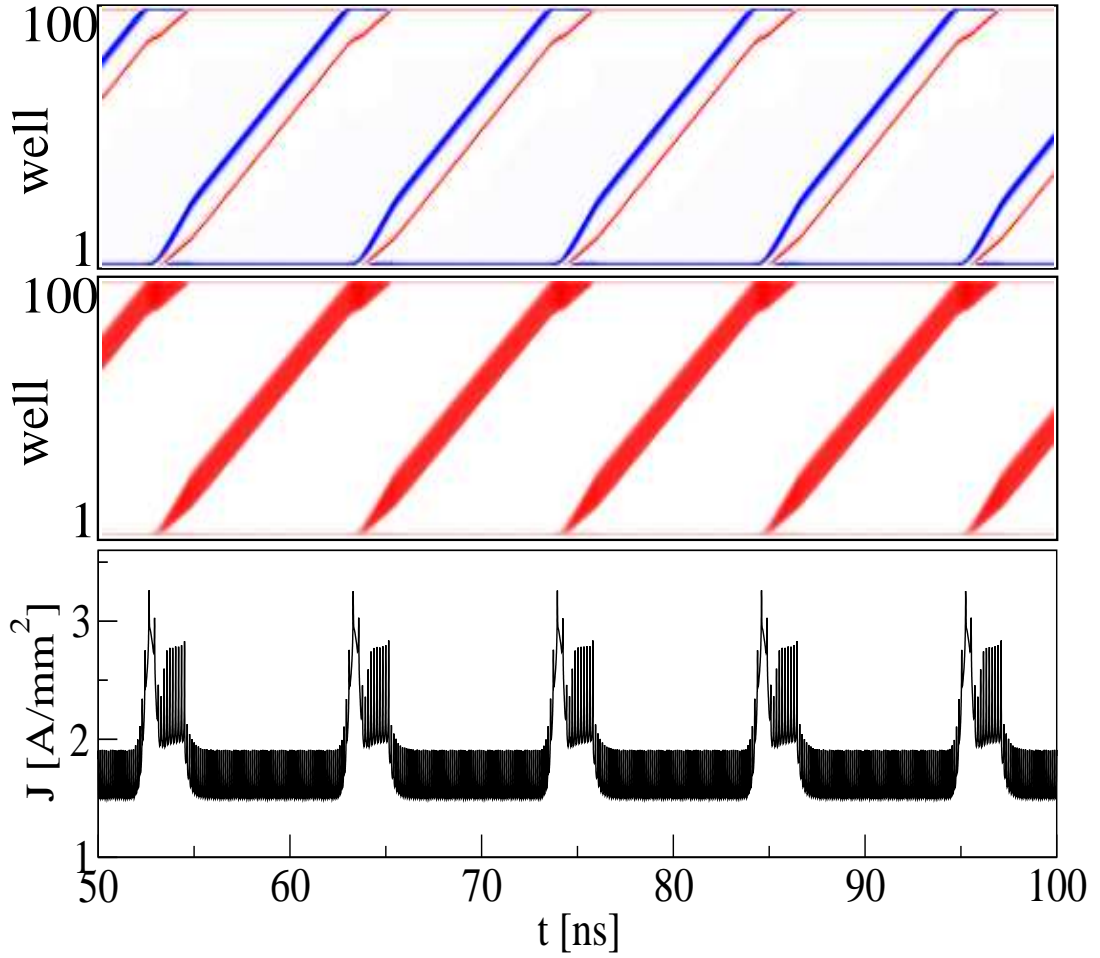


Figure 3.1: Top: Spatio-temporal pattern in superlattice for parameters $\sigma = 1.3(\Omega m)^{-1}$ and $U = 1V$. Red and blue denote charge accumulation and depletion fronts, respectively. White corresponds to a homogeneous configuration. The emitter is located before well 1 and the collector after well 100. Middle: Evolution of the electric field with red areas marking the high-field domains and white the low-field domains. Bottom: Associated current density time series of the global current density $J(t)$ given by Eq. (2.7). Parameters as in Table 2.1.

3.3 The role of the boundary

Assume that the contact conductivity σ is chosen such that the contact characteristic $J_{0 \rightarrow 1} = \sigma F_0$ intersects the homogeneous characteristic between first and second well, $J_{1 \rightarrow 2}(F_1, N_D, N_D)$, at a point (F_c, J_c) in the NDC region (Fig. 3.2). If

$J < J_c$, the field at the emitter is larger than that at the first barrier, $F_1 > F_0$. This results in electron depletion, $n_1 < N_D$ according to the Poisson equation (2.3). If we could suddenly change the current to a value larger than J_c , the field F_1 would increase according to Eq. (2.3). This would result in charge accumulation followed by the depletion front already there. Together they would form a dipole. With proper selection of the two parameters, σ and U , complex front motion may be obtained [Ama04].

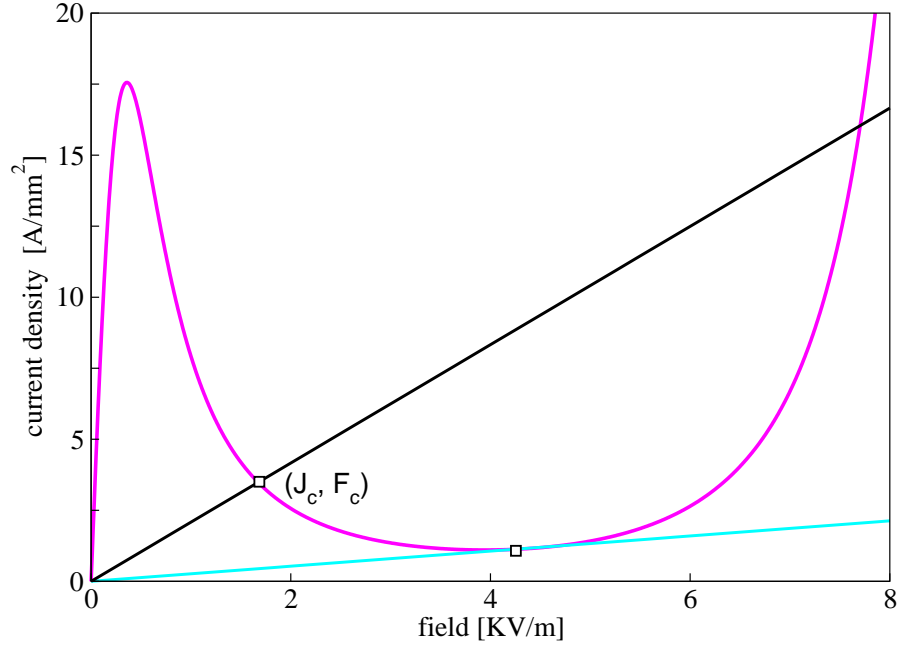


Figure 3.2: Intersection of two Ohmic contact characteristics ($J_{0 \rightarrow 1} = \sigma F_0$) with the homogeneous current-field characteristic (magenta line). Cyan line corresponds to $\sigma = 0.266(\Omega m)^{-1}$ and black line to $\sigma = 2.0821(\Omega m)^{-1}$. (J_c, F_c) marks the intersection point with the homogeneous characteristic. Parameters as in Table 2.1.

3.4 Stationary to moving fronts: Bifurcation scenarios

The transition from stationary to oscillatory behaviour in the context of nonlinear dynamics happens through a bifurcation, when a certain parameter achieves a critical value. In the following we will study the two main bifurcation mechanisms which govern the switching from stationary to moving fronts in the superlattice.

3.4.1 The (σ, U) plane

The two control parameters which determine whether the front dynamics are stationary or moving, are the contact conductivity σ and the externally applied voltage U . In Fig. 3.3 a bifurcation diagram in the (σ, U) plane is shown. The regime

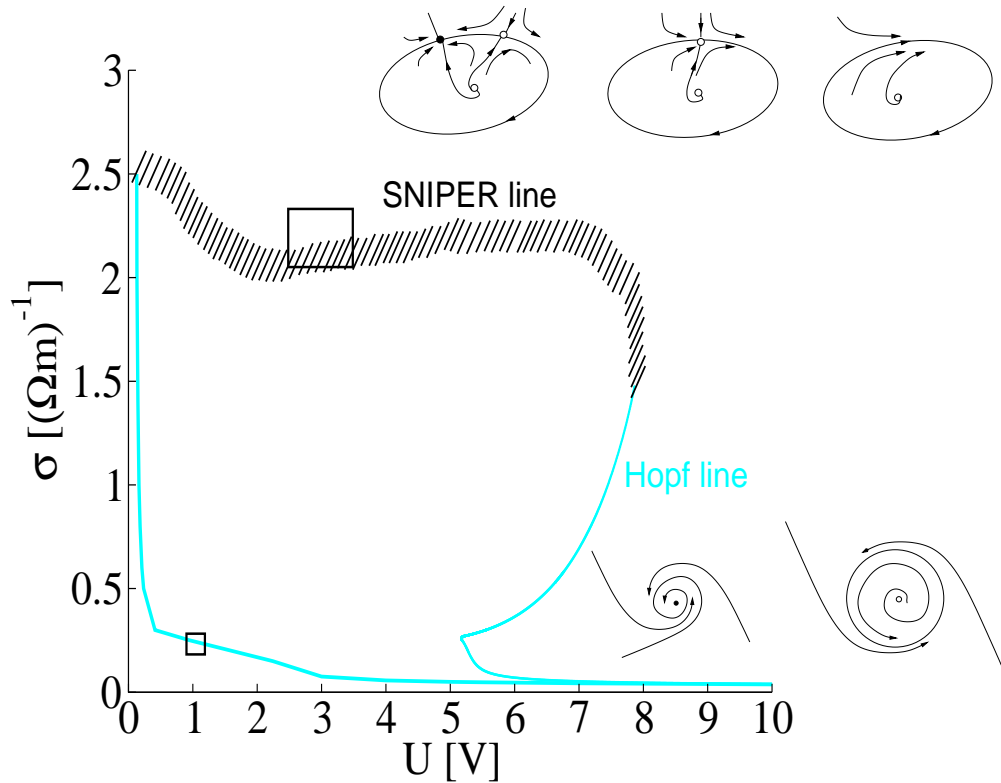


Figure 3.3: Bifurcation diagram in the (σ, U) plane produced by the numerical package AUTO [Doe02]. Black hatched line and cyan line denote the parameter regime in which a saddle-node bifurcation on a limit cycle and a supercritical Hopf bifurcation (illustrated in corresponding schematic figures) takes place, respectively. Boxes mark the two regimes, one in the vicinity of the *SNIPER* and one in the vicinity of the Hopf bifurcation, which are studied throughout this work. Parameters as in Table 2.1.

of oscillations is in the closed area and is bounded below by a supercritical Hopf bifurcation (solid cyan line), and above by a fold bifurcation (saddle-node bifurcation on a limit cycle, or saddle-node infinite period bifurcation, *SNIPER*) (black hatched line). In the same figure both bifurcations are illustrated schematically: A stable focus loses its stability and a limit cycle is born in a supercritical Hopf

bifurcation (lower plot). A saddle-point and a node lying on a closed curve of heteroclinic orbits collide and a stable limit cycle is generated in a *SNIPER* bifurcation (upper plot). The Hopf bifurcation and the *SNIPER* are, therefore, the two basic bifurcations that govern the transition from stationary to moving fronts. In the following we will go through the dynamics characterizing these two bifurcations and give a physical interpretation for our specific model.

3.4.2 Hopf bifurcation

We now fix the parameters of the system in the area marked by the lower box in Fig. 3.3, i. e. near the Hopf bifurcation [Hiz05]. Below the line and for parameters

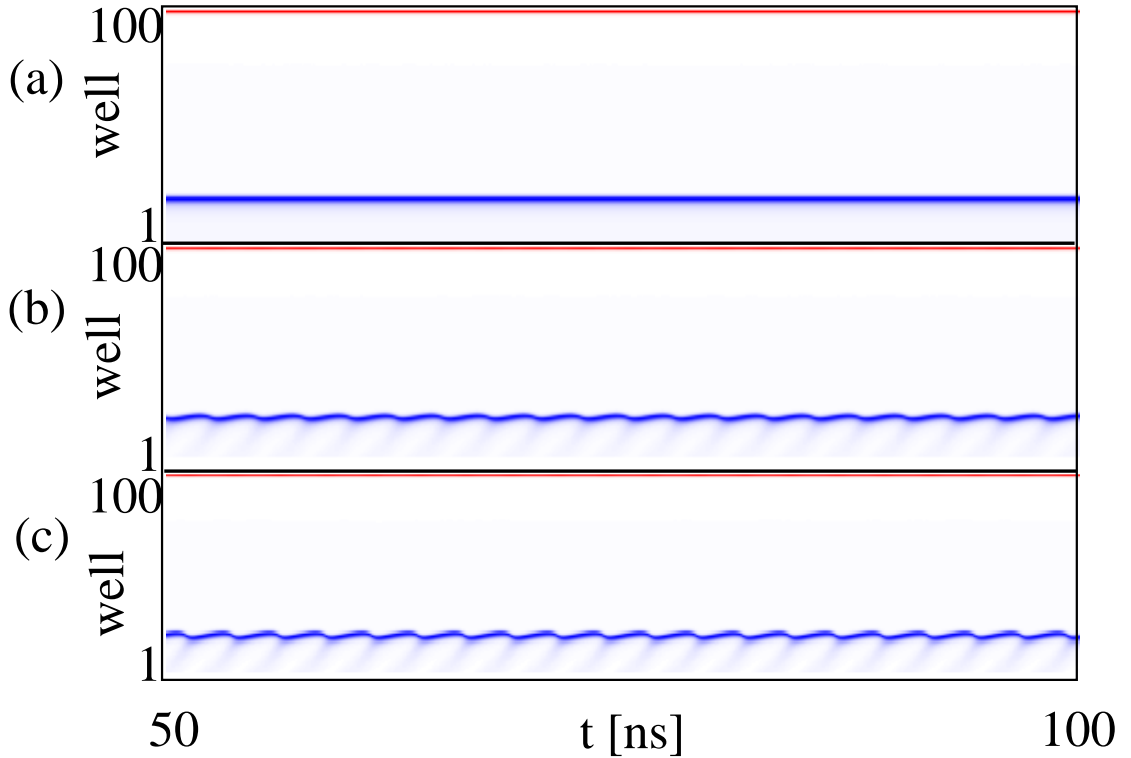


Figure 3.4: Spatio-temporal electron density plots near the Hopf bifurcation. (a) Stationary front below the bifurcation at $\sigma = 0.266(\Omega m)^{-1}$, weak front motion above the bifurcation at $\sigma = 0.2673$ and $\sigma = 0.268(\Omega m)^{-1}$ in (b) and (c), respectively. Voltage $U = 1V$ and other parameters as in Table 2.1.

$(\sigma, U) = (0.266(\Omega m)^{-1}, 1V)$ the only stationary solution is a fixed point that corresponds to a stationary depletion front localized over a small range of wells

near the emitter (Fig. 3.4 (a)). This small value of σ pins a high-field domain at the emitter region and suppresses the generation of accumulation fronts at the emitter. Note that for the considered superlattice a free depletion front under fixed current conditions would always have a positive velocity [Ama02a]. The observed stationarity of the depletion front is therefore a consequence of the global coupling Eq. (2.4) and the suppression of new fronts at the emitter.

For values of σ close but above the Hopf bifurcation the depletion front exhibits some weak motion around its former fixed position (Figs. 3.4 (b) and 3.4(c)). There is no front travelling through the device but instead a slight “wiggling” of the electron density depletion around well 18. The corresponding current density time series, shown in the left panels of Fig. 3.5, display the typical increase in the amplitude expected above a Hopf bifurcation.

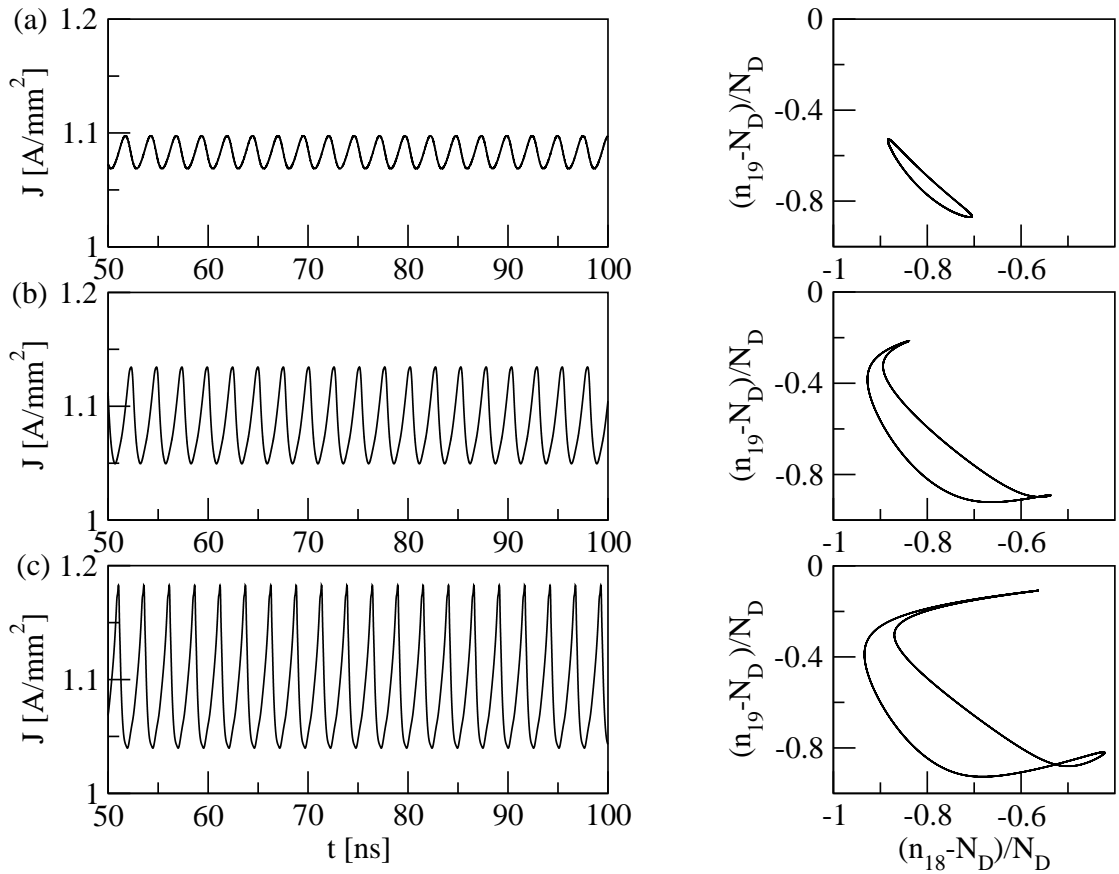


Figure 3.5: Time series of the total current density (left) and corresponding phase portraits in the (n_{18}, n_{19}) plane (right), above the Hopf bifurcation. (a) $\sigma = 0.267$, (b) $\sigma = 0.2673$ and (c) $\sigma = 0.268(\Omega m)^{-1}$. $U = 1V$ in all plots. Parameters as in Table 2.1.

The frequency of the oscillations is finite at the birth of the limit cycle and remains constant at 0.4 GHz. The phase portraits in a cross section of the 100-dimensional phase space are also to be seen in the right panels of the same figure. The limit cycle increases in radius according to the characteristic square-root scaling law. In Fig. 3.6 the amplitude of the total current density oscillations ($J_{max} - J_{min}$) shows this square-root dependence over the contact conductivity σ both in linear and double logarithmic scale.

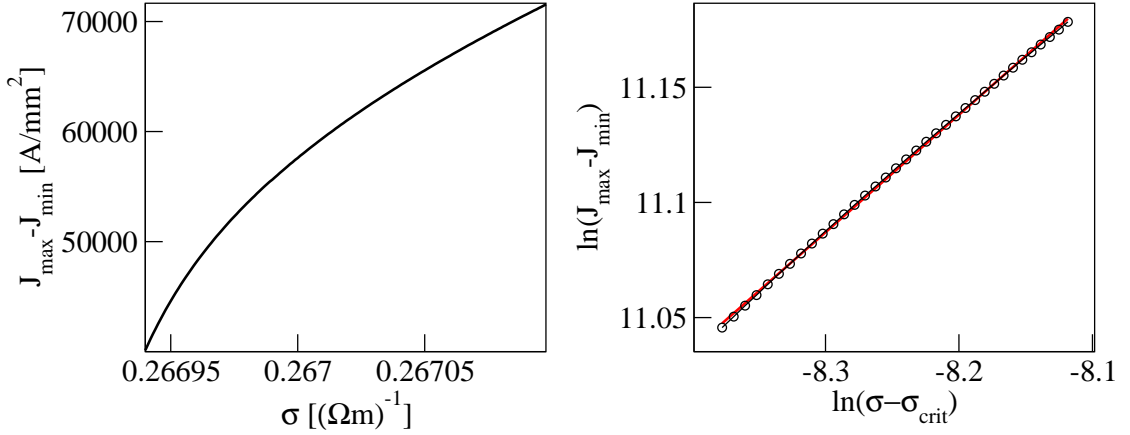


Figure 3.6: Left: Amplitude of the limit cycle oscillations in dependence on the contact conductivity σ above the Hopf bifurcation. Right: Corresponding square-root scaling law: Open circles correspond to data from numerical simulation and red thick line corresponds to a linear fit with slope 0.501. Critical value $\sigma_{crit} = 0.26694(\Omega m)^{-1}$ and voltage $U = 1V$. Parameters as in Table 2.1.

3.4.3 Saddle-node bifurcation on a limit cycle: *SNIPER*

By selecting a higher contact conductivity σ [Hiz06] (in the area marked by the upper box in Fig. 3.3) we set the system at a fixed point which corresponds to a stationary current running through the device and, in the spatio-temporal picture, to an accumulation front localized at well 64 (see Fig. 3.7 (a)). This accumulation front separates a low- from a high-field domain marked by white and red, respectively, in Fig. 3.8(a). Keeping σ fixed and increasing the voltage, we observe the birth of an oscillation at a critical value of the voltage $U_{crit} = 3V$. With further increase of U the period of the limit cycle decreases, as shown in Figs. 3.7(b) and 3.7(c), for both current density time series and spatio-temporal plots. The corresponding moving field domains are shown in Fig. 3.8. The sudden birth of the

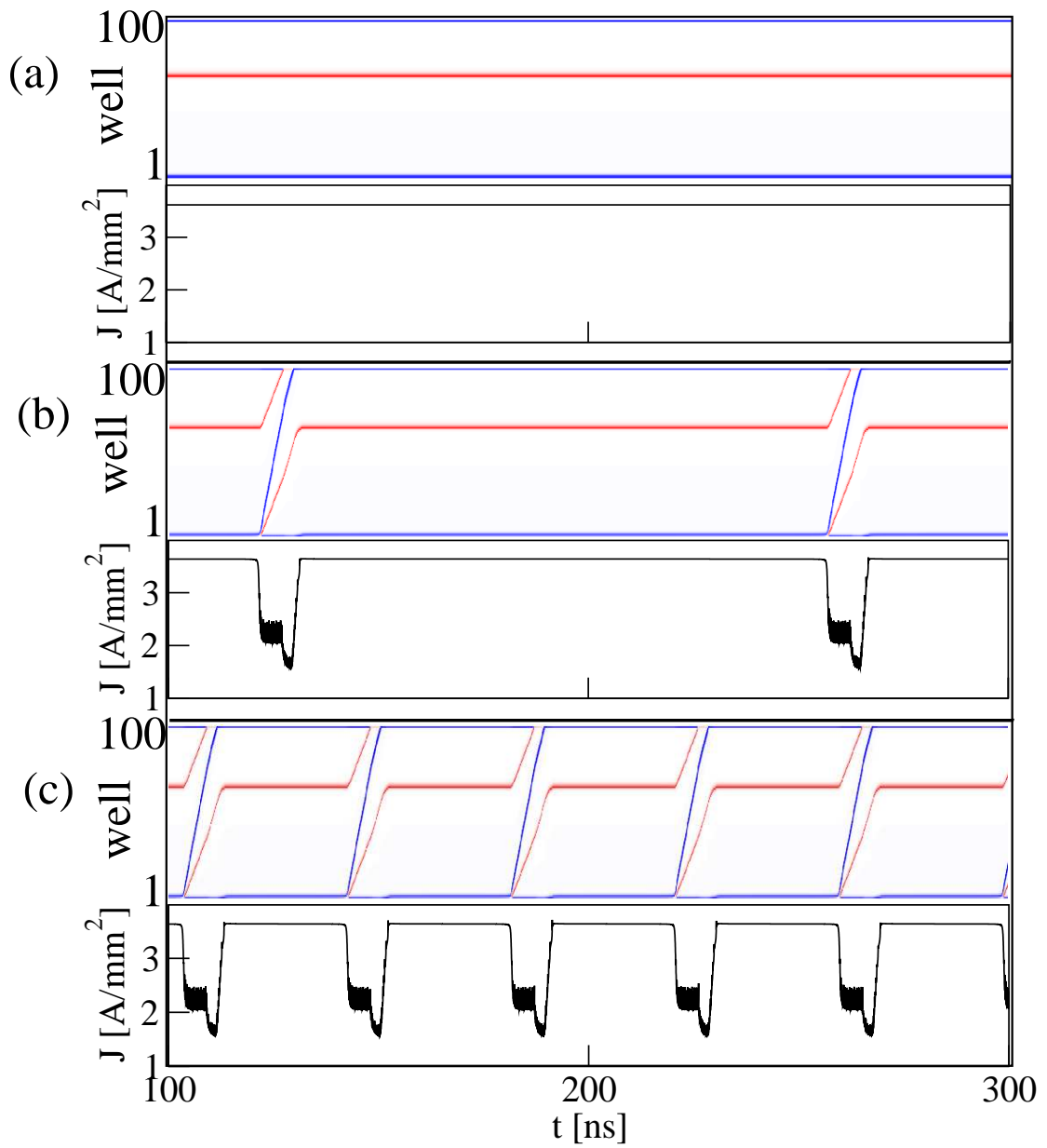


Figure 3.7: Time series of the total current density (lower plots) and corresponding spatio-temporal plots (upper plots), below (a) and above ((b) and (c)) the *SNIPER*. (a) $U = 2.99$, (b) $U = 3.0000002$ and (c) $U = 3.00001$ V. $\sigma = 2.0821(\Omega m)^{-1}$ in all plots. Parameters as in Table 2.1.

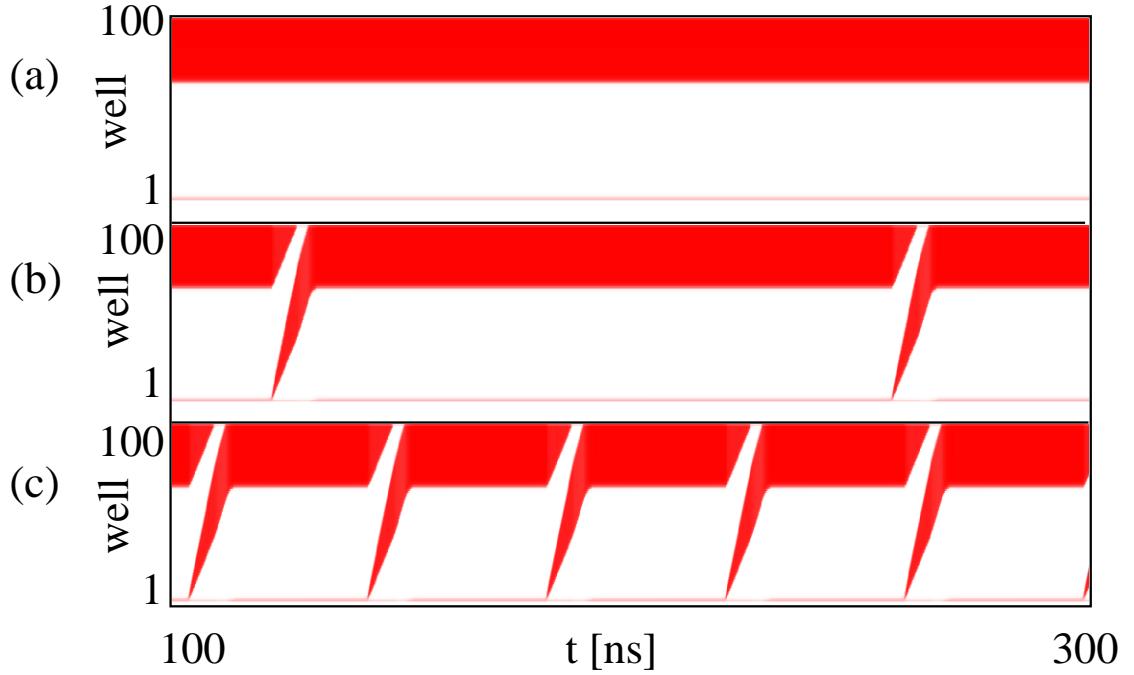


Figure 3.8: Spatio-temporal plots of the electric field corresponding to Fig. 3.7. (a) $U = 2.99$, (b) $U = 3.0000002$ and (c) $U = 3.00001V$. High-field domains are shaded red. $\sigma = 2.0821(\Omega m)^{-1}$ in all plots. Parameters as in Table 2.1.

limit cycle takes place through a saddle-node bifurcation on a limit cycle. In such a bifurcation a saddle-point and a stable node, both lying on an invariant circle, collide, disappear and a limit cycle is generated. At the critical point U_{crit} , the frequency of the oscillations tends to zero. This corresponds to an infinite period oscillation (Fig. 3.9 (a)) and therefore this bifurcation is also known as saddle-node infinite period bifurcation or *SNIPER* [Guc86]. It is one of the so-called *global* bifurcations as discussed in Chapter 6.

Plotting the frequency of the oscillations above the *SNIPER* in dependence on the bifurcation parameter U (Fig. 3.9 (b)), we obtain the characteristic square-root scaling law, $f \sim (U - U_{crit})^{1/2}$, that governs a saddle-node bifurcation on a limit cycle.

Figure 3.10(a) shows a phase portrait in terms of electron densities in two neighboring wells, below the bifurcation, for three different initial conditions. The electron density in well 65, n_{65} , is plotted versus n_{64} , in a two-dimensional projection of the 100-dimensional phase space. Arrows denote the direction which the trajectory follows and the thick dot (VI) corresponds to the stable node, i. e. a stationary

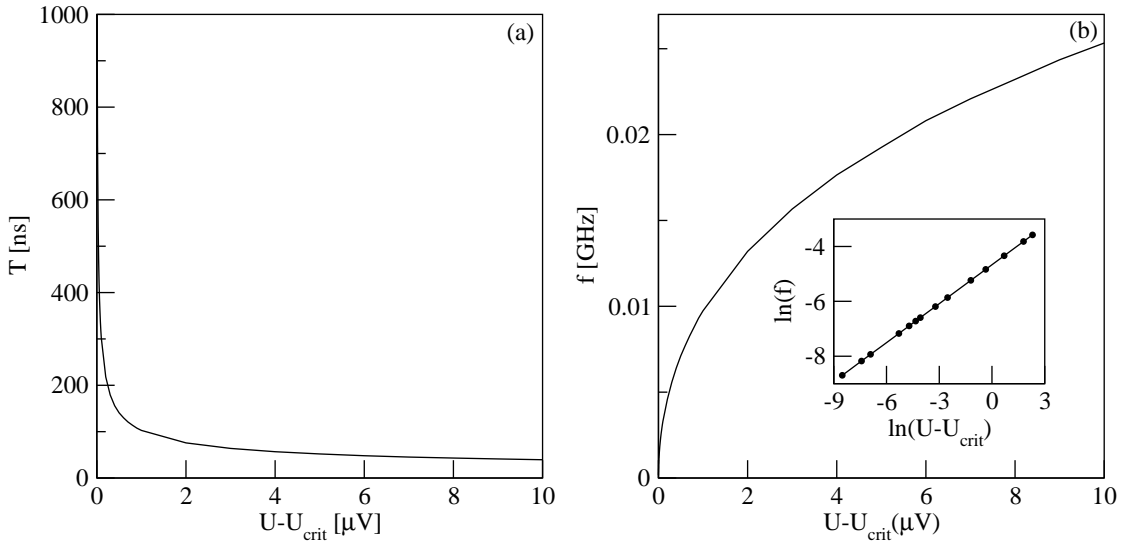


Figure 3.9: (a) Period T and (b) frequency $f = 1/T$ of the current density time series above the *SNIPER* in dependence on the voltage. The inset of (b) shows the characteristic square-root scaling law that governs a saddle-node bifurcation on a limit cycle. $U_{crit} = 3V$ and $\sigma = 2.0821(\Omega m)^{-1}$. Parameters as in Table 2.1.

accumulation front, which all trajectories approach regardless of the initial condition. The cross denotes the saddle-point which corresponds to a stationary spatial configuration which separates two regimes: Either no dipole is injected at the emitter (this is associated with the short piece of the unstable manifold connecting the saddle-point and the stable node), or a dipole is injected and traverses the system, and interacts with the stationary accumulation front, thus performing a full tripole oscillation. The latter corresponds to the trajectory shown (labeled I-V) which performs a large excursion in phase space before approaching the stable node (VI). It is close to the long piece of the unstable manifold connecting the saddle-point with the stable node via a big loop. In Figs. 3.10(b), 3.10(c) and 3.10(d), the space-time plot of the electron densities and the time evolution of the electron density n_{65} are plotted for all three trajectories of Fig 3.10(a). From Fig 3.10(b) we see that initially an accumulation front is located near well 64 (I). After a depletion front is injected at the emitter, followed immediately by the injection of an accumulation front, both move through the system (II-IV) while the first accumulation front also starts moving towards the collector (II) (driven by the global constraint (Eq. (2.4))). Finally the accumulation front generated at the emitter approaches well 64 (V) and rests there (VI), while at the emitter a new depletion front starts to develop. In this context the previously discussed

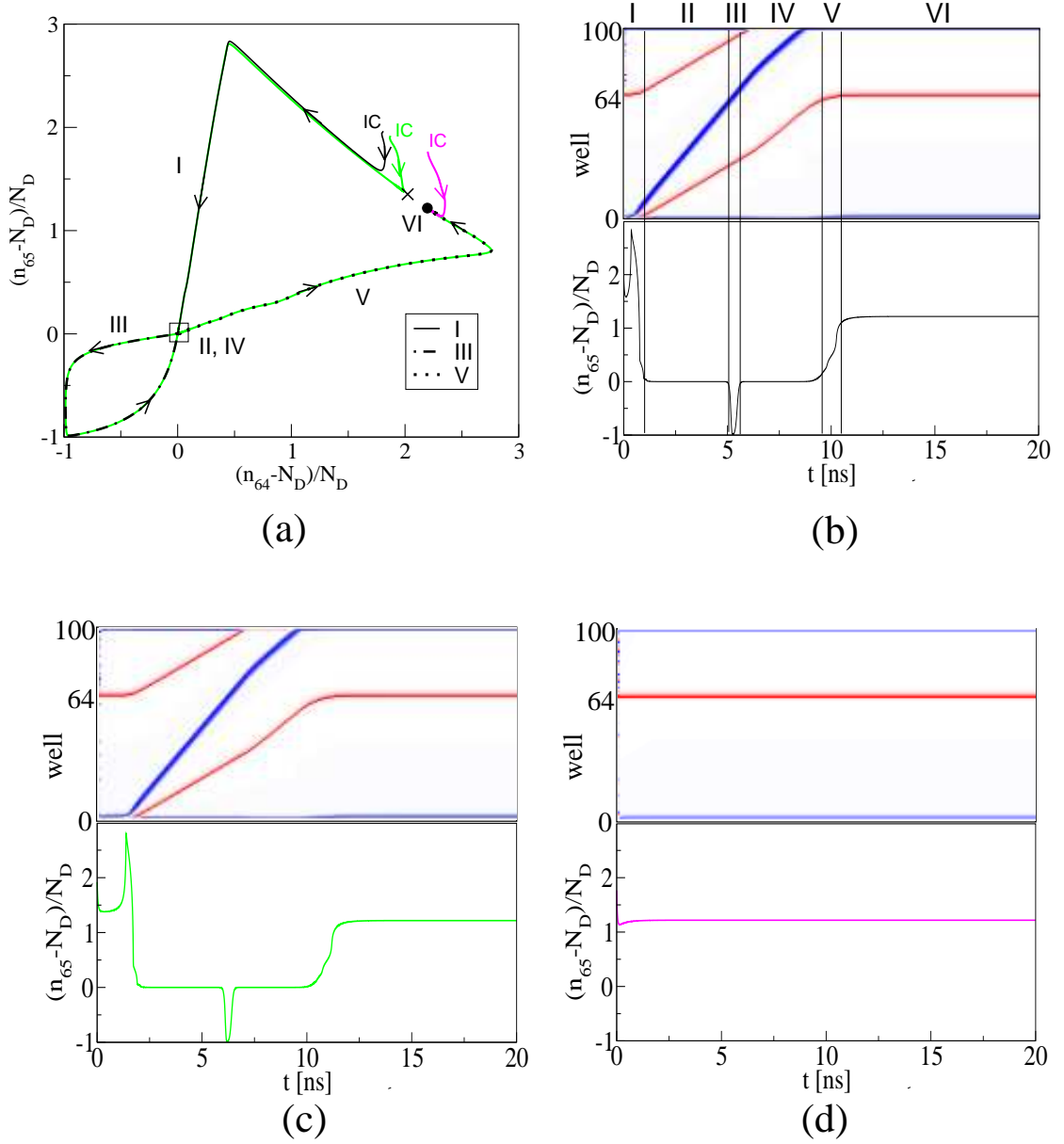


Figure 3.10: (a) Phase portrait in terms of electron densities n_{65} and n_{64} , normalized to the donor density N_D , below the global bifurcation. Three different initial conditions (IC) have been used, corresponding to trajectories of different color. (b) Space-time plot (upper plot) and time series of n_{65} (lower plot) for the black trajectory shown in (a). The different parts of the trajectory are labeled by Roman numerals I-VI. Corresponding space-time plot and time series of n_{65} for green and magenta trajectory depicted in (c) and (d), respectively. $U = 2.99V$ and $\sigma = 2.0821(\Omega m)^{-1}$. Parameters as in Table 2.1.

saddle-point corresponds to the stationary but unstable situation, where the depletion front is not yet completely detached from the emitter. This is evident also in the space-time plot of the green trajectory of Fig 3.10(a), shown in Fig 3.10(c). The green trajectory spends more time (than the black one) near the saddle-point, before performing the long excursion in phase space leading to the stable node. In the space-time plot, this is demonstrated as such: It takes longer time for the accumulation front to start moving and for the depletion front to detach from the emitter until they eventually form a dipole on their way to the collector. Otherwise: If we divided the trajectory and space-time plot in parts denoted by Roman numerals as for the case of the black trajectory, part (I) would be wider. Finally, the magenta trajectory of Fig 3.10(a) is at once attracted by the stable node. This is visible in the corresponding space-time plot and time series in Fig 3.10(d).

Scanning the area marked by the upper box in Fig. 3.3 both in σ and U we obtain a more detailed bifurcation diagram shown in Fig. 3.11. The yellow area

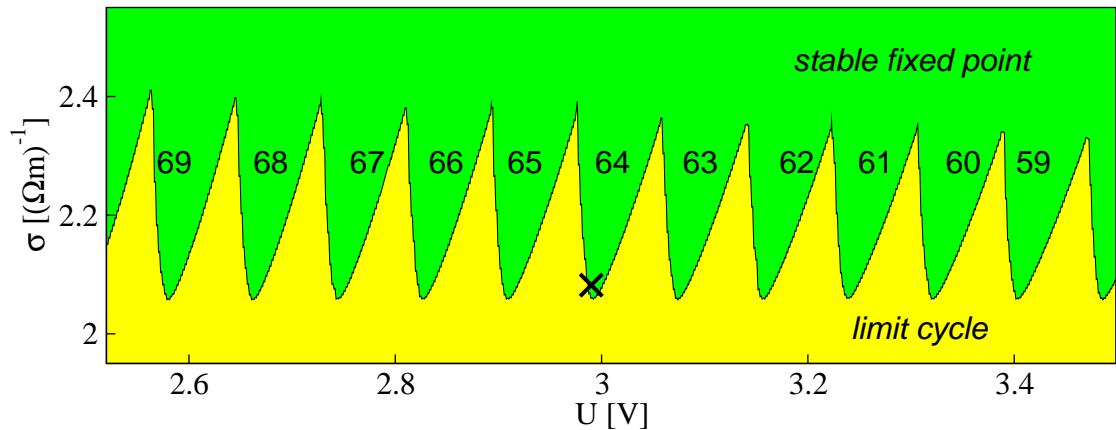


Figure 3.11: Bifurcation diagram in the (σ, U) plane. Yellow and green regions correspond to moving and stationary domains, respectively. The black line is the border of the yellow region and marks the bifurcation line where a saddle-node bifurcation on a limit cycle takes place. Numbers denote the positions of the stationary accumulation front in the device. The cross marks the parameter set used in the following chapters where the effect of noise and delay below the *SNIPER* in the superlattice is studied. Parameters as in Table 2.1.

corresponds to moving domains and the green area to stationary ones. The black line separates these two regions and marks the bifurcation line where a *SNIPER* takes place. Numbers denote the positions of the stationary front and each tongue (yellow) corresponds to a specific position of the stable accumulation front within the superlattice. With increasing U the position shifts towards the emitter, well

by well, thus increasing the size of the high-field domain between the accumulation front and the collector. This is shown in Fig. 3.12 (upper plot), where the electron density profiles along the superlattice are depicted for fixed contact conductivity and increasing voltage. The black line corresponds to a voltage value $U = 2.83V$

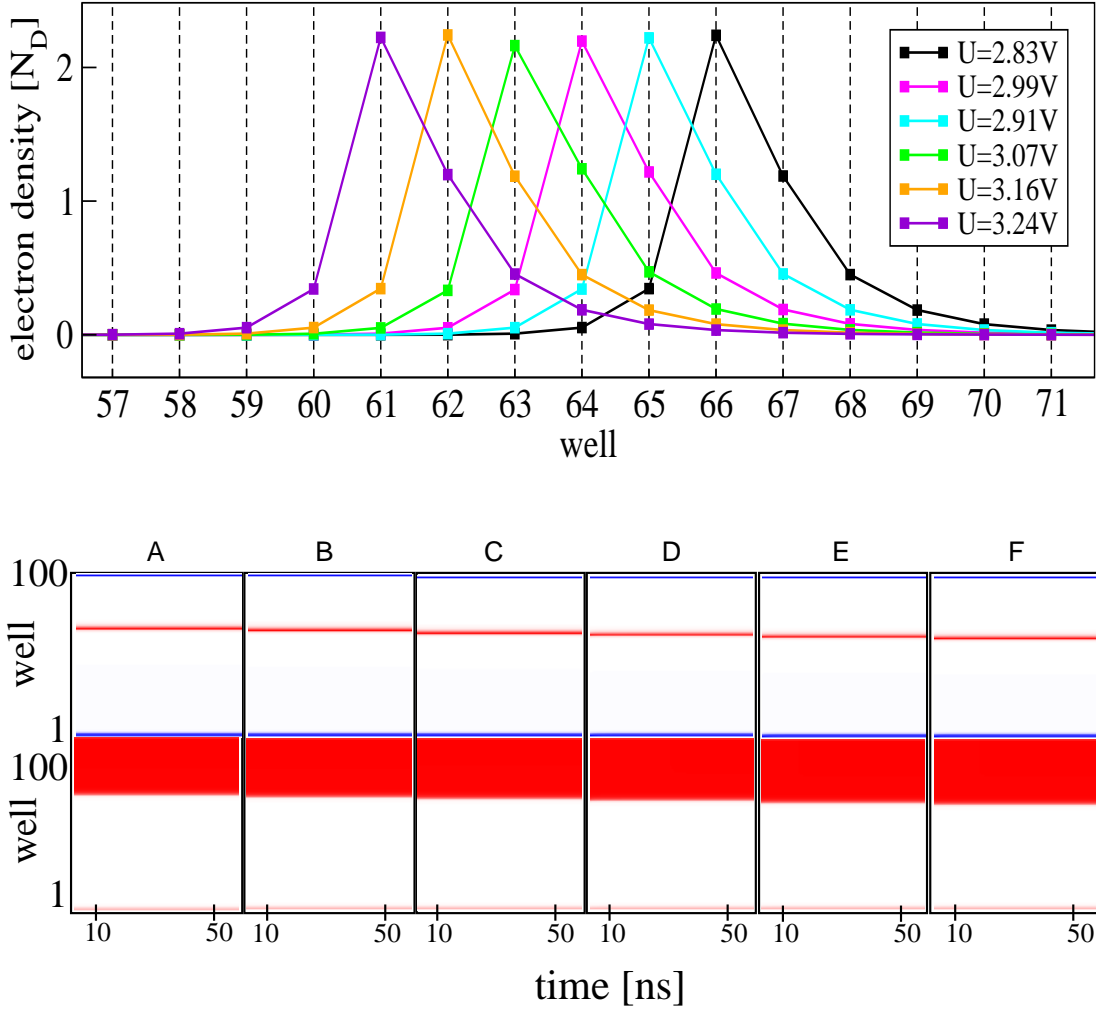


Figure 3.12: Top: Electron density (minus the doping density) profiles of stationary accumulation front for increasing voltage (from left to right) corresponding to green tongues of Fig. 3.11. Bottom: Corresponding spatio-temporal plots of electron density (upper) and electric field density (lower). Voltage increases from A to F. $\sigma = 2.0821(\Omega m)^{-1}$ in all plots. Parameters as in Table 2.1.

and to a stationary accumulation front located at well 66. Increasing the voltage, the position of the accumulation front is shifted by 5 wells towards the emitter,

reaching, finally, well number 61 at $U = 3.24V$. In the lower panel of the same Figure the corresponding spatio-temporal plots of the electron density and the electric field are shown. In the latter, one can clearly see the increase in the size of the high-field domain between the accumulation front and the collector as the voltage increases, from A to F.

The global bifurcation can be understood by noting the important role of the current at the emitter for the bifurcation. For high σ only stationary accumulation fronts appear, and a typical sawtooth pattern in the current-voltage characteristic is obtained [Pat98, Ama01]. As we decrease σ , we lower the critical current J_c , above which depletion fronts are triggered at the emitter [Ama04].

In the regime of σ shown in Fig. 3.11 it depends upon the voltage whether a depletion front will develop fully at the emitter. In the green region the current of the stationary accumulation front is below J_c , and therefore no fronts are generated at the emitter. In the region of the yellow tongues, however, the stationary accumulation front is not stable, since it corresponds to a current larger than J_c . Instead of a stationary current we therefore observe periodic current oscillations, where the current only rises above J_c during the dipole injection phases, and otherwise is less than J_c [Ama04]. This is the physical interpretation of the *SNIPER*.

The *SNIPER* was first observed experimentally in a semiconductor device [Pei89], and also encountered in various semiconductor models, e.g. for Gunn domains [Shi96], superlattices [Pat98, Hiz06], or lasers [Dub99, Wie02, Kra03a].

4 Noise-induced dynamics

Noise is an inevitable feature in physical systems. Since the seminal work of A. Einstein on Brownian motion [Ein05], its theoretical treatment has been very central in the field of statistical physics. In the last couple of decades it has attracted a lot of attention by researchers working in the vast field of nonlinear dynamics. Nonlinearity and randomness may interact in a very interesting manner.

In electrical conductors the two fundamental sources of noise are thermal noise and shot noise. Thermal noise, also known as Johnson-Nyquist noise [Joh28, Nyq28], is due to the thermal motion of electrons. Authors Johnson (experiment) and Nyquist (theory) showed that an electric resistor at equilibrium, i.e. under no external bias, generated fluctuations of electric voltage. The second source of noise, for nonequilibrium systems, is shot noise [Sch18] and is due to the discrete nature of the electron charge in units of the elementary charge tunneling through barriers.

In semiconductor nanostructures far from equilibrium it is well known that microscopic random fluctuations essentially affect the transport mechanisms [Bla00, Son03, Zha00, Kie03b, Kie04, Kie05a, Kie07a, Kie07b]. They usually smear out and deteriorate the regularity in charge transport. However, nowadays for a large class of extended systems of reaction-diffusion type it has been shown that noise can play a constructive role. Noise-induced ordering was first demonstrated in the phenomena of stochastic [Gam98] and coherence [Hu93a, Pik97, Lin04] resonance. Since then the applications to physical models have been numerous. In extended systems, moreover, it has been shown that noise can induce quite coherent dynamical spatio-temporal patterns [Gar99, Sag07]. Recently, such noise-induced patterns were also found in semiconductor nanostructures described by a reaction-diffusion model for the current density distribution [Ste05, Maj07, Sch08a]. Thus, the open question to what extent the noise-induced ordering occurs generally in different classes of nanostructures, becomes of central importance.

4.1 Noise in the superlattice model

We extend the deterministic model to incorporate stochastic influences. The dominant noise source, which effects the electron dynamics in semiconductor nanostructures, is shot noise, which is associated with the fluctuations of the times between tunneling of electrons across a potential barrier (see e.g. [Pou03] for a theoretical description). In the case of a weakly coupled superlattice, the random component of the well-to-well current can be described in a first approximation by Poissonian statistics [Bla00]. Those fluctuations affect the current densities $J_{m \rightarrow m+1}$. Assuming that the tunneling times are much smaller than any characteristic time scale of the global current through the device Eq. (2.7) and taking into account that each current density $J_{m \rightarrow m+1}$ is influenced by many Poissonian events we can roughly approximate those fluctuations by Gaussian white noise sources in the continuity equations for the electron densities [Bon02a, Bon04]. Charge conservation is automatically guaranteed by adding a noise term ξ_m to each current density $J_{m-1 \rightarrow m}$:

$$e \frac{dn_m}{dt} = J_{m-1 \rightarrow m} + D\xi_m(t) - J_{m \rightarrow m+1} - D\xi_{m+1}(t), \quad (4.1)$$

where $\xi_m(t)$ is Gaussian white noise with

$$\langle \xi_m(t) \rangle = 0, \quad (4.2)$$

$$\langle \xi_m(t) \xi_{m'}(t') \rangle = \delta(t - t') \delta_{mm'}, \quad (4.3)$$

and D is the noise intensity. Since we assume that the inter-well coupling in our superlattice is very weak, these noise sources can be treated as independent. In the following we will study the effect of noise in two different dynamical regimes, first below the Hopf bifurcations and then below the global *SNIPER* bifurcation. We will observe the differences in the noise-induced dynamics.

4.2 Regime I: Below the Hopf bifurcation

We tune the parameters such that the system lies slightly below the Hopf bifurcation line (Fig. 3.3) [Hiz05]. In the absence of noise ($D = 0$), as seen in Chapter 3, the only stationary solution is a stable fixed point that corresponds to a stationary depletion front localized over a small range of wells near the emitter (Fig. 3.4 (a)). In the following the contact conductivity and the voltage will be kept fixed at values $\sigma = 0.266(\Omega m)^{-1}$ (corresponding to the cyan contact characteristic in Fig. 3.2) and $U = 1V$, respectively and the noise is switched on.

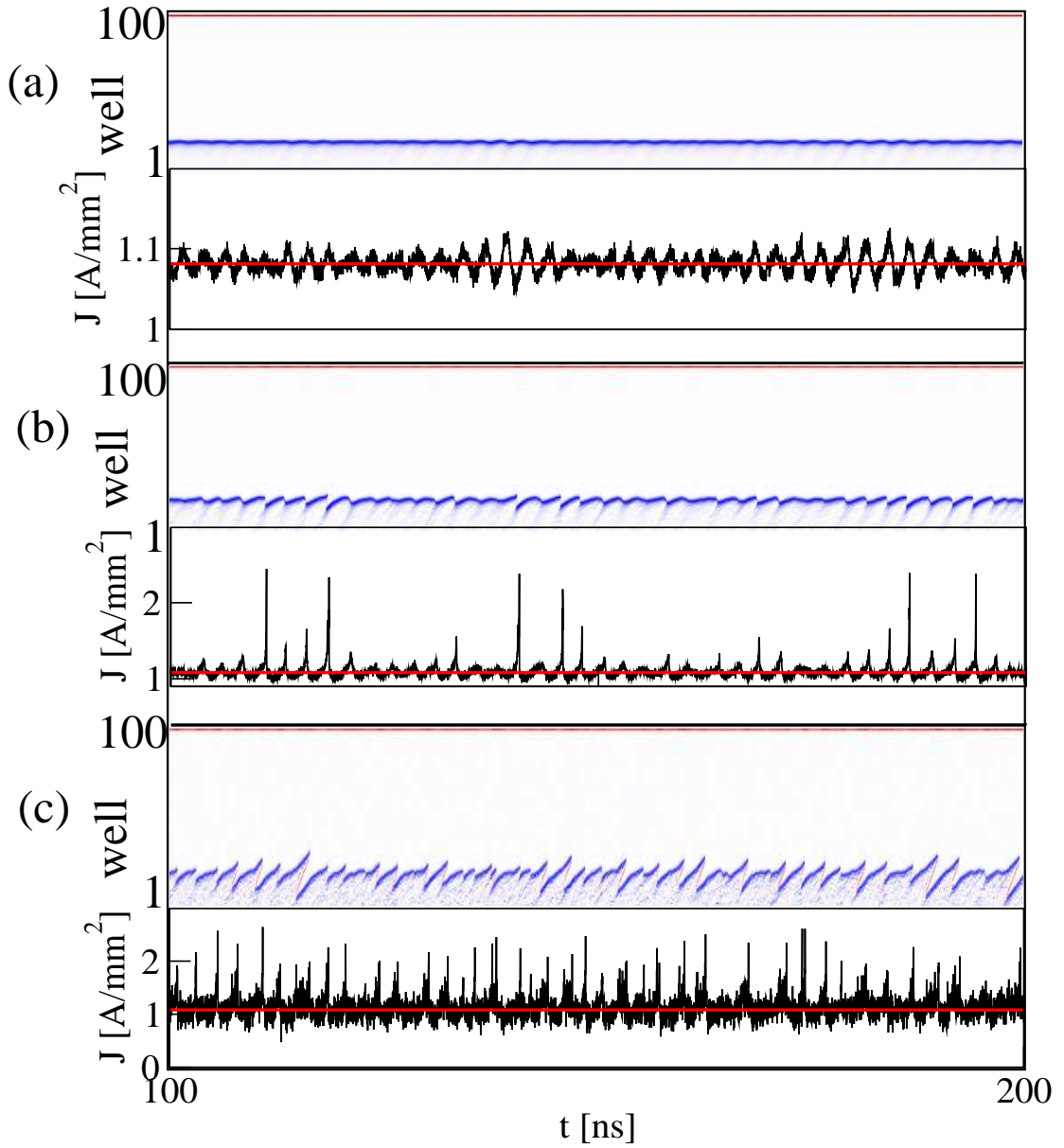


Figure 4.1: Simulation of the superlattice model from (4.1) with (a) $D = 0.1$, (b) $D = 0.5$ and (c) $D = 2.5 A s^{1/2} / m^2$. Initial condition chosen below the Hopf bifurcation in the stable fixed point ($\sigma = 0.266(\Omega m)^{-1}$, $U = 1V$). Spatiotemporal pattern (upper plots) and noise-induced oscillations of the total current density (lower plots) around the fixed point marked with red.

4.2.1 Noise-induced current oscillations

As the noise intensity increases ($D > 0$), the current density starts to oscillate in a quite regular manner around the steady state (upper panel of Fig. 4.1 (a)). From the corresponding charge density plot (lower panel of Fig. 4.1 (a)) we can associate this oscillation with a periodic motion of the depletion front as a whole. This is the expected behavior close to a Hopf bifurcation. At even larger noise intensities, however, the nature of the observed dynamics changes dramatically (Figs. 4.1(b) and 4.1(c)). Now the current oscillations are no longer harmonic around the stationary value, but become sharply peaked and spiky, and the average current is shifted towards larger values. This is reflected in a more asymmetric motion of the depletion front. In particular we now occasionally observe the onset of a tripole oscillation, where in addition to the existing depletion front, a dipole of an accumulation and a depletion front is generated close to the emitter, and the leading (but not fully developed) accumulation front catches up and annihilates with the already present depletion front, while the trailing depletion front remains.

4.2.2 Effect of noise on the coherence

To quantify the regularity of oscillations we introduce the correlation time t_{cor} given by the formula [Str63] :

$$t_{cor} := \frac{1}{\sigma^2} \int_0^\infty |\psi(s)| ds, \quad (4.4)$$

where $\psi(s)$ is the autocorrelation function of the current density signal $J(t)$,

$$\psi(s) = \langle (J(t) - \langle J \rangle)(J(t+s) - \langle J \rangle) \rangle, \quad (4.5)$$

and $\psi(0) = \sigma^2$ is its variance. In addition to the autocorrelation function, the Fourier power spectral density (in the following referred to as power spectrum) of the noisy oscillations may be considered as a measure for the coherence. We express it in terms of the total current density:

$$S_J(\omega) = \lim_{T \rightarrow \infty} \frac{1}{2\pi T} \left| \int_0^T J(t) e^{-i\omega t} dt \right|^2. \quad (4.6)$$

Using the Wiener-Khinchin Theorem [Gar02] which links the power spectrum with the Fourier transform of the autocorrelation function, we obtain:

$$S_J(\omega) = \frac{1}{2\pi} \int_{-\infty}^{\infty} \psi(\tau) e^{-i\omega\tau} d\tau. \quad (4.7)$$

A typical numerical estimate of the autocorrelation function and the power spectrum are shown in black in Fig. 4.2. Qualitatively, for the autocorrelation function,

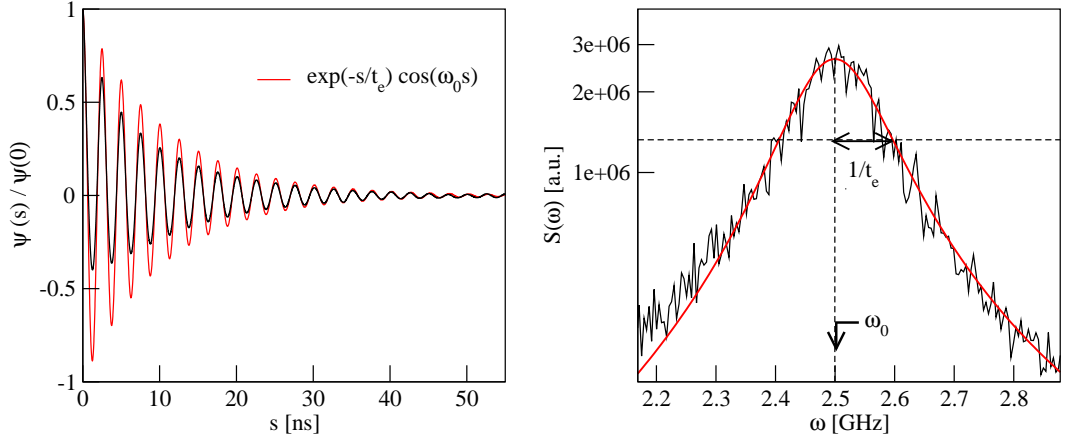


Figure 4.2: Left: Normalized to the variance, $\psi(0)$, autocorrelation function according to (4.5). Right: Fourier power spectral density (black) and Lorentzian fit according to (4.9) (red). ω_0 and $1/t_e$ denote the basic frequency and spectral half-width, respectively. $D = 0.5As^{1/2}/m^2$ in both plots. $\sigma = 0.266(\Omega m)^{-1}$ and $U = 1V$ set below the Hopf bifurcation. Parameters as in Table 2.1.

we see an exponentially damped oscillation which can be approximated by (this becomes exact for linear processes)

$$\psi(s) = \psi(0) e^{-\frac{s}{t_e}} \cos(\omega_0 s). \quad (4.8)$$

The Fourier transform of the autocorrelation function (Eq. (4.5)) is, by the Wiener-Khinchin theorem [Gar02], the power spectrum of the current density. From Eq. (4.8) we obtain approximately a Lorentzian shaped power spectrum:

$$S(\omega) \propto \frac{\omega^2}{(\omega^2 - \omega_0^2)^2 + (\frac{2\omega}{t_e})^2}, \quad (4.9)$$

and $1/t_e$ is now simply the half-width of the spectral peak.

In Fig. 4.2 the analytical approximation for both autocorrelation function and

power spectrum is shown in red. The agreement is rather good and should improve the larger the size of the statistical ensemble is. When the above analytical ansatz for the autocorrelation function and power spectrum holds, one may show that those two measures provide equivalent information for the coherence of the noise-induced oscillations. By setting Eq. (4.8) into Eq. (4.4) we get:

$$t_{cor} = \int_0^{\infty} e^{-\frac{s}{t_e}} |\cos(\omega_0 s)| ds. \quad (4.10)$$

For $\omega_0 t_e \gg 1$ and substituting the cos term by the filling factor $\frac{1}{\pi} \int_{-\pi/2}^{\pi/2} \cos\phi d\phi = 2/\pi$ we get [Sch04b]:

$$t_{cor} = \frac{2}{\pi} \int_0^{\infty} e^{-\frac{\tau}{t_e}} d\tau \approx \frac{2}{\pi} t_e. \quad (4.11)$$

This means that larger correlation times, and therefore more coherent oscillations, correspond to smaller values of the spectral half-widths. The two extreme cases of this are a broad spectrum corresponding to a vanishing correlation time and a narrow one related to a large correlation time. In Fig. 4.3 the correlation time, calculated from Eq. (4.4), is plotted over the noise intensity and with red squares the spectral halfwidth (t_e) multiplied by $2/\pi$ is shown. The two curves are in rather good agreement.

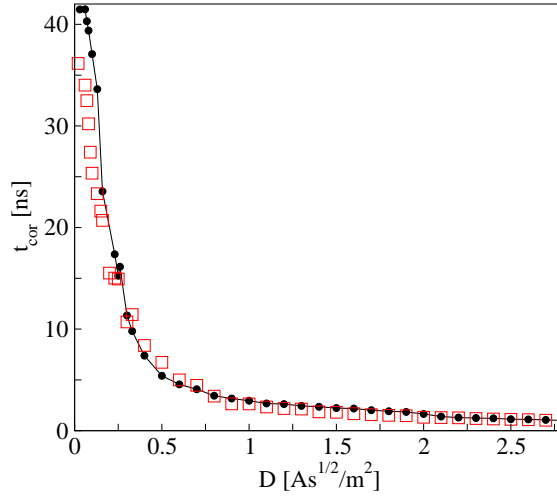


Figure 4.3: Correlation time versus the noise intensity D . Black circles calculated from Eq. (4.4) and red squares calculated from the inverse spectral halfwidths, $t_{cor} = 2t_e/\pi$, according to Eq. (4.11). Values calculated from average over 30 realizations, each calculated from a time series of length $T = 1600ns$. $\sigma = 0.266(\Omega m)^{-1}$ and $U = 1V$. Parameters as in Table 2.1.

Another measure one may extract from the power spectrum is the *degree of coherence* [Hu93a, Lin04], also known as *signal-to-noise-ratio* (SNR), which is often used in laser physics, or coherence factor:

$$\beta = \omega_0 \frac{H}{\Delta\omega}, \quad (4.12)$$

with $\Delta\omega = \omega_2 - \omega_1$, $S(\omega_1) = S(\omega_2) = S(\omega_0/a)$, $\omega_1 < \omega_0 < \omega_2$, where $H = S(\omega_0)$ is the height of the spectral peak at the main frequency ω_0 while $\Delta\omega$ is the spectral half-width at a certain fraction $1/a$ of $S(\omega_0)$. Typical values are $a = e$ [Hu93a] and $a = 2$, which will be used here. In Fig. 4.4 (d), β shows a non-monotonic

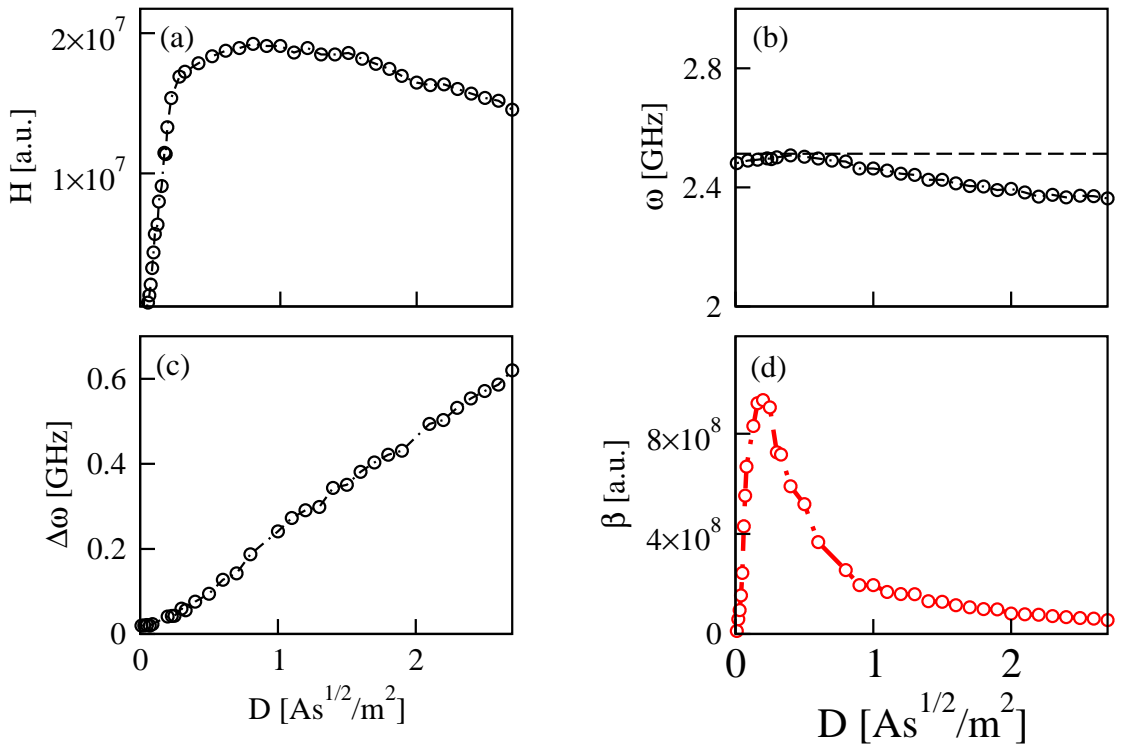


Figure 4.4: (a) Spectral height, (b) basic frequency, (c) spectral width and (d) coherence factor, in dependence on the noise intensity. Calculated from power spectra averaged over 30 realizations, each of length $T = 1600ns$. Voltage and contact conductivity set below the Hopf bifurcation, $\sigma = 0.266(\Omega m)^{-1}$ and $U = 1V$. Parameters as in Table 2.1.

dependence upon the noise intensity, which is expected in the case of a supercritical Hopf bifurcation. In [Ush05] a detailed study on the qualitative differences, in β , between supercritical and subcritical Hopf bifurcation is presented. In the former, H increases monotonically and saturates at higher noise intensities. This is shown

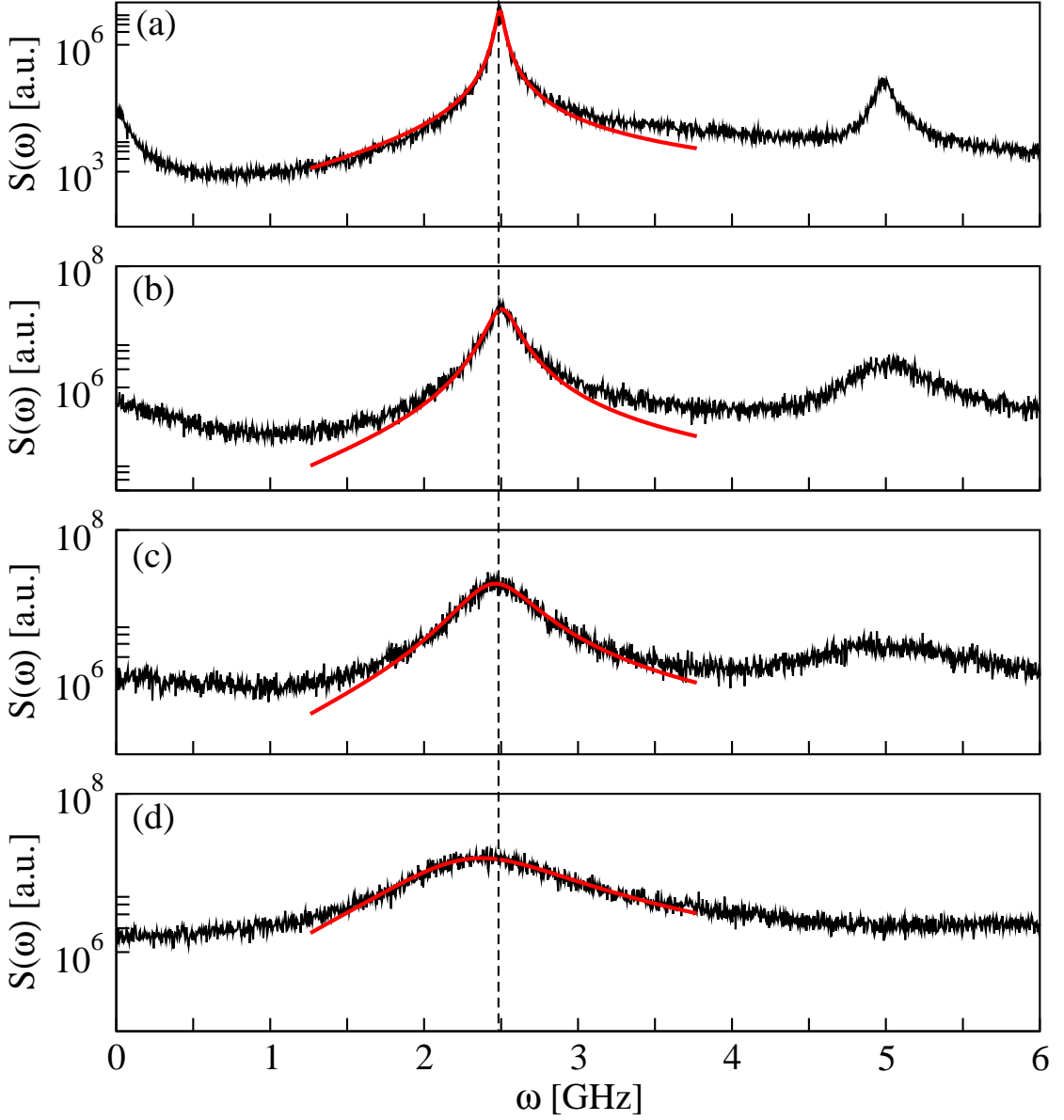


Figure 4.5: Fourier power spectral density of the total current density $J(t)$ for noise intensity (a) $D = 0.1$, (b) $D = 0.5$, (c) $D = 1.0$ and (d) $D = 2.5As^{1/2}/m^2$. Red curves correspond to Lorentzian fits according to (4.9). Averages over 30 time series realizations of length $T = 1600ns$ have been used. $\sigma = 0.266(\Omega m)^{-1}$ and $U = 1V$. Parameters as in Table 2.1.

in Fig. 4.4 (a) (note that for stronger noise, where the power spectra are very

“noisy”, the Lorentzian fit fails to reproduce the exact height and therefore we estimate it manually). The increase in β is caused by the spectral peak height, that is, by an increase of the oscillation amplitude. The spectral width increases also, particularly at higher noise intensities (Fig. 4.4 (b)), weakening, thus, the coherence. The competition between the growth of height and width results in the resonance-like behaviour of β .

4.2.3 Effect of noise on the time scales

Apart from the coherence, we are also interested in the effect of noise on the time scales. The time scale of the noise-induced oscillations is an essential characteristic of noise-induced oscillations. We consider power spectra for different values of noise intensities D (Fig. 4.5) and see that the position of the main spectral peak, corresponding to the basic frequency ω_0 of the oscillations, is almost unchanged. This is also seen in Fig. 4.4 (c) where ω_0 is plotted over D . At low noise the basic period, $T_0 = 2\pi/\omega_0 \approx 2.5ns$ is close to the period of self-oscillations above the Hopf bifurcation slightly shifting its value when noise increases.

4.3 Regime II: Below the *SNIPER*

Now we tune the parameters such that the system lies slightly below the *SNIPER* line (Fig. 3.3) [Hiz06]. In the absence of noise ($D = 0$) the only stationary solution is a stable fixed point that corresponds to a stationary accumulation front localized over a small range of wells near the collector (Fig. 4.6 (a)). The values for the contact conductivity and the voltage are $\sigma = 2.0821(\Omega m)^{-1}$ and $U = 2.99V$, respectively. Noise is switched on.

4.3.1 Noise-induced front motion

As the noise intensity is increased, the behaviour of the system changes dramatically (Figs. 4.6(b), 4.6(c) and 4.6(d)): the accumulation front remains stationary only for a while, until a pair of a depletion and another accumulation front is generated at the emitter.

As is known from the deterministic system (see previous chapter), this dipole injection depends critically upon the emitter current [Ama04]. Here it is triggered by noise at the emitter (we have in fact verified that the same scenarios occur if noise is applied locally only to the wells near the emitter). Because of the global voltage constraint (Eq. (2.4)) the growing dipole field domain between the

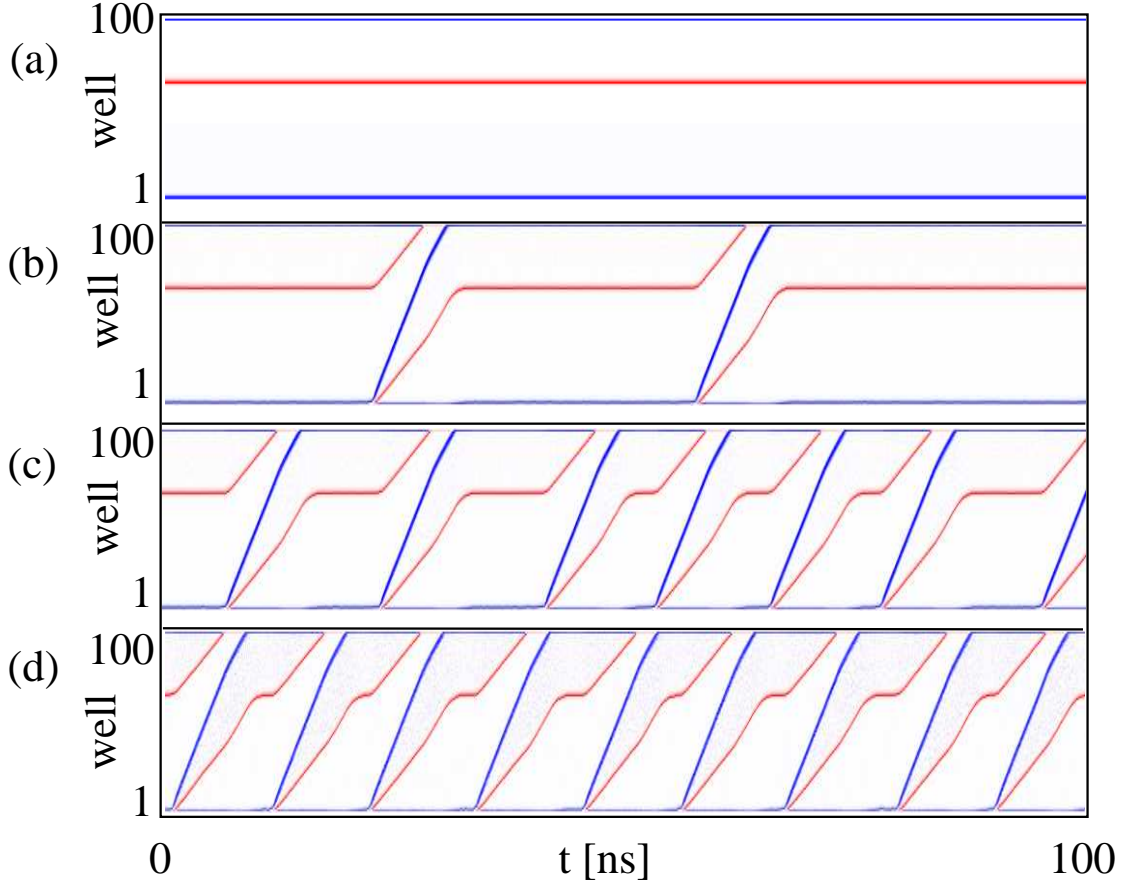


Figure 4.6: Noise-induced front motion. Noise intensity (a) $D = 0$ (no noise), (b) 0.5, (c) 0.7 and (d) $1.7 \text{ As}^{1/2}/\text{m}^2$. $\sigma = 0.266(\Omega m)^{-1}$ and $U = 1V$. Parameters as in Table 2.1.

injected depletion and accumulation fronts requires the high field domain between the stationary accumulation front and the collector to shrink, and hence the accumulation front starts moving towards the collector. For a short time there are two accumulation fronts and one depletion front in the sample, thereby forming a tripole, until the first accumulation front reaches the collector and disappears. When the depletion front reaches the collector, the remaining accumulation front must stop moving because of the global constraint (Eq. (2.4)), and this happens at the position where the first accumulation front was initially localized. After some time noise generates another dipole at the emitter and the same scenario is repeated.

4.3.2 Coherence Resonance

The fact that noise may play a constructive role rather than being an unwanted feature in a nonlinear dynamical system has been well established in the field of statistical physics. The phenomenon of *stochastic resonance* (SR) was the first expression of the above principle: Consider an overdamped particle in a periodically modulated double-well potential subjected to fluctuations. At an optimal noise level, synchronized hopping between the wells is achieved. In the works of Benzi *et al.* [Ben81] and Nicolis [Nic81b] a bistable model for the global climate explained the periodically recurrent ice ages, based on the mechanism of SR. Experimentally, SR was first manifested in a Schmitt trigger device [Fau83], with the signal-to-noise ratio showing a resonance peak at a finite noise intensity. Since then, SR has been extensively studied in a wide variety of systems ranging from ring lasers [Mcn88] to prey detection mechanisms in the crayfish [Dou93] and human visual perception modelling [Sim97]. For a comprehensive review see [Gam98, Ani99].

Almost a decade after SR was first proposed, Gang Hu *et al.* [Hu93a] reported a phenomenon which they called *stochastic resonance without periodic forcing*. They showed how noise influences the coherent motion stimulated by the *intrinsic* dynamics of a system when the external signal is absent. This phenomenon was later on named *internal* [Nei97] or *autonomous stochastic resonance* [Lon97], finally receiving its present name, *coherence resonance* (CR), by the authors Pikovsky and Kurths [Pik97]. In that work the authors studied the FitzHugh-Nagumo model [Fit61, Nag62] under white noise driving and showed that the regularity in its spiking behaviour has a nonmonotonic resonance dependence on the noise intensity. Since then CR has been strongly associated with excitable systems [Mik90], i. e. systems in which a sufficiently strong perturbation may “kick” them over a threshold resulting in a large excursion in phase space. Many works have been carried out in the field of CR, theoretical as well as experimental. For a review see [Lin04].

4.3.3 Coherence Resonance in the superlattice

The superlattice below the *SNIPER* can very well be considered as an excitable system and therefore the observation of CR is to be expected. From the spatio-temporal picture (Fig. 4.6 (b)) one can see that there are two distinct time scales in the system. One is related to the time the depletion front takes to travel through the superlattice. The other time scale is associated with the time needed for a new depletion front to be generated at the emitter. These two time scales are also visible in the noise-induced current oscillations shown in Fig. 4.7.

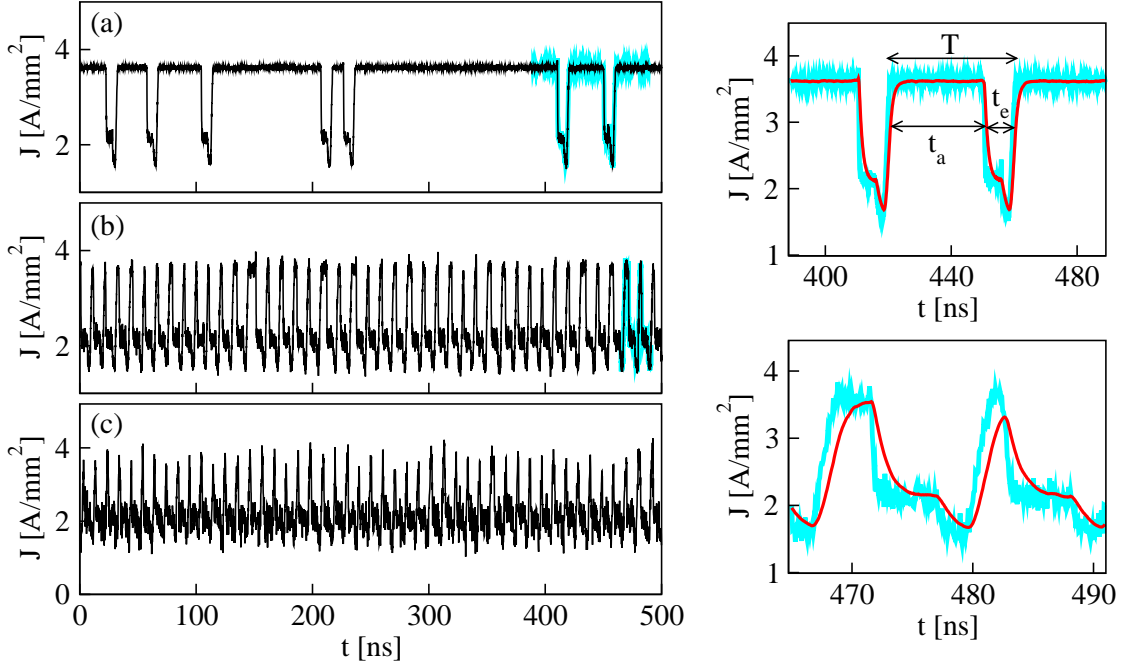


Figure 4.7: Noise-induced oscillations in the superlattice (compare equation (4.1)). Noise intensity (a) $D = 0.5$, (b) 1.7 and (c) $5.0 \text{ As}^{1/2}/\text{m}^2$. In the right side, enlarged parts (cyan) of the time series are plotted. The red thick line shows the filtered current density (according to Eq. (5.3)), with cutoff frequency $\alpha = 10^9 \text{ s}^{-1}$. The interspike interval T is the sum of the activation time t_a and the excursion time t_e . $\sigma = 0.266(\Omega m)^{-1}$ and $U = 1V$. Parameters as in Table 2.1.

The time series of the current density are in the form of a pulse train with two characteristic times: The activation time, which is the time needed to excite the system from this stable fixed point (time needed for a new depletion front to be generated at the emitter) and the excursion time which is the time needed to return from the excited state to the fixed point (time the depletion front needs to travel through the device). Low noise is associated with large activation times and small, almost constant, excursion times, while as the noise level increases activation times become smaller and at sufficiently large D vanish.

A very common measure for quantifying the variability of spike timing is the so-called *normalized fluctuations of pulse durations* [Pik97], also known as *coefficient of variation* [Lin04], given by the ratio of the standard deviation of the interspike

intervals (ISI) to their mean.

$$R_T = \frac{\sqrt{\langle \Delta T^2 \rangle}}{\langle T \rangle}. \quad (4.13)$$

Here $\langle T \rangle$ is the mean and $\langle \Delta T^2 \rangle = \langle T^2 \rangle - \langle T \rangle^2$ is the variance of the interspike interval T .

At low D the spike train looks irregular, and the interval between excitations (mean interspike-interval $\langle T \rangle$) is relatively large and random in time. At moderate noise, the spiking is rather regular therefore suggesting that the mean interspike-interval does not vary substantially. Further increase of noise results in a highly irregular spike train with very frequent spikes.

In Fig. 4.8(b) the decrease of $\langle T \rangle$ as a function of D is shown thus demonstrating that the mean interspike-interval is strongly controlled by the noise intensity. In the inset of Fig. 4.8(b) the corresponding spectral peak frequency ω_0 shows a linear scaling for small D (regime bounded by two red lines). As D increases, ω_0 grows similarly to the inverse of $\langle T \rangle$.

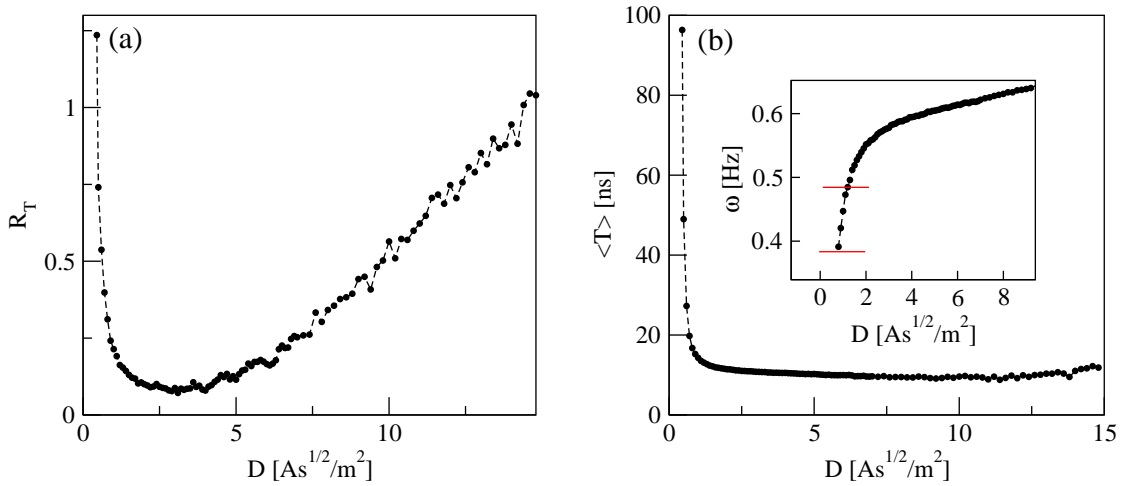


Figure 4.8: (a) Normalized variance of the interspike interval R_T and (b) mean interspike interval $\langle T \rangle$ in dependence on the noise intensity D . Calculated from time series of the filtered total current density (according to Eq. (5.3)) containing 1000 periods. Inset of (b) shows basic frequency versus D , as extracted from spectra averaged over 30 realizations, each of length $T = 1600\text{ns}$. $\sigma = 0.266(\Omega m)^{-1}$ and $U = 1V$. Parameters as in Table 2.1.

In Fig. 4.8(a), R_T shows a non-monotonic behaviour in dependence on D , exhibit-

ing a minimum at moderate noise intensity. This resonance-like behaviour is a first indicator of coherence resonance in our system. In order to provide more evidence for coherence resonance we consider the two previously used measures, the coherence factor β and the correlation time t_{cor} , as a function of the noise intensity, as well. The result is summarized in Fig. 4.9. In Fig. 4.9(a) the correlation time

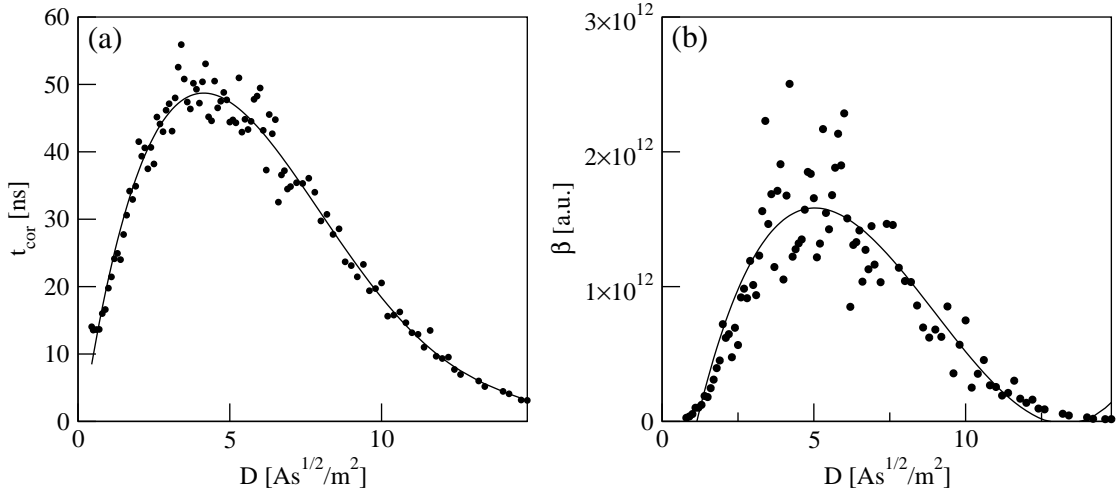


Figure 4.9: (a) Correlation time t_{cor} and (b) coherence factor β in dependence on the noise intensity D . Averages of 30 time series of length $T = 1600\text{ns}$ each, have been used. $\sigma = 0.266(\Omega m)^{-1}$ and $U = 1V$. Parameters as in Table 2.1.

shows nonmonotonic behaviour. Similarly, the coherence factor (4.9(b)), reaches a maximum at optimal noise. The correlation time data are smoother than those of the coherence factor and this is due to the fact that the latter is a function of the averages, over an ensemble, of three measures (spectral height, width and main frequency). In Fig. 4.10 the spectra for various noise intensities are shown. The spectral width clearly becomes narrower at an intermediate noise level and therefore we have gained full evidence of coherence resonance in our system.

At this point it is useful to make a comparison with the other prototype model for coherence resonance, the FitzHugh-Nagumo system. This system, in the excitable regime, has a supercritical Hopf bifurcation and a small perturbation may lead to a Canard explosion resulting in a large excursion in phase space. This regime is sensitive to noise and coherence resonance is confirmed in terms of both correlation time t_{cor} and normalized fluctuation of pulse durations R_T [Pik97]. Moreover, in [Lin99a] an analytical expression for R_T as a function of the noise intensity was found, as well as for the spiking frequency (or rate) in the limit of small and large noise. In [Pra07] analytical approximations of t_{cor} and the mean frequency

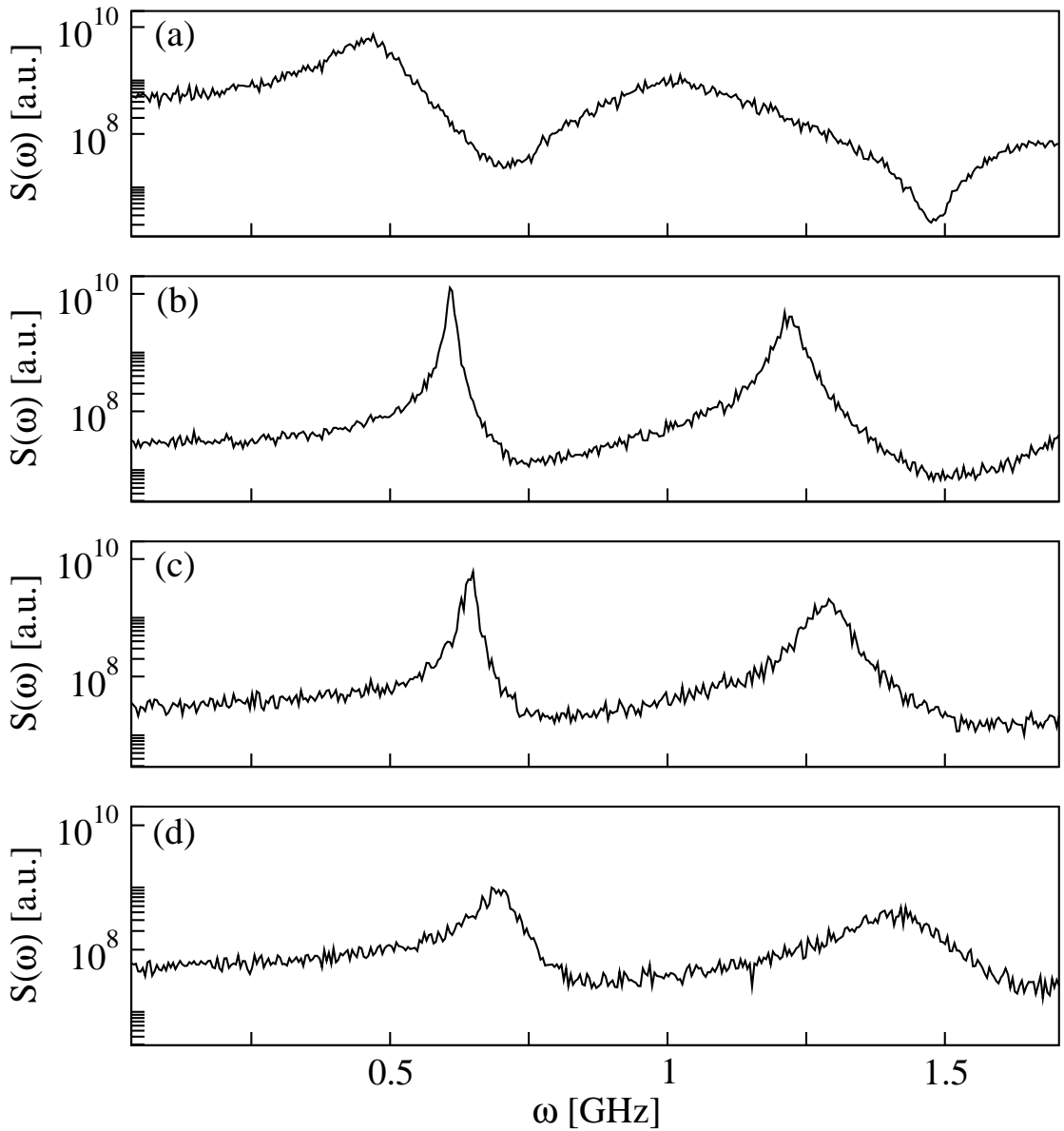


Figure 4.10: Fourier power spectral density of the total current density $J(t)$ for noise intensity (a) $D = 1.0$, (b) $D = 5.5$, (c) $D = 9.6$ and (d) $D = 14.8 \text{As}^{1/2}/\text{m}^2$. Averages over 30 time series realizations of length $T = 1600 \text{ns}$ have been used. $\sigma = 2.0821(\Omega m)^{-1}$ and $U = 2.99 \text{V}$. Parameters as in Table 2.1.

were found for the FitzHugh-Nagumo model. In [Lin99], for small noise, it was shown that the spiking rate increases following an exponential dependence on the inverse of the noise intensity (Kramers law [Kra40]). The same was shown in

the limit of small noise for the one-dimensional normal form of the *SNIPER* in [Lin03]. Overall, both models show qualitatively a similar nonmonotonic increase of the frequency in dependence on the noise.

In both models the coherence resonance is due to the competing effects of the stochastic activation time, which decreases strongly with increasing noise, and the deterministic excursion time, whose variance increases at high noise intensities. However, the mechanism of activation is different: In the FitzHugh-Nagumo system there is a unique fixed point (stable) and noise must excite the system from the stable fixed point across the nonmonotonic null-isocline to trigger a large excursion in phase space, whereas in the *SNIPER* model there are two more (unstable) fixed points, and noise must excite the system from the stable fixed point upstream against the deterministic vector field towards the saddle-point, from where it continues along the heteroclinic orbit back to the stable fixed point.

4.3.4 Application as noise sensor

The observed effects of noise in our model are very important in terms of experiments, where noise can induce oscillations by forcing stationary fronts to move. Noise triggers the injection of fronts into the system and thus determines the frequency of the resulting current oscillations, whereas the front propagation velocity is insensitive to the noise level. This opens promising applications of superlattices as fast noise sensors which convert the noise intensity into frequency. Such sensors could potentially be used for measuring temperature, pressure, electromagnetic bias, or other parameters which affect the level of noise in a superlattice. Of course, those parameters would also affect the deterministic state of the system. However, since the sensitivity of the mean interspike interval and thus of the mean frequency upon the noise intensity is particularly strong for small noise intensity near the coherence resonance, this effect can be expected to dominate as long as no other bifurcations are induced. Thus, further experimental study would be very interesting.

4.4 Comparison of the results obtained in Regimes I and II

We have studied the effect of noise in the superlattice in the vicinity of two different types of bifurcations: Supercritical Hopf bifurcation and *SNIPER*. In the first case, noise induces stochastic oscillations of an almost constant frequency very close to the Hopf frequency of the deterministic system. The coherence of these oscillations

deteriorates the stronger the noise is in the system. In the spatio-temporal picture, weak front motion is observed, restricted around the deterministically stationary depletion front. On the other hand, in the case of the *SNIPER*, more interesting dynamics is observed. Noise manages to trigger clear front motion, with tripoles travelling through the entire device. In addition, the excitable nature of the system results in the existence of two time scales which are affected in a different way by noise. The competition between them results in a resonance peak in the coherence of the noise-induced oscillations, resulting, thus, in the verification of coherence resonance, which is absent in the case of the Hopf bifurcation. The coherence factor shows resonance-like behaviour in both cases, but the mechanism is different [Ush05, Flu06, Flu07b]. In the case of the Hopf bifurcation it is due to the competition between the growth of spectral height and width. In the case of the *SNIPER*, it arises from the nonmonotonic dependence on the spectral width upon the noise intensity, which provides evidence for coherence resonance.

5 Control of noise-induced dynamics

In contrast to the problem of controlling deterministic chaos, for which a number of methods have been proposed and successfully applied [Sch99c, Sch07], control of noise-induced and noise-mediated motion is a significantly less studied concept. In the first case, there is no oscillatory dynamics in the absence of noise. The deterministic system rests in a stable steady state, e.g. a stable fixed point, and may be pushed out from it by random fluctuations. On the other hand, in the case of noise-mediated motion, the system already exhibits deterministic oscillations. The addition of noise may not only smear-out those oscillations but may also induce qualitatively new structures and dynamics, like coherence resonance [Hu93a, Pik97], studied in the previous chapter.

The ability to control the properties of noisy oscillations (both noise-induced and noise-mediated) is very often of practical relevance. This usually implies the enhancement in the regularity of motion. However, in some cases, for instance in medical or biological applications, too much regularity is unwanted since it may lead to damaging consequences, e.g. epilepsy or Parkinson's disease [Tas02].

Previous works mainly concentrate on the control of stochastic oscillations in low-dimensional simple models [Chr95a, Lan97, Mas02, Jan03, Bal04, Sch04b, Pom05a, Hau06, Sch06, Pom07, Pra07, Flu07, Jan07], or self-oscillations in the presence of noise [Gol03] while control of noise-induced dynamics in spatially extended systems [Hiz05, Ste05a, Bal06, Hiz08, Sch08a] seems still to be an open problem. The question we wish to answer here is how control can play a role in the improvement of the properties of the noise-induced dynamics that the superlattice model shows, in both regimes studied in the previous chapter.

5.1 Time-delayed feedback

In this section, we study the effect of a time-delayed feedback of the form

$$F(t) = K(s(t) - s(t - \tau)). \quad (5.1)$$

Time-delayed feedback was originally proposed in the context of chaos control [Pyr92] as an alternative to the famous OGY method developed earlier by Ott, Grebogi and Yorke [Ott90]. The idea is to achieve stabilization of unstable periodic orbits (UPOs) by adding, to a chaotic system, a control force in the form of the difference between a system variable at time t and at a delayed time $t - \tau$. Here $s(t)$ is an output signal of the system, τ is a delay time, and K is the feedback strength. This is a non-invasive method in the sense that the control force vanishes once the desired orbit is reached.

Apart from the control of UPOs the stabilization of unstable fixed points can also be achieved by time-delayed feedback [Hoe05, Dah07]. This method proved to be very powerful and has been successfully applied to various physical systems since then [Sch99c, Sch07]. The scheme was improved by Socolar *et al.* [Soc94], and other variants have been elaborated [Kit95, Bab02, Bec02, Unk03, Sch04]. Socolar's scheme is called extended time-delayed autosynchronization (ETDAS) and has been applied not only to deterministic systems [Fra99, Sch03a, Bec02, Unk03, Sch03a, Sch06c, Dah07] including fixed points but to stochastic systems as well [Pom07, Sch08a].

An easy way to implement control in the superlattice model is to choose the output signal to be the total current density, $s(t) = \bar{J}(t)$ and simply add the control force to the external voltage U , i.e.

$$U = U_0 - K(\bar{J}(t) - \bar{J}(t - \tau)), \quad (5.2)$$

where U_0 is the time-independent external voltage bias and \bar{J} , filtered by a low-pass filter, is the total current density

$$\bar{J}(t) = \alpha \int_0^t J(t') e^{-\alpha(t-t')} dt', \quad (5.3)$$

with α being the cutoff frequency [Sch03a]. This control scheme is depicted in Fig. 5.1. Since both voltage and total current density are externally accessible global variables, such a control scheme is easy to implement experimentally. The low-pass filter in the current density was introduced initially for the effective control of chaotic motion in the superlattice [Sch03a]. Due to the well-to-well hopping of the depletion and accumulation fronts, the current is modulated by fast small-amplitude oscillations. These high-frequency oscillations render the control loop unstable as $J(t)$ is fed back to the system and therefore they need to be filtered out. Stochastic oscillations, like chaotic ones, exhibit the same high-frequency

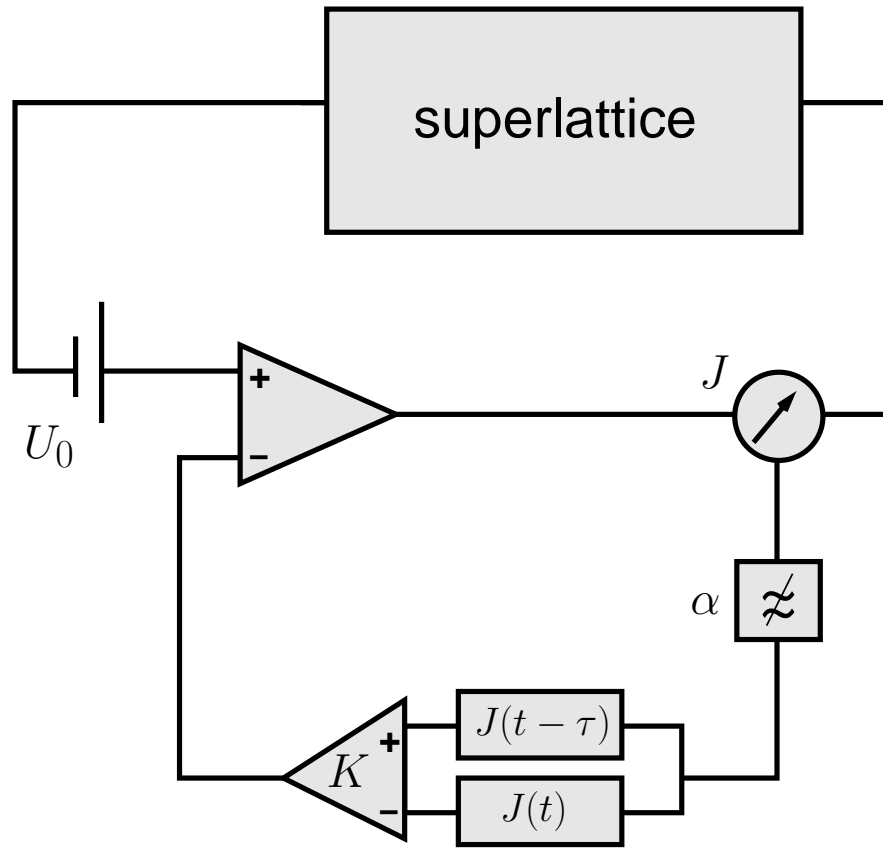


Figure 5.1: Global time-delayed feedback control scheme in the superlattice including the low-pass filter with cutoff frequency α and the time-delayed feedback loop K , according to Eq. (5.2).

oscillations and thus we apply this filter here, too.

5.2 Regime I: Below the Hopf bifurcation

We now prepare the system below the Hopf bifurcation and apply the control force of Eq. (5.2) to the system [Hiz05]. In the absence of delay the system has one stable fixed point. In the addition of noise, oscillations around this fixed point are induced with increasing amplitude and irregularity as the noise intensity grows, shown in the previous chapter. Of interest is to see how and to what extent control is able to affect the properties of the stochastic dynamics and, in particular, the coherence and characteristic time scales of the noise-induced oscillations. Apart from the noise intensity D , two additional parameters due to control, the control

strength K and the time delay τ , add to the various possibilities of manipulating the systems behaviour.

5.2.1 Delay-induced Hopf instability

First we will examine the system under control alone, i. e. with the noise switched off. The delay τ renders the system infinite-dimensional affecting the eigenvalue spectrum of the fixed point. In the free system the fixed point possesses a finite number of eigenvalues. Delay generates infinitely many eigenvalues, the real part of which determines the stability of the fixed point. In variation of either of the two control parameters, K and τ , it is possible that the least stable eigenvalue attains a positive real part yielding, thus, the fixed point unstable. Delay may, therefore, induce the birth of a stable limit cycle via a Hopf bifurcation. We numerically track this delay-induced bifurcation in the K - τ plane and obtain the bifurcation diagram shown in Fig. 5.2. In the cyan area the fixed point remains stable. For all

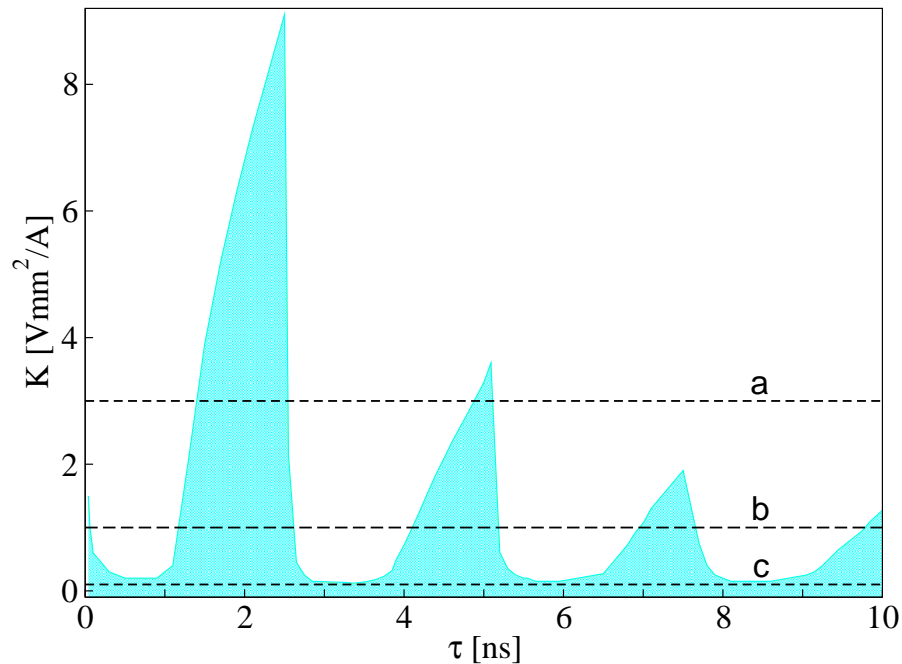


Figure 5.2: Bifurcation diagram in the K - τ plane. Cyan area denotes the parameter regime for which delay does not induce a Hopf bifurcation whereas white area denotes the regime where delay induces oscillations. The dashed lines a, b and c correspond respectively to subfigures (a), (b) and (c) of Fig. 5.3 and Fig. 5.6. $U = 1V$ and $\sigma = 0.266(\Omega m)^{-1}$. Parameters as in Table 2.1.

other values of K and τ , the fixed point becomes unstable and a limit cycle is born. A very similar bifurcation diagram was found in [Ste05a], for a reaction-diffusion system, where an analytical expression could confirm the numerical simulation. The line bounding the cyan area in Fig. 5.2, marks the Hopf bifurcation line and shows a modulation in τ . In the following section the mechanism behind this modulation will be explained in detail.

Our initial aim was to control the oscillations induced by noise below the Hopf bifurcation. Here, however, it is shown that control itself may impose a delay-induced frequency. By keeping K fixed (above a minimum value) and varying τ , there are regions (cyan) where the oscillations are induced exclusively by noise, and regions (white) where delay generates a limit cycle which noise simply smears out. The oscillations induced exclusively by noise have an almost constant frequency, close to the deterministic frequency, as shown in the previous chapter. The frequency imposed by delay, however, depends on the choice of τ as will be shown in the next section. Therefore, in terms of time scales, we can say that delay has a dominating role upon noise. Regardless of whether one is in the cyan or white area, the oscillation frequency will be set by the delay. On the other hand, the coherence properties of the oscillations depend strongly on the position in the bifurcation diagram. In the white area the motion is expected to be most regular due to the delay-induced deterministic oscillatory dynamics, which is rather trivial. It therefore makes sense to speak of controlling the coherence of noise-induced oscillations in the cyan areas only.

5.2.2 Influence of the control on the coherence

Now we study the regularity of the system's motion under noise and control as a function of the parameters D and τ . Since the coherence factor, introduced in the previous chapter, and the correlation time are equivalent measures, we will express the regularity in terms of correlation times which are less difficult to compute.

Varying the time delay τ

First, the control amplitude K and the noise intensity D will be kept fixed and the dependence upon the time delay will be studied. For the reasons described above, one should avoid being in a regime where delay induces a limit cycle because then the explanation for high coherence is trivial. However, due to the form of the bifurcation diagram in Fig. 5.2, variation of τ brings the system in and out of such regions, unless K is fixed at a very small value, marked by the lowest dashed line in Fig. 5.2. Such a value, however, is so small that the delayed feedback has

little effect upon the correlation time. It is, nevertheless, of interest to scan τ at higher values of K denoted by the upper dashed lines in the same figure. The noise intensity will be fixed at a rather low level, $D = 1.0As^{1/2}/m^2$. In Fig. 5.3 the correlation time is plotted over τ for three values of K . In Fig. 5.3 (a) K is

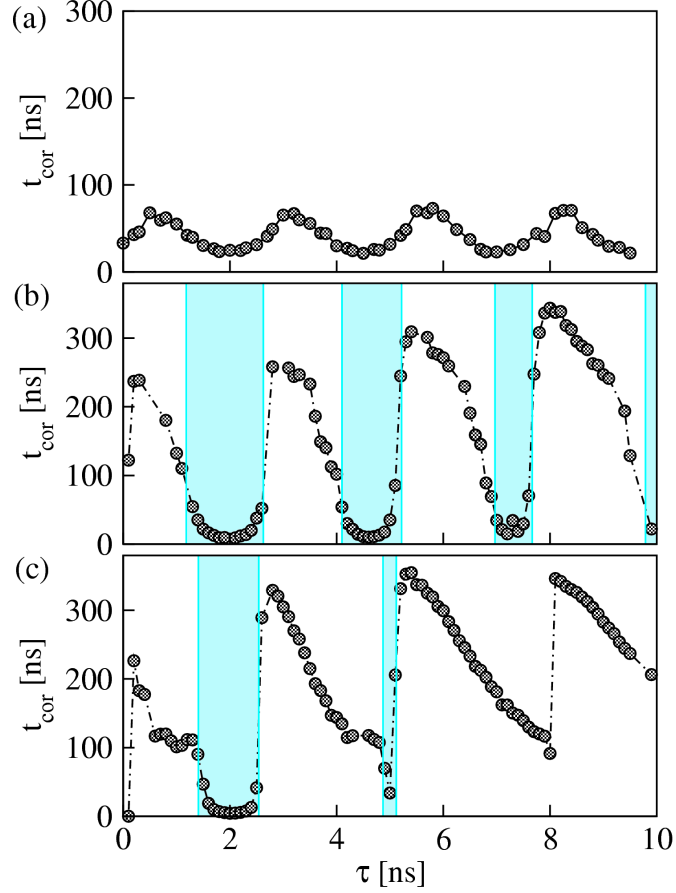


Figure 5.3: Correlation time t_{cor} in dependence on the time delay τ for different values of the control strength: (a) $K = 0.1$, (b) $K = 1.0$ and (c) $K = 3.0Vmm^2/A$. $D = 1.0As^{1/2}/m^2$ in all three plots. Averages over 30 time series realizations of length $T = 1600ns$ have been used. The cyan shaded regions mark the τ intervals where no delay-induced oscillations exist, according to Fig. 5.2. $U = 1V$ and $\sigma = 0.266(\Omega m)^{-1}$. Parameters as in Table 2.1.

not large enough to allow for a delay-induced limit cycle. The correlation time exhibits a slight oscillatory behaviour under variation of τ , showing local maxima at “optimal” τ and local minima at “non-optimal” τ . Optimal delays correspond to more coherent motion, whereas non-optimal delays to less regular oscillations.

The modulation of the correlation time in τ was observed in generic models ([Jan03, Pom05a, Hau06]) and in another semiconductor device in [Ste05a]. The reason is the following: As already mentioned, due to delay, the fixed point possesses an infinite number of eigenvalues.

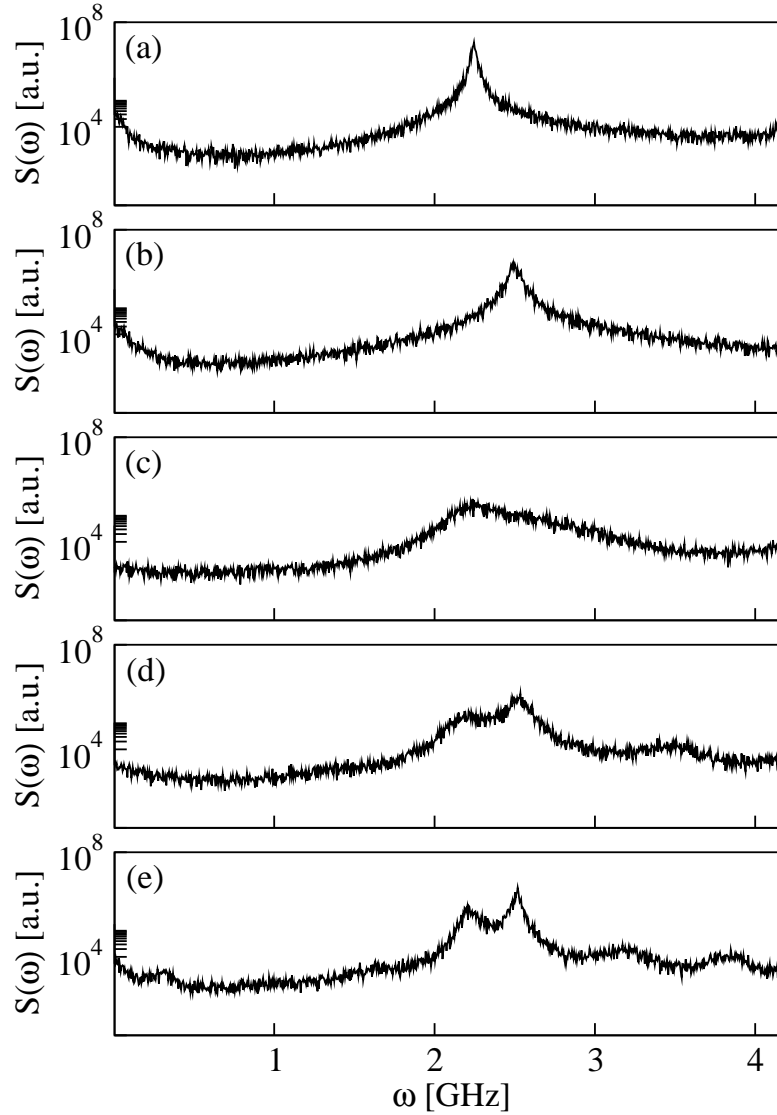


Figure 5.4: Fourier power spectral density of the total current density $J(t)$ for $D = 0.1 \text{As}^{1/2}/\text{m}^2$, $K = 1 \text{Vmm}^2/\text{A}$ and varying time delay: (a) $\tau = 1.3$ (b) $\tau = 2.5$, (c) $\tau = 4.5$, (d) $\tau = 7.4$ and (e) $\tau = 10 \text{ns}$. Averages over 30 time series realizations of length $T = 1600 \text{ns}$ have been used. $U = 1 \text{V}$ and $\sigma = 0.266(\Omega\text{m})^{-1}$. Parameters as in Table 2.1.

Under variation of τ , the real part oscillates with the time delay and with it, the degree of stability of the fixed point as well, leading to modulation of the coherence of the stochastic motion. The latter is reflected on the correlation time, whose local maxima occur for real parts closer to zero, i. e. least stable ones.

Similar behaviour is observed for higher values of K in Fig. 5.3 (b) and (c), where the correlation time attains higher values at delay intervals outside the cyan shaded areas where delay imposes a regular motion. Although in these cases the regularity is “artificial”, one can still distinguish between “optimal” and “non-optimal” τ leading to a similar modulation of t_{cor} as in Fig. 5.3 (a). The increase and decrease of coherence as τ varies is also demonstrated in the power spectra (Fig. 5.4), where the spectral width becomes narrower at optimal delays and wider at non-optimal τ , corresponding to more, and less regular motion, respectively.

Varying the noise intensity D

In the previous chapter it was shown that the correlation time has a monotonic dependence on the noise intensity D , i. e. the stronger the noise, the less coherent the oscillations become. What interests us further here, is whether control can affect the correlation time upon variation of D . The selection of the control

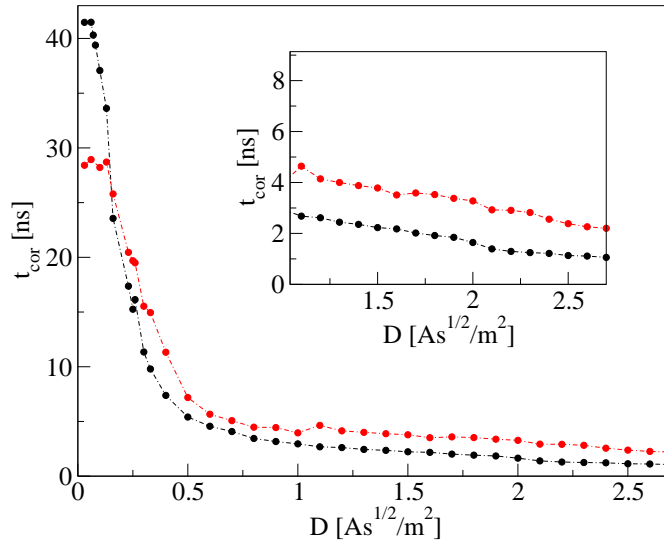


Figure 5.5: Correlation time t_{cor} in dependence on the noise intensity D for $K = 0$ (black) and $(K, \tau) = (3Vmm^2/A, 2ns)$ (red). Calculated from an average of 30 time series each of length $T = 1600ns$. Inset shows blow-up at higher noise intensities where control improves the correlation time. $U = 1V$ and $\sigma = 0.266(\Omega m)^{-1}$. Parameters as in Table 2.1.

parameter values will be made on the basis of the previous analysis: We should select a time delay close to an optimal value where the correlation time showed an increase and at the same time be sure that we are still in a regime in the (K, τ) plane where no delay-induced Hopf bifurcation takes place. Such values are, for instance, $K = 1Vmm^2/A$ and $\tau = 2.7ns$. Plotting, however, the correlation time t_{cor} over the noise intensity D for these values one hardly notices a difference to the free system.

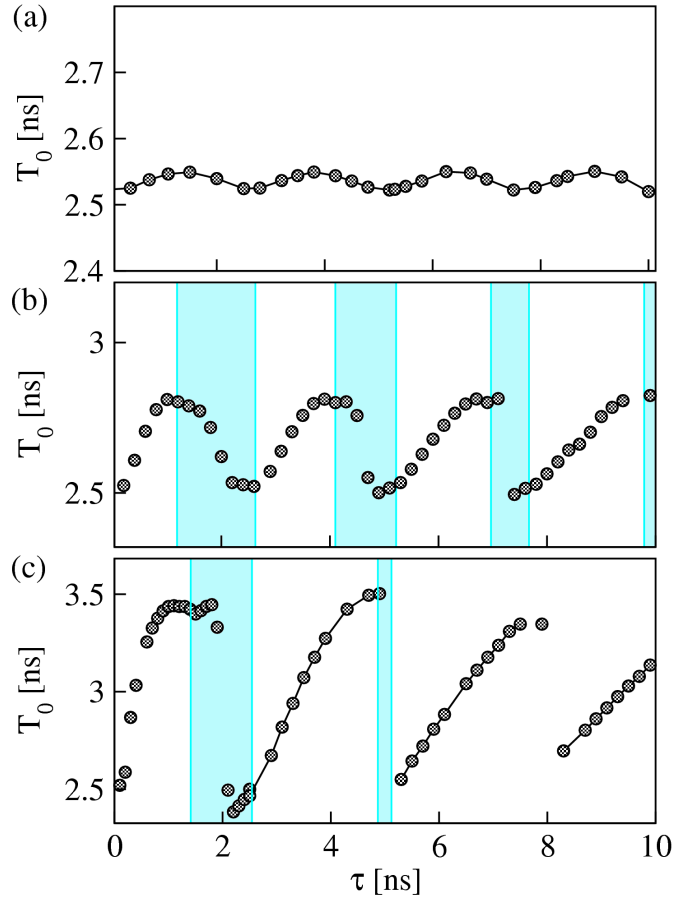


Figure 5.6: Main period T_0 in dependence on the time delay τ for different values of the control strength: (a) $K = 0.1$, (b) $K = 1.0$ and (c) $K = 3.0Vmm^2/A$. $D = 1.0As^{1/2}/m^2$ in all three plots. The cyan shaded regions mark the τ intervals where no delay-induced oscillations exist, according to Fig. 5.2. $U = 1V$ and $\sigma = 0.266(\Omega m)^{-1}$. Parameters as in Table 2.1.

The control strength must attain a higher value and thus we fix $K = 3Vmm^2/A$ and shift τ slightly closer to the deterministic Hopf time scale in order to remain

in the cyan area of Fig. 5.2. The result is shown in Fig. 5.5 where red corresponds to the controlled case. It is clear that for higher noise intensities in particular, control manages to improve the regularity of the noise-induced oscillations.

5.2.3 Control of time scales

Here the dependence of the motion's time scales on the time delay τ will be shown. Already from the power spectra of Fig. 5.4 we saw how the position of the main frequency, around which the power spectrum maximum is centered (and therefore its inverse), varies with the delay. Moreover, additional harmonic peaks occur at larger time delays τ .

We make sure that the delay τ is chosen such that it lies in the cyan area of Fig 5.2. We extract the main frequency from the spectra and plot its inverse over τ (Fig. 5.6). Similarly to the correlation time, the time scales, also, exhibit an oscillatory behaviour under variation of τ which is stronger and tends to a piecewise linear dependence as K increases (Fig. 5.6 (c)).

The same behaviour has been found for the simple models without spatial degrees of freedom and explained analytically via a linear stability analysis [Jan03, Bal04] or via the power spectrum [Sch04b, Pom05a]. There it was shown that the eigenperiod is proportional to the inverse of the imaginary part of the eigenvalue of the fixed point which itself depends linearly on τ , for large τ . Therefore, we note that while the position of the main peak of the spectrum is insensitive to the noise level in the case without control, it is indeed possible to shift its position by the proposed time-delayed feedback scheme

5.3 Regime II: Below the *SNIPER*

In this section we will study the effect of time-delayed feedback on the front motion induced by noise when the system is prepared in the other dynamical regime presented in the previous chapter, namely below the *SNIPER*. We will follow the same methodology applied in the case of the Hopf bifurcation: First examine the system under delay only and then with the noise switched on, study the influence of control on the system's time scales and coherence properties.

5.3.1 Delay-induced homoclinic bifurcation

In the absence of both delay and noise the only stable attractor in phase space is the stable node. Regardless of the initial condition, all trajectories end there.

In particular, when selecting the initial condition on the unstable manifold of the saddle-point, the system performs a long excursion along the invariant circle before ending in the stable node. This deterministic path is affected by the delay for given combinations of the two control parameters, K and τ . By keeping the delay τ fixed and varying the control amplitude K we track the orbits. During the first few nanoseconds the system acts as it would in the absence of delay, repelled by the saddle-point. Control is switched on at $t = \tau = 2ns$ when the control force begins to act. The interval $[0, 2ns]$ serves as initial condition of the delay equation. This becomes evident in a “twist” in the trajectory just before the orbit reaches the stable node. For a moment it looks as if the system is attracted to the saddle-point instead of the node. This may be understood as follows: The control force shortly pulls the system off the phase space of the uncontrolled system pushing it towards the stable manifold of the saddle-point. At a critical value $K_c = 0.0064375Vmm^2/A$, the system is indeed “swallowed” by the saddle and the trajectory closes in a homoclinic orbit (see Chapter 6). In the top panel of Figs. 5.7(b) - 5.7(d) the trajectories for three values of K approaching this critical value are shown.

Due to the high dimensionality of the system, which is blown up to infinity due to the delay, the above mechanism is not clearly demonstrated in a 2-dimensional projection in phase space. One must zoom in carefully in order to see the deviation from the deterministic path due to delay (middle panels of Fig. 5.7). For better comparison, in Fig. 5.8, the part approaching asymptotically the stable node for all 4 values of K is blown up.

This deviation is even better visible in the bottom panels of Fig. 5.7 where the final part of the electron density time series of n_{65} is plotted. In (a) the deterministic trajectory is plotted and the thick grey solid and dotted line marks the position of the stable node and the saddle-point, respectively. It is clear that, the closer one is to the homoclinic bifurcation (d), the closer to the saddle-point does the system reach and the longer the trajectory is, before ending up in the stable node. This is also evident in the global current density time series (bottom panel of Fig. 5.9). The corresponding spatio-temporal plots in the same Figure, on the other hand, provide a less clear picture of the same effect. In the following chapter we will find perfect agreement with a generic model below a *SNIPER* with delay, where this phenomenon is better visualized.

Beyond the critical value of $K_c = 0.00644Vmm^2/A$ the homoclinic orbit breaks and

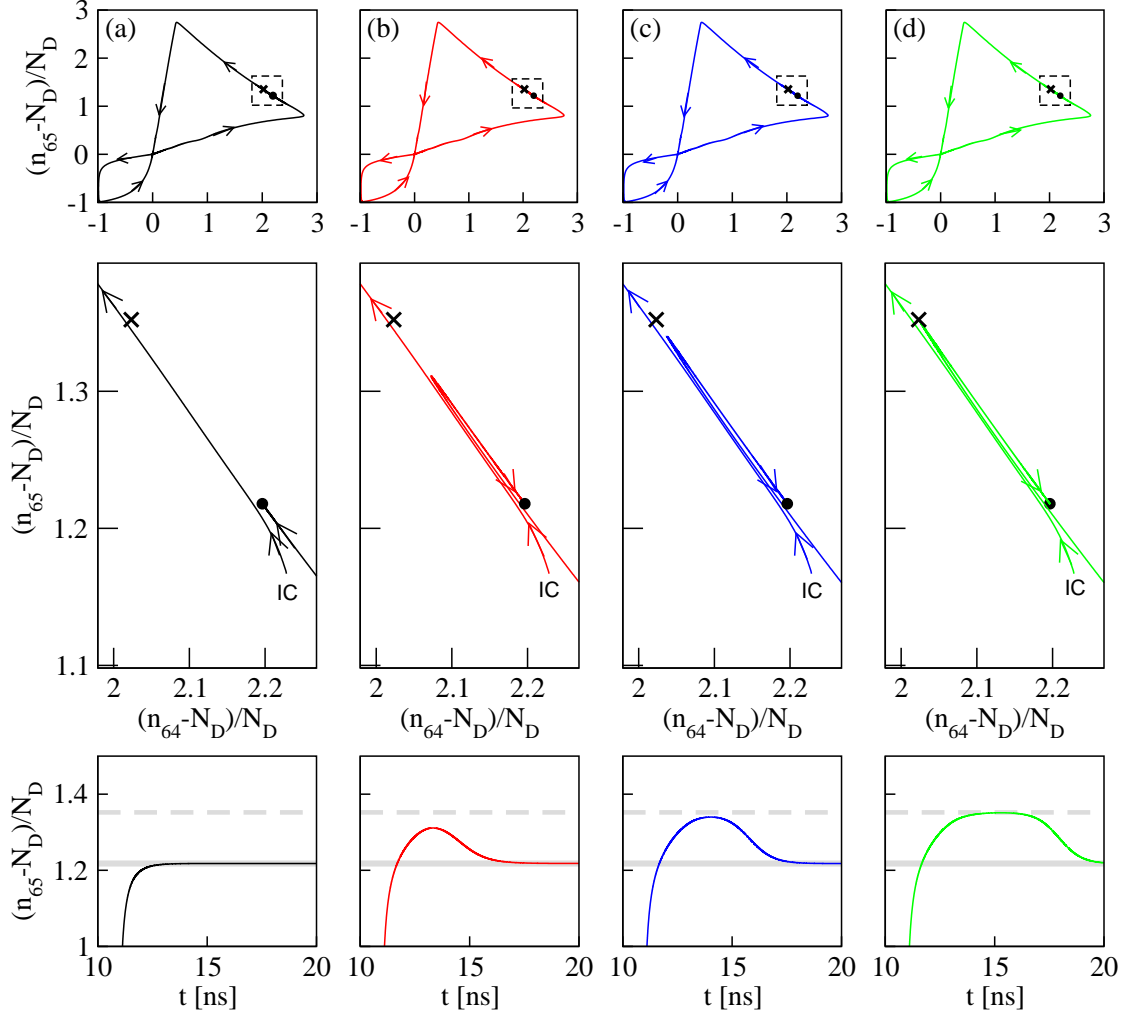


Figure 5.7: Top: Phase portrait in the (n_{65}, n_{64}) plane for fixed $\tau = 2\text{ ns}$ and (a) $K = 0$, (b) 0.006 , (c) 0.0064 and (d) $0.006437\text{ Vmm}^2/\text{A}$. Middle: Enlargement of corresponding phase portraits shown in upper plots. Cross marks the position of the saddle-point, full circle marks the position of the stable node and *IC* is the initial condition, which is the same in all figures. Bottom: Corresponding electron density time series (only the part approaching asymptotically the stable node as shown in Fig. 5.8) of n_{65} . Thick grey line denotes the value of the stable node and dotted grey line denotes that of the saddle-point. $U = 2.99\text{ V}$ and $\sigma = 2.0821(\Omega\text{m})^{-1}$. Parameters as in Table 2.1.

a limit cycle is born. In Figs. 5.10(a) - 5.10(c) the time series of the current density for three different values of K above K_c are shown. The period clearly decreases for

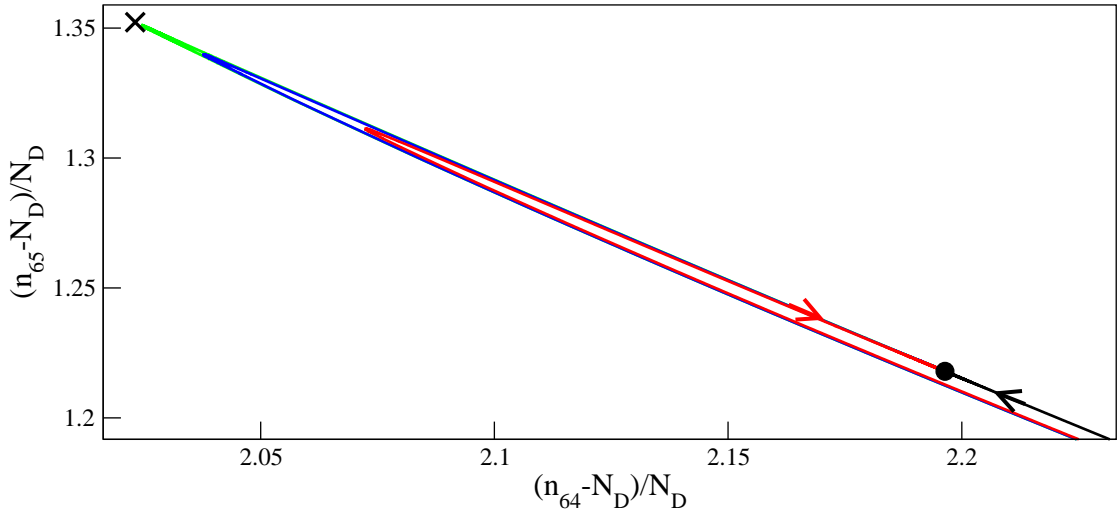


Figure 5.8: All 4 trajectories (a)-(d) of Fig. 5.7 in one plot showing part approaching asymptotically the stable node.

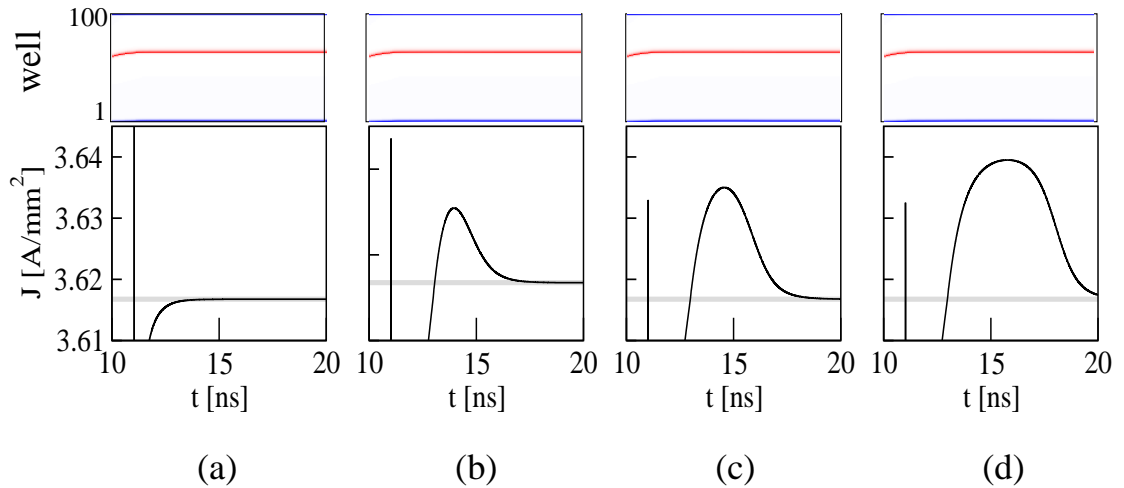


Figure 5.9: Corresponding to Fig. 5.7, spatio-temporal plots (top) and current density time series (bottom). Thick grey line denotes the current density value of the stable node. $\tau = 2$ and (a) $K = 0$, (b) 0.006, (c) 0.0064 and (d) $0.006437Vmm^2/A$, as in Fig. 5.7.

increasing K . Plotting it as a function of the control strength we obtain Fig. 5.10 (d). The period shows a characteristic scaling law [Kuz95], $T \sim \ln[K - K_c]$, shown in the inset. This law governs another type of global bifurcation, namely the homoclinic bifurcation. Following the homoclinic bifurcation in the K - τ plane we obtain the regime where control induces limit cycle oscillations. The result is

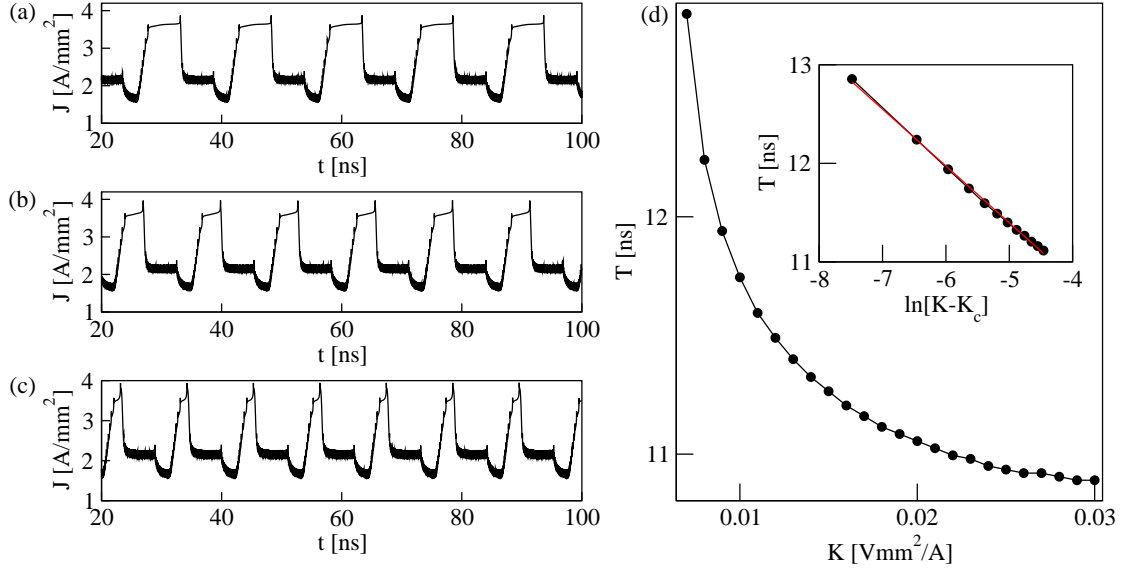


Figure 5.10: (a) Time series of the delay-induced limit cycle for fixed $\tau = 2$ ns showing period lengthening as the homoclinic bifurcation is approached from above ($K > K_c$), for $K = 0.0064379$, (b) $K = 0.007$ and (c) $K = 0.019$ Vmm²/A. (d) Period lengthening in K and characteristic scaling law governing the homoclinic bifurcation shown in inset. $K_c = 0.0064375$ Vmm²/A, $U = 2.99$ V, and $\sigma = 2.0821$ (Ωm)⁻¹. Parameters as in Table 2.1.

shown in Fig. 5.11.

Crossing the bifurcation line either in K or τ , oscillations of decreasing period are born. The scaling law of the period can also be demonstrated with the time delay as bifurcation parameter (Fig. 5.12)

5.3.2 Influence of the control on the coherence

Now we switch on noise. Coherence is expressed through the correlation time and the normalized fluctuation of pulse durations. We examine the dependence on the time delay τ and the noise intensity D .

Varying the time delay

By keeping the noise intensity fixed at $D = 1.0$ As^{1/2}/m² we first select a value $K = 0.002$ Vmm²/A outside the delay-induced limit cycle regime. This corresponds to

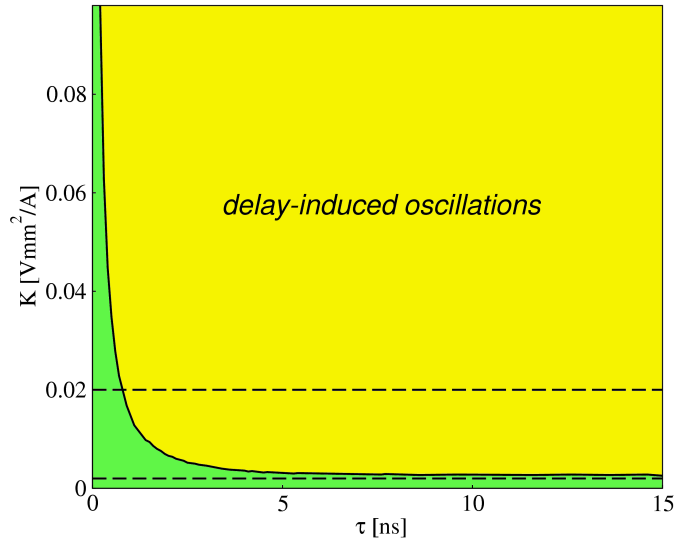


Figure 5.11: Bifurcation diagram in the K - τ plane below the *SNIPER* in the superlattice. Yellow area denotes the parameter regime for which delay-induced oscillation occur. In the green area there are no delay-induced bifurcations. The black line marks the delay-induced homoclinic bifurcation line. $U = 2.99V$ and $\sigma = 2.0821(\Omega m)^{-1}$. Parameters as in Table 2.1.

the lower dashed horizontal line in Fig. 5.11. In the right plot of Fig. 5.13(a), the correlation time is plotted versus the time delay. It exhibits a slight modulation with a period close to the period of the noise-induced oscillations, $\langle T \rangle = 14.5ns$ (see Fig. 4.8) and reaches minimum values for $\tau = n\langle T \rangle$, $n \in \mathbb{N}$. Overall, however, it remains close to the control-free value, $t_{cor} = 19.76ns$ (see Fig. 4.9 (a)).

At $K = 0.02Vmm^2/A$ inside the delay-induced limit cycle regime (upper dashed line in Fig. 5.11), this modulation is much stronger and has a period close to the delay-induced period ($T = 11ns$, see Fig. 5.10)). In addition, one can better distinguish between non-optimal and optimal values of τ at which the correlation time attains maximum values. This is shown in the right plot of Fig. 5.13 (b). For a higher noise intensity (Fig. 5.13 (c), right) the effect is similar but weaker.

Varying the noise intensity

Next we are interested in the dependence on the correlation time t_{cor} and the normalized fluctuation of pulse durations R_T as a function of the noise intensity. We keep the control strength fixed to the value corresponding to Fig. 5.13(b) (right), from which we also select an optimal and a non-optimal value of the time

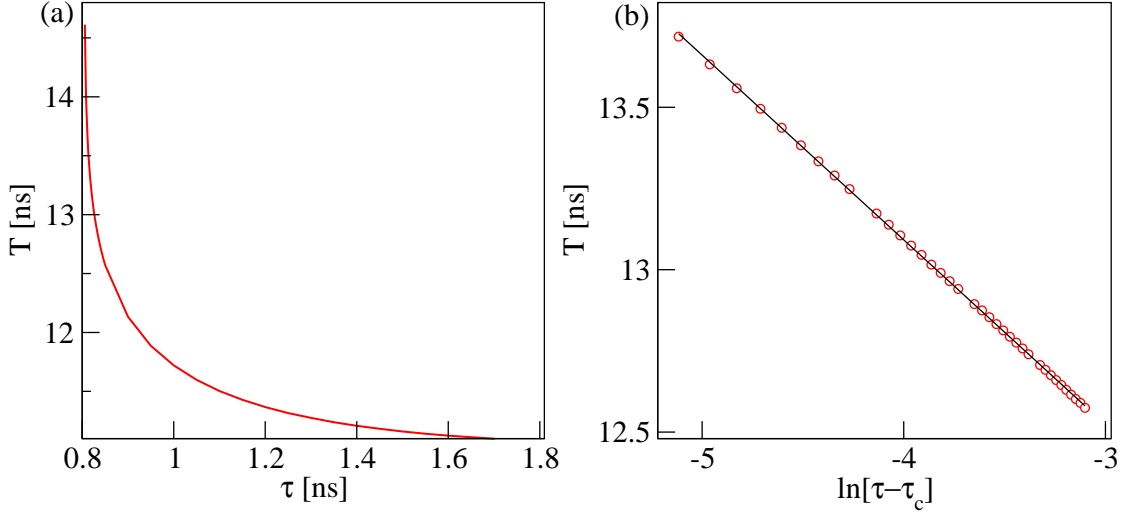


Figure 5.12: (a) Period of the delay-induced limit cycle as a function of the time delay τ . (b) Logarithmic scaling law which governs the period close to the critical value $\tau_c = 0.8ns$. Red circles correspond to numerical data whereas continuous black line corresponds to a linear fit. $K = 0.02Vmm^2/A$, $U = 2.99V$ and $\sigma = 2.0821(\Omega m)^{-1}$. Parameters as in Table 2.1.

delay and compare the result to the free system. In the left and right panel of Fig. 5.14, R_T and t_{cor} are plotted, respectively. The case $K = 0$ is shown in (Fig. 5.13(a)) for direct comparison. For both non-optimal (Fig. 5.13(b)) and optimal τ (Fig. 5.13(c)), there is an enhancement in the coherence. Correlation times attain much higher values to those of the control-free system, especially at low noise level. Similarly, R_T values are lower. In addition, for non-optimal $\tau \approx 11ns$, the effect of coherence resonance is suppressed (Fig. 5.13(b)). The correlation time shows a local maximum exactly where the uncontrolled system does, but this cannot account for coherence resonance since there are much higher values at lower noise intensities. Nevertheless, for optimal $\tau \approx 14.5ns$ (Fig. 5.13(c)), coherence resonance is maintained and both t_{cor} and R_T show a maximum and minimum, respectively, but at a lower noise intensity than in the free system. The comparison between the three cases is better visible in Fig. 5.13(d) where the three curves are plotted together.

5.3.3 Control of the time scales

We express the time scales through the mean interspike interval $\langle T \rangle$ and look at the dependence upon the time delay τ for a fixed value of the noise intensity,

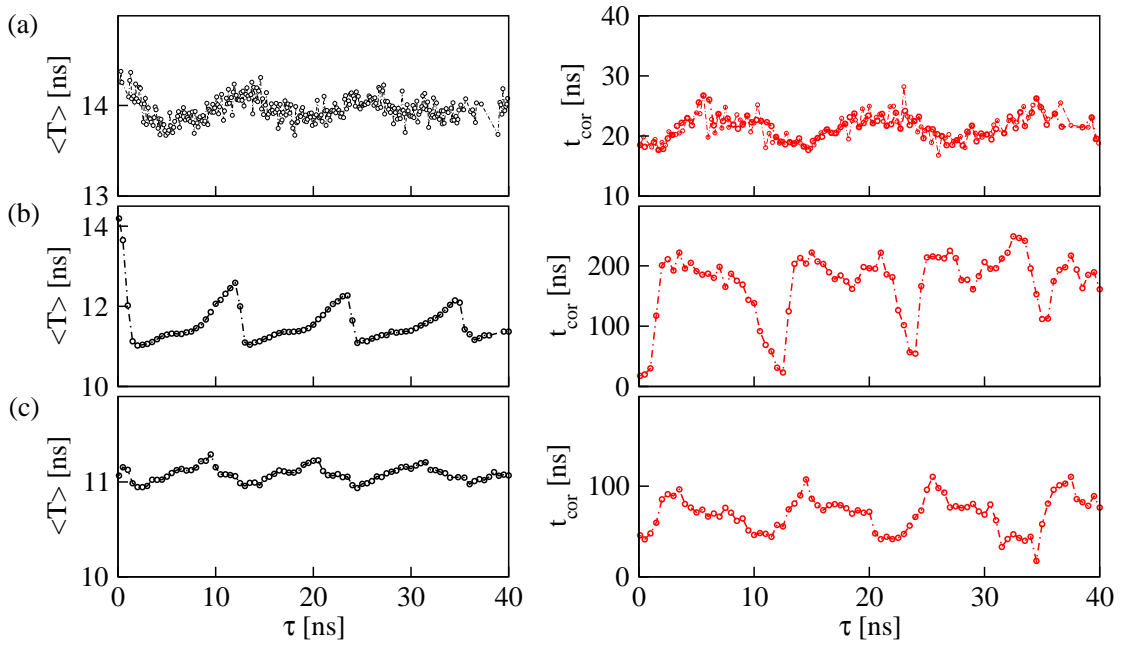


Figure 5.13: Mean interspike interval $\langle T \rangle$ (left) and correlation time t_{cor} (right) in dependence on the time delay τ . (a) Control strength $K = 0.002 Vmm^2/A$ and noise intensity $D = 1.0 As^{1/2}/m^2$, (b) $K = 0.02 Vmm^2/A$ and $D = 1.0 As^{1/2}/m^2$ and (c) $K = 0.02 Vmm^2/A$ and $D = 2.5 As^{1/2}/m^2$. Averages over 30 time series realizations of length $T = 1600 ns$ have been used for the calculation of t_{cor} and averages over 1000 periods for $\langle T \rangle$. $U = 2.99 V$ and $\sigma = 2.0821(\Omega m)^{-1}$. Parameters as in Table 2.1.

$D = 1.0 As^{1/2}/m^2$, and control strength $K = 0.002 Vmm^2/A$, chosen outside of the delay-induced oscillations regime (lower dashed line in Fig. 5.11). As shown in the left plot of Fig. 5.13 (a), $\langle T \rangle$ is slightly modulated due to the delay with a period close to the noise-induced mean period ($\langle T \rangle \approx 14.5 ns$).

In the left plot of Fig. 5.13 (b) a value of K inside the delay-induced oscillations regime is used, $K = 0.02 Vmm^2/A$ (upper dashed line in Fig. 5.11). For $\tau = 0$, the mean interspike interval is equal to the noise-induced period, $\langle T \rangle \approx 14.5 ns$, (see Fig 4.8). As the time delay increases, $\langle T \rangle$ drops to the value of $11 ns$ which corresponds to the period induced by the delay (see Fig. 5.10). By further increase of τ , $\langle T \rangle$ rises a little above $12 ns$. Then, for $\tau = 11 ns$ the mean interspike interval decreases again and the same scenario is repeated with a modulation period very close to the delay-induced period.

There is a resemblance to the piecewise linear dependence upon τ reported in

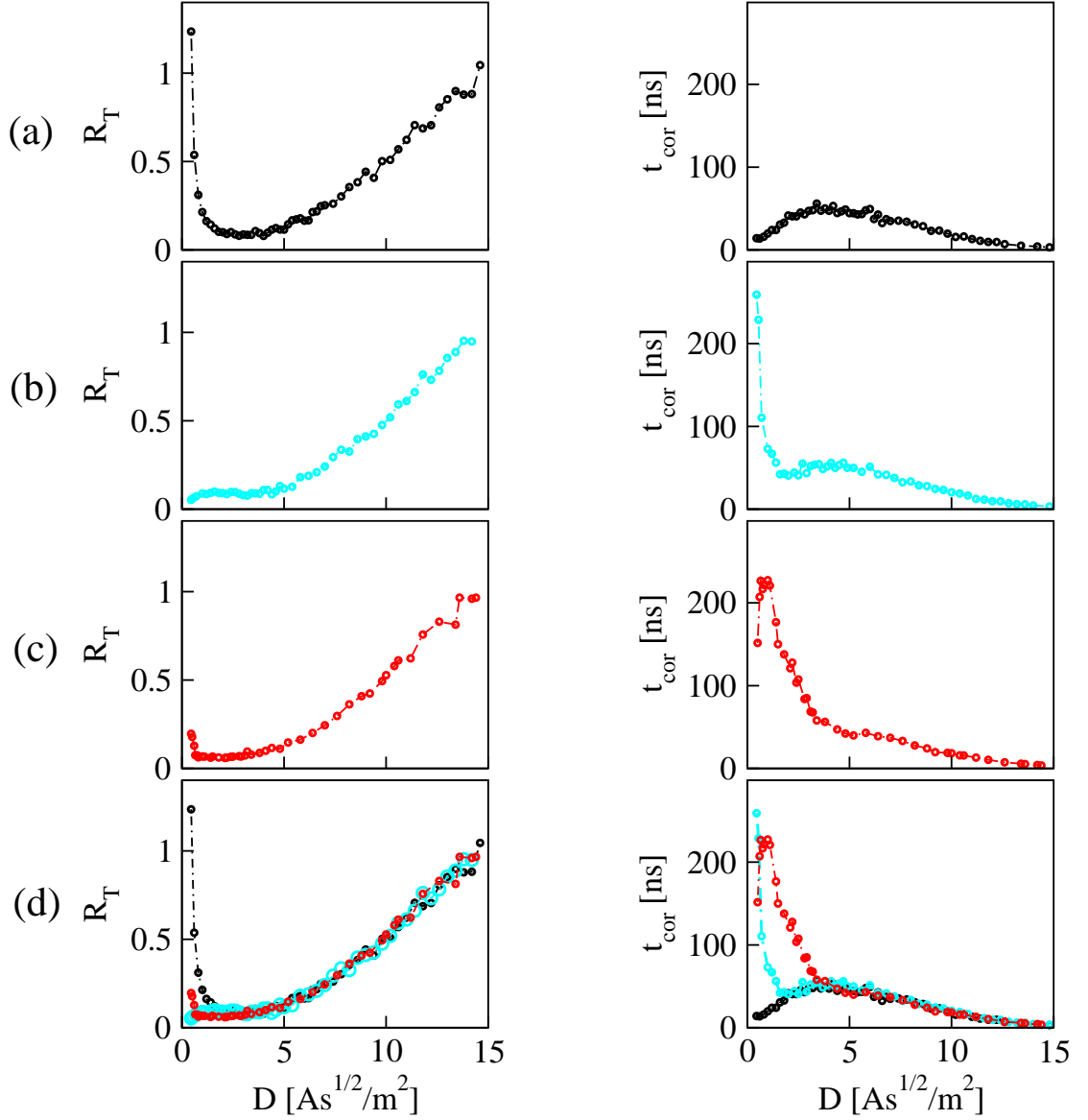


Figure 5.14: Correlation time (right) and normalized fluctuation of pulse durations (left) as a function of the noise intensity for (a) $K = 0$, (b) $(K, \tau) = (0.02V\text{mm}^2/A, 11\text{ns})$ and (c) $(K, \tau) = (0.02V\text{mm}^2/A, 14.5\text{ns})$. All three curves plotted together in (d). Averages over 30 time series realizations of length $T = 1600\text{ns}$ have been used for the calculation of t_{cor} and averages over 1000 periods for R_T . $U = 2.99V$ and $\sigma = 2.0821(\Omega m)^{-1}$. Parameters as in Table 2.1.

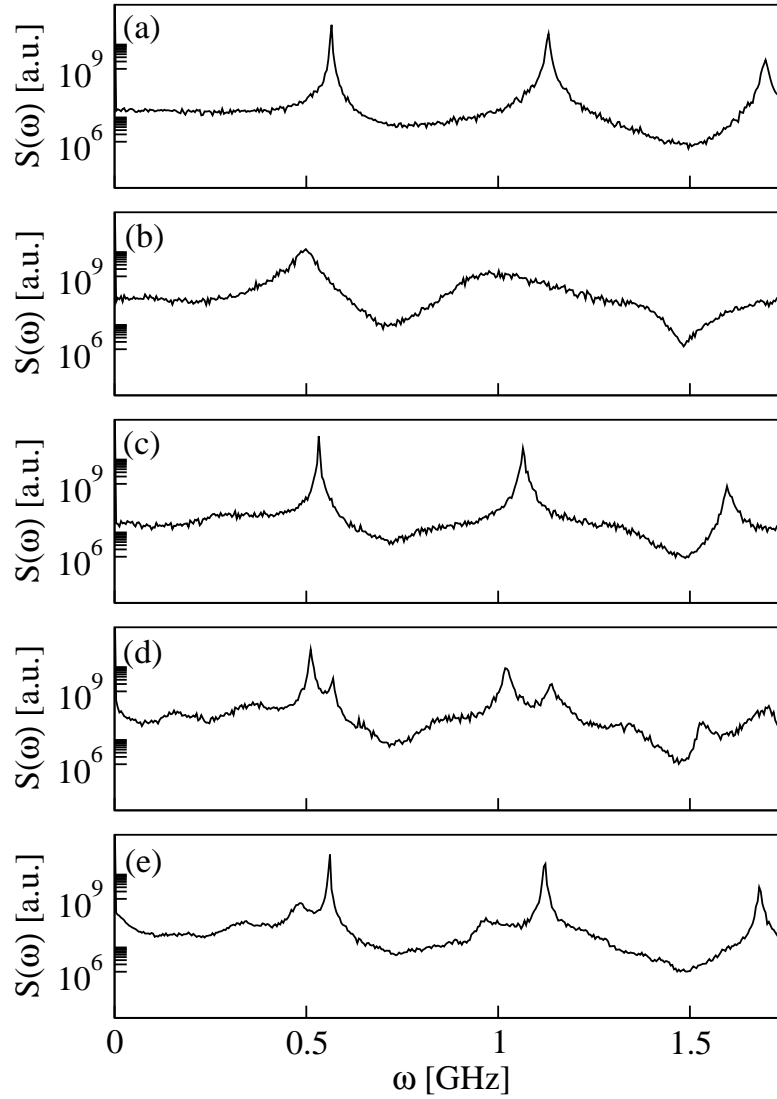


Figure 5.15: Fourier power spectral density of the total current density $J(t)$ for $D = 0.1As^{1/2}/m^2$, $K = 0.02Vmm^2/A$ and varying time delay: (a) $\tau = 3$ (b), $\tau = 12$, (c) $\tau = 21$, (d) $\tau = 35$ and (e) $\tau = 37.5ns$, respectively. Averages over 30 time series realizations of length $T = 1600ns$ have been used. $U = 2.99V$ and $\sigma = 2.0821(\Omega m)^{-1}$. Parameters as in Table 2.1.

other excitable systems below a Hopf bifurcation: The FitzHugh-Nagumo model in [Jan03, Bal04] and the Belousov-Zhabotinsky reaction (under correlated noise and nonlinear delayed feedback) in [Bal06] which, like our system, is also spatially extended. The difference to our analysis is that in those models the case of a delay-

induced limit cycle was either excluded or not discussed. The explanation for the entrainment of the time scales by the delayed feedback was done on the basis of a linear stability analysis. It was shown that the basic period is proportional to the inverse of the imaginary part of the eigenvalue of the fixed point which itself depends linearly on τ , for large time delays.

In our case, we have to additionally consider the time scale imposed by the delay which seems to compete, in a way, with the noise-induced period. At higher noise intensities, $D = 2.5As^{1/2}/m^2$, where the noise-induced period is almost equal to the delay-induced period, the modulation of the mean interspike interval upon the time delay is less strong, and the time scales oscillate around the value of $11ns$ (left plot of Fig. 5.13 (c)).

Finally, the power spectra may also provide information not only on the dependence on the time delay of the time scales, but also of the coherence. The result is shown in Fig 5.15. One can see that variation of τ shifts the basic frequency and affects the spectral widths, as well.

6 A generic model for excitability

It is very common to use simple models in order to understand the dynamics of more complicated ones like the superlattice. In this chapter we present a generic model undergoing a saddle-node bifurcation on a limit cycle. The advantages are that such a simple model is easier to handle numerically and is better in visualizing the dynamical behaviour. Moreover, it offers the possibility for analytical treatment under specific considerations [Aus07]. Bifurcations are governed by universal characteristics present in every system, however complicated, prepared in their vicinity.

6.1 Global bifurcations

In the previous chapters, we distinguished between two dynamical regimes, one in the vicinity of a *local* bifurcation, namely a supercritical Hopf bifurcation, and one in the vicinity of a saddle-node bifurcation on a limit cycle. The latter is a *global* bifurcation in the sense that it involves a large region of the phase space. The fact that it cannot be confined to a small neighbourhood of fixed points or periodic orbits, like in the case of local bifurcations, yields it harder to detect. In the following we provide a descriptive picture for such global bifurcations [Sch01] which play a central role in the dynamics studied in this work. For a mathematical description one should refer to textbooks [Guc86, Kuz95].

6.1.1 Saddle-node bifurcation on a limit cycle

This bifurcation is also known as saddle-node bifurcation on an invariant circle (*SNIC*), *blue-sky catastrophe* or saddle-node infinite period bifurcation (*SNIPER*), the latter of which is the term used throughout this work. As shown in Fig. 6.1, a saddle-point and a stable node lying on an invariant circle (any trajectory starting on this circle remains there) collide and give birth to a limit cycle. The period T of the born limit cycle obeys a characteristic square-root scaling law, $T \sim 1/\sqrt{\mu - \mu_c}$,

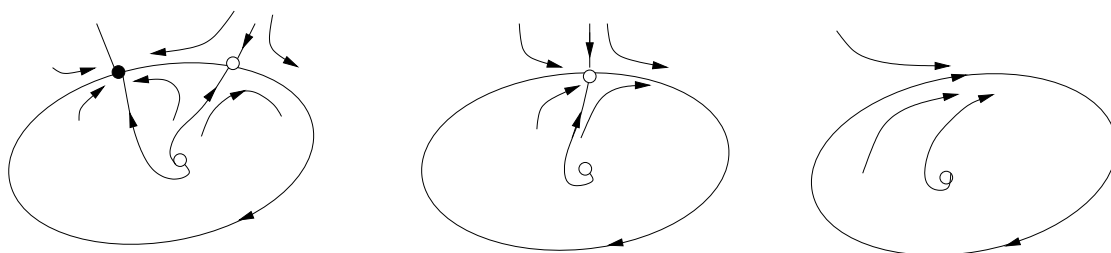


Figure 6.1: Saddle-node bifurcation on a limit cycle (*blue-sky catastrophe*, *SNIPER*). Open and full circles denote unstable, and stable fixed points, respectively. A saddle-node pair on the circle (left) move closer as the bifurcation is approached, saddle-point and node collide (middle) giving birth to a limit cycle (right).

where μ is the bifurcation parameter and μ_c its critical value. The amplitude, on the other hand, is finite at the birth of the limit cycle and remains almost constant. In the next section we will present a generic model undergoing a *SNIPER* and therefore study in more detail the dynamics associated to this bifurcation.

6.1.2 Homoclinic Bifurcation

This bifurcation is also known as *saddle-loop* bifurcation. Depicted in Fig. 6.2 (from right to left), a limit cycle moves closer and closer to a saddle-point, touches it and forms, thus, a homoclinic loop and disappears (left plot). Viewed in the other

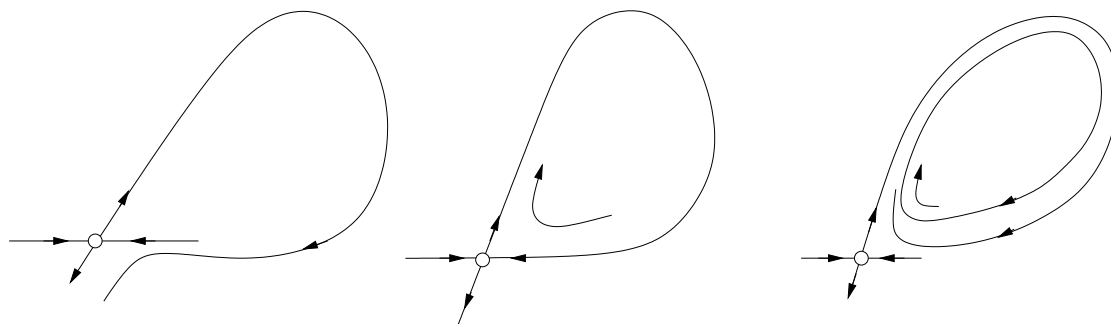


Figure 6.2: Homoclinic bifurcation on the plane. Right: Limit cycle approaching saddle-point, colliding in a homoclinic orbit (middle) and vanishing (left).

direction, a limit cycle is born from a homoclinic orbit. The orbit is “homoclinic” in the sense that it is a trajectory which joins the saddle-point to itself. (In the

SNIPER the periodic orbit appears from a homoclinic orbit to a saddle-node). This bifurcation is also an infinite period bifurcation in which the period of the born limit cycle obeys a logarithmic scaling law [Gas90, Kuz95]. The period T

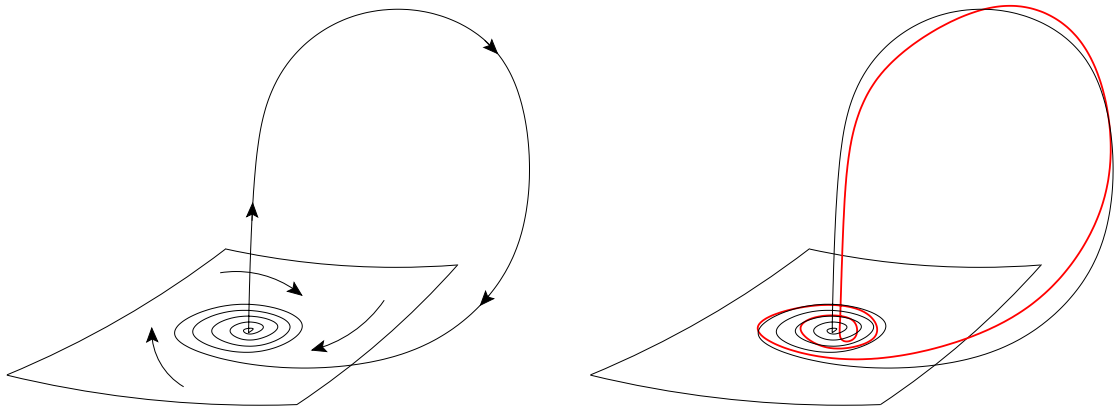


Figure 6.3: Left: Homoclinic orbit to a saddle-focus. The plane corresponds to the two-dimensional stable manifold of the saddle-focus. Right: A periodic orbit (red) close to the primary homoclinic orbit (black).

lengthens approximately like $T \sim \lambda_u^{-1} \ln|\mu - \mu_c|$, where λ_u is the real part of the least unstable eigenvalue of the saddle-point, μ is the bifurcation parameter and μ_c its critical value. Like in the case of the *SNIPER*, the amplitude of the born limit cycle is finite and constant. A three-dimensional phase space gives rise to a wider variety of homoclinic bifurcations, some of which may involve an infinite number of periodic orbits [Shi63, Shi65, Nei65]. The homoclinic orbit in \mathbb{R}^3 is either to a saddle-point (like in the two-dimensional case) or to a saddle-focus. A saddle-focus has a one-dimensional unstable manifold and a two-dimensional stable manifold. A homoclinic orbit to a saddle-focus is shown in Fig. 6.3. In the following chapter we will deal with a variety of complicated homoclinic orbits likely to be found in systems with delay which is responsible for the infinite dimensionality of such systems.

6.2 Other bifurcations of periodic orbits

Apart from the above global bifurcations, there are other ways limit cycles can be destroyed or created. Here we refer to two local bifurcations of limit cycles which we will come across in Chapter 7.

6.2.1 Saddle-node bifurcations of cycles

This bifurcation is also called *fold bifurcation of cycles*. By analogy with the fold bifurcation of a saddle-point and a node, here an unstable and a stable limit cycle coalesce and annihilate (Fig. 6.4). Each fixed point of the Poincaré section in this figure corresponds to a limit cycle.

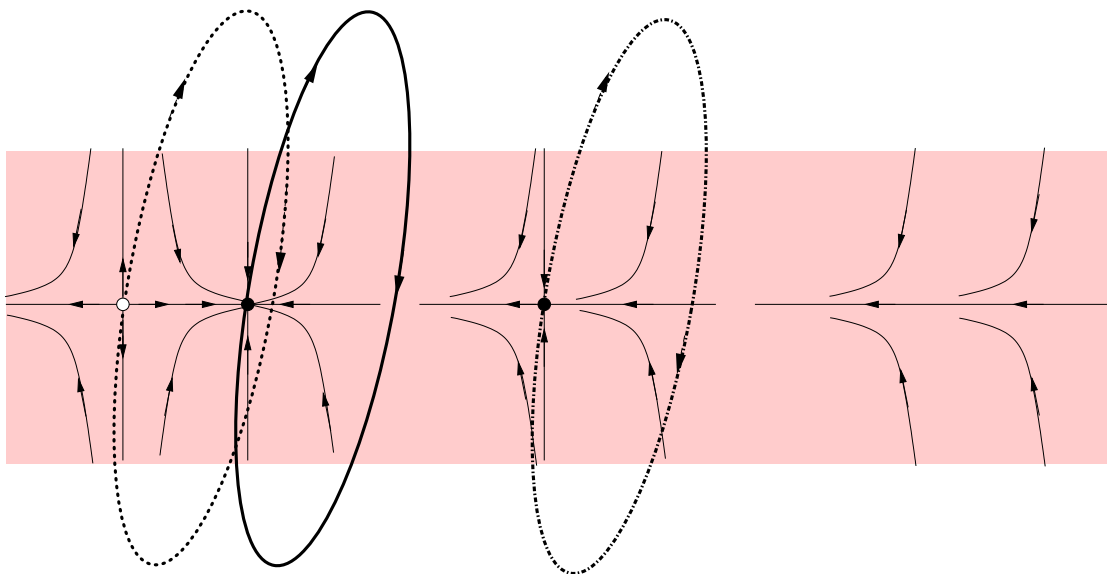


Figure 6.4: Saddle-node bifurcation of limit cycles. Left: Stable (thick line) and unstable (dotted line) periodic orbits collide (middle) and disappear (right). The coordinate plane in the light pink shaded area shows the Poincaré section (after [Kuz95]).

6.2.2 Period-doubling bifurcation of cycles

This bifurcation is also known as *flip bifurcation*. A limit cycle loses its stability, and another cycle, with a period twice the period of the original cycle, is born (Fig. 6.5). Other bifurcations involving periodic orbits are the Hopf bifurcation, Neimark-Sacker (or secondary Hopf bifurcation occurring in three-, or higher-, dimensional systems, and in which a limit cycle bifurcates into a quasiperiodic orbit; the resulting motion lies on a two-dimensional torus).

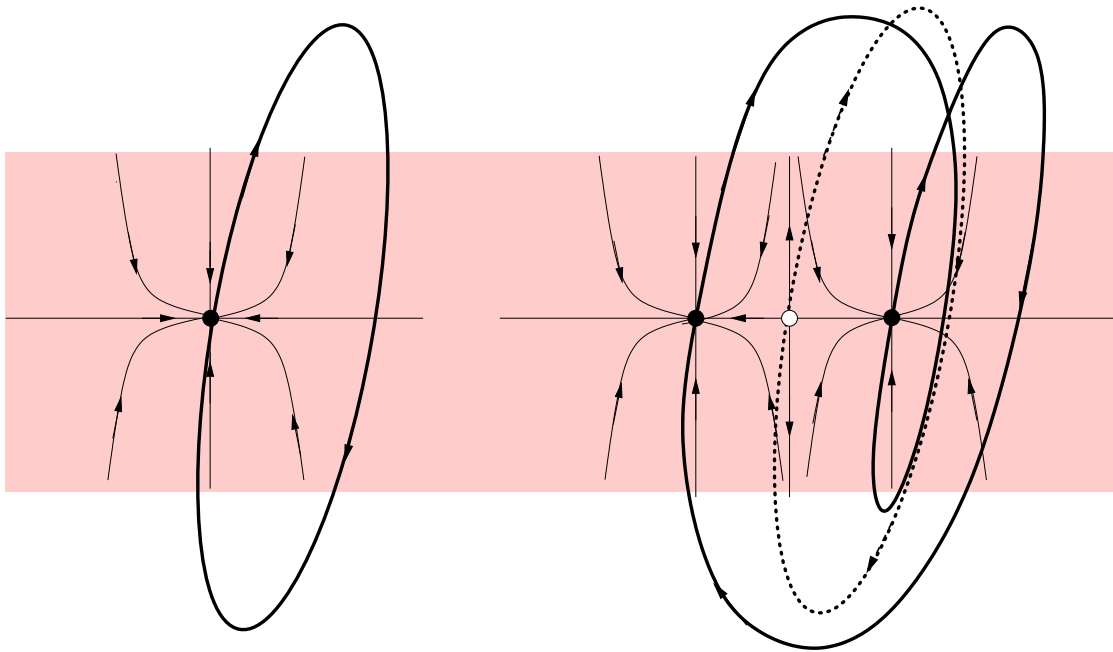


Figure 6.5: Flip bifurcation (period-doubling): A limit cycle (left) loses its stability (dotted cycle in right plot), and another cycle, with a period twice the period of the original cycle (solid cycle in right plot), is born. The coordinate plane in the light pink shaded area shows the Poincaré section (after [Kuz95]).

6.3 A paradigm for the *SNIPER*

We consider a generic model for a saddle-node bifurcation on a limit cycle. It is a system of two nonlinear ODEs as follows [Hu93a, Dit94, Rap94, Hiz07]:

$$\dot{x} = x(1 - x^2 - y^2) + y(x - b) \quad (6.1)$$

$$\dot{y} = y(1 - x^2 - y^2) - x(x - b). \quad (6.2)$$

Here x and y denote the system variables and b plays the role of the bifurcation parameter. In polar coordinates $x = r \cos \phi$, $y = r \sin \phi$, Eqs. (6.1) and (6.2) read:

$$\dot{r} = r(1 - r^2) \quad (6.3)$$

$$\dot{\phi} = b - r \cos \phi \quad (6.4)$$

In Fig. 6.6 the vector fields on the circle and the corresponding phase portraits of the polar coordinate ϕ are shown. When $b < 1$ (Fig. 6.6 (a)) there are three

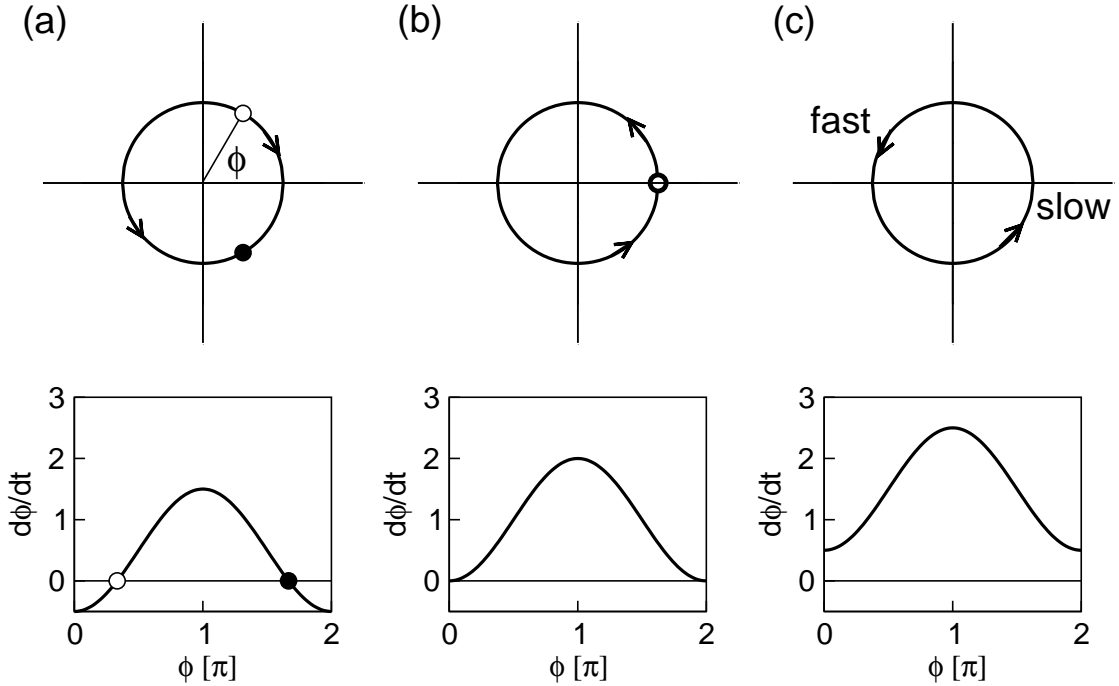


Figure 6.6: Top: *SNIPER* on the circle (a) below ($b = 0.5$), (b) at ($b = 1$) and (c) above ($b = 1.5$) the bifurcation. Full and open circles correspond to stable node and saddle-point, respectively. Bottom: Corresponding phase portraits of the polar coordinate ϕ .

fixed points: An unstable focus at the origin and a pair of a saddle-point and a stable node on the unit circle with coordinates $(b, +\sqrt{1-b^2})$ and $(b, -\sqrt{1-b^2})$, respectively. The latter collide at $b = 1$ (Fig. 6.6 (b)) and a limit cycle $r = 1$ is born (Fig. 6.6 (c)). Above, but close to the bifurcation, the period T of this limit cycle obeys a characteristic scaling law which can be calculated analytically: By setting $r = 1$ in Eqs. 6.1 and 6.2, we obtain that the time required for ϕ to change by 2π is:

$$T = \int dt = \int_0^{2\pi} \frac{d\phi}{b - \cos(\phi)}. \quad (6.5)$$

This integral can be evaluated by the substitution $u = \tan \phi$ [Bro05]. The result is:

$$T = \frac{2\pi}{\sqrt{b^2 - 1}}. \quad (6.6)$$

As $b \rightarrow 1^+$ we can do the approximation $\sqrt{b^2 - 1} = \sqrt{(b-1)(b+1)} \approx \sqrt{2}\sqrt{b-1}$. Then

$$T \approx \frac{\pi\sqrt{2}}{\sqrt{b-1}}. \quad (6.7)$$

Alternatively: For $b \rightarrow 1^+$ we are very close to the bifurcation where the fixed points collide at $\phi = 0$ and $\phi = \pi$. Therefore we can write $\phi = \pi + \phi'$ (or $\phi = 0 + \phi'$ equivalently), where ϕ' is very small, and do a Taylor expansion around ϕ :

$$\begin{aligned} \dot{\phi}' &= \dot{\phi} = b - \cos((\phi' + \pi)) \\ &= b - \cos(\phi') \\ &= b - 1 + \frac{1}{2}\phi'^2 + \dots \end{aligned} \quad (6.8)$$

If we let $\theta = \phi'/\sqrt{2}$ and $b' = b - 1$ the equation becomes:

$$\sqrt{2}\dot{\theta} = b' + \theta^2.$$

Separating variables yields:

$$T = \sqrt{2} \int_{-\infty}^{\infty} \frac{d\phi'}{b' + \phi'^2} = \frac{\pi\sqrt{2}}{\sqrt{b'}} = \frac{\pi\sqrt{2}}{\sqrt{b-1}}, \quad (6.9)$$

which is in agreement with Eq. (6.7). Therefore, the frequency $f = 1/T$ scales according to the square-root law $f \sim (b-1)^{1/2}$, shown in Fig. 6.8 (e).

In Fig. 6.7 the phase space of the system is shown below, at and above the bifurcation. Below the bifurcation (Fig. 6.7(a)) a saddle-point and a stable node exist on the circle $r = 1$, which forms an invariant manifold. The red trajectory starts left of the stable manifold of the saddle-point and thus performs an excursion in phase space along the unstable manifold of the saddle-point before ending in the stable node. The black trajectory starts right of the unstable manifold of the saddle-point and is directly attracted to the stable node. The turquoise line starts in the vicinity of the focus. The motion on the circle once the limit cycle is born is nonuniform. This is stressed in the upper-right plot in Fig. 6.6 where the fast and slow parts of this motion are shown. The two time scales characterizing the oscillation are also to be seen in the time series of the x -variable in Fig. 6.8 (a). The system slows down when it passes through the point $((x, y) = (1, 0))$ where the collision took place. The fixed point disappears but what remains is a “ghost” of the saddle-node which is responsible for this slow passage. The closer to the *SNIPER* the system is, the longer it takes to pass through the “ghost”. Once it manages to escape this “barrier”, it performs an excursion in phase space which corresponds to the fast motion on the unit circle.

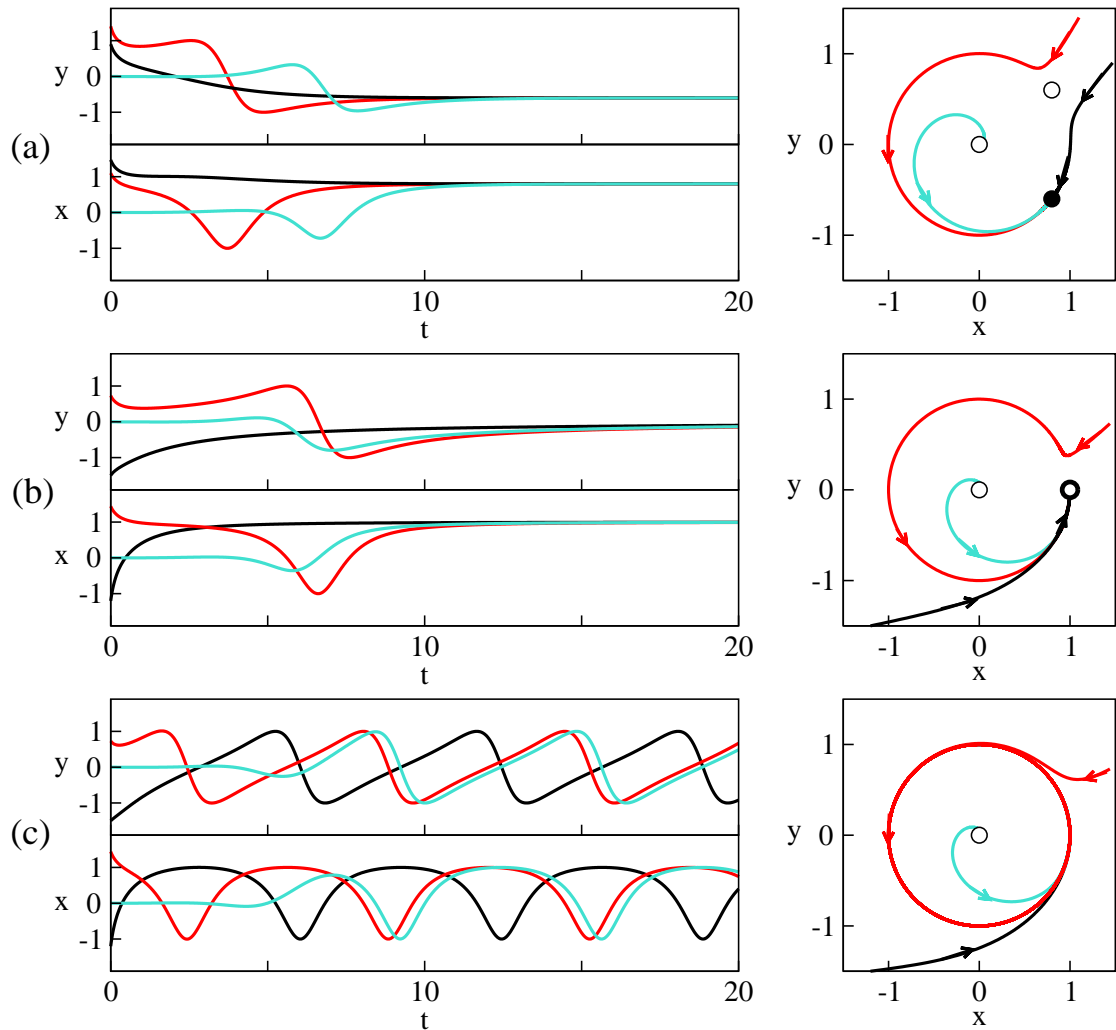


Figure 6.7: *SNIPER* bifurcation which system of Eqs. 6.1 and 6.2 undergoes. Right: Phase portrait (a) below ($b = 0.8$), (b) at ($b = 1$) and (c) above the bifurcation ($b = 1.4$). Open circle at the origin denotes unstable focus. Open circle in (a) denotes the saddle-point whereas full circle denotes the stable node. In (b) open circle with thick line denotes semistable fixed point, where saddle-point and stable node collide for $b = 1$. Red, black and cyan coloured trajectory correspond to initial condition chosen near the saddle-point, stable node, and unstable focus, respectively. Left: Corresponding time-series of y and x variable.

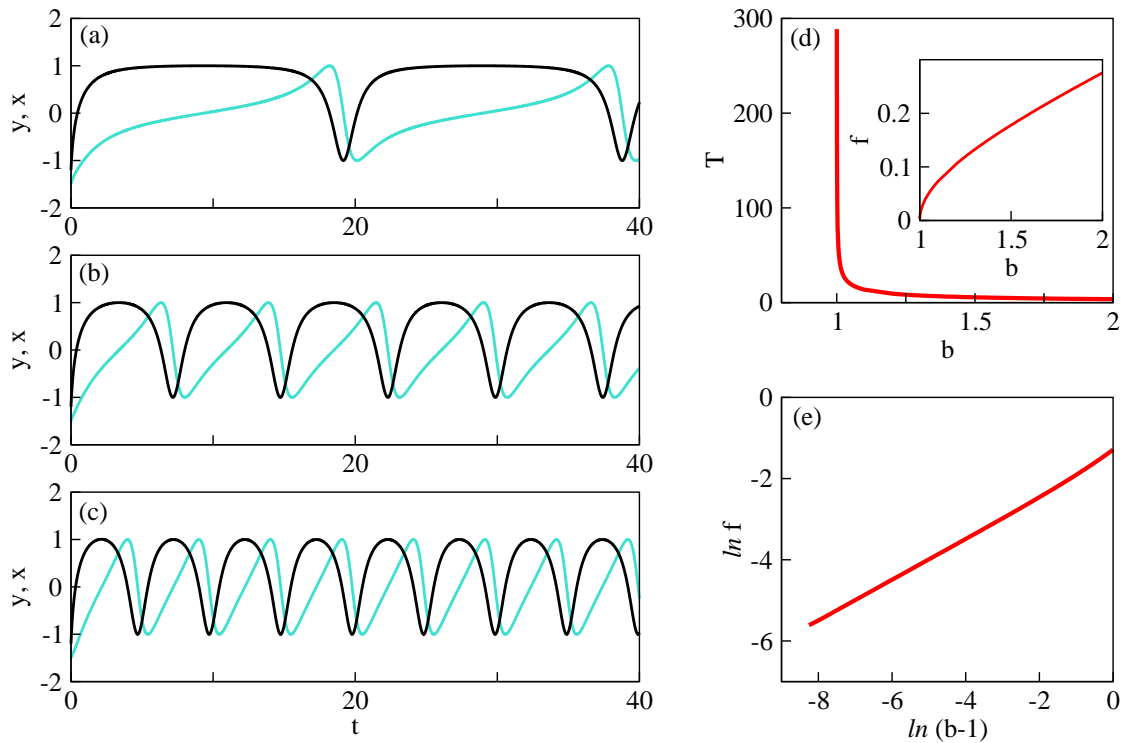


Figure 6.8: Left: Time series of the generic model above the *SNIPER*: (a) $b = 1.05$, (b) $b = 1.3$ and (c) $b = 1.6$. (d) Period T as a function of b . Inset shows the same for frequency $f = 1/T$. Frequency scaling law demonstrated in (e).

6.3.1 Excitability and the influence of noise

As discussed above, the saddle-node point affects the dynamics of the system even when it has disappeared. In a one-variable system at a saddle-node bifurcation, $\dot{x} = \mu + x^2$ (known as the normal form of the saddle-node bifurcation), the saddle-node point represents an impenetrable barrier at $\mu = 0$. Trajectories starting on the attracting manifold of the saddle-node slowly approach the saddle-node but never escape beyond it. In our system the unit circle, in a way, allows to overcome this barrier and a limit cycle is born. This can be understood considering Eq. (6.3) and Eq. (6.4) for $b \geq 1$ as $r = 1$ and $\dot{\phi} = -dV/d\phi$, respectively, where $V(\phi) = -b\phi + \sin \phi$ is a periodic “potential” function that describes the motion on the unit circle.

The barrier-role of the saddle-node exactly at the bifurcation yields the system sensitive to noise. Almost 20 years ago [Sig89] a “saddle-node bifurcation leading to relaxation oscillations” was studied considering a special case of the Adler

equation [Adl73], which is well known in the study of phase-locked oscillators: $\dot{\psi} = -B \sin(\psi) + \Delta\omega_0$ where ψ is the oscillator phase, $\Delta\omega_0$ is the difference between the oscillator frequency and the frequency of the external signal (frequency detuning between two oscillators) and B is a constant. Now the model in [Sig89], $\dot{\theta} = 1 - \cos\theta$, has a saddle-node point at $\theta = 0$ (θ is a phase) and provides a good model for the dynamics of the center manifold that becomes a limit cycle above the bifurcation in a system at a *SNIPER* and actually, according to Eq. (6.4), describes the dynamics of our model on $r = 1$ and for $b = 1$. The authors in [Sig89] showed that Gaussian white noise can push the system across the barrier and induce oscillations which resemble those observed in the deterministic system above the bifurcation. The system is, thus, excitable and therefore served as a toy-model to introduce the phenomenon of coherence resonance [Hu93a, Dit94, Rap94].

One should also add that the saddle-node bifurcation on a limit cycle is associated with the, so-called, type I neuronal excitability [Rin89]. Neurons are excitable in their nonlinear response to electrical stimuli. The transition from quiescent to periodic firing is characterized by the behaviour of the firing frequency. Neurons are divided into type I and type II dynamics according to this behaviour [Hod48]. Type II neurons exhibit a finite nonzero frequency as periodic firing begins and are associated with Hopf bifurcations. Type I neurons are described by Morris-Lecar [Mor81] and Hindmarsh-Rose models [Hin82] and type II neurons by FitzHugh-Nagumo models [Fit61, Nag62]. All these models are simplified variants of the much more complicated Hodgkin-Huxley model [Hod48]. The FitzHugh-Nagumo and Hindmarsh-Rose models, in particular, are described by a system of two ordinary differential equations:

$$\begin{aligned}\dot{x} &= f(x, y) \\ \dot{y} &= g(x, y),\end{aligned}$$

where x is the cell membrane potential and y is a recovery variable. The FitzHugh-Nagumo takes the following form:

$$\dot{x} = c \left(x - \frac{x^3}{3} - y \right) \tag{6.10}$$

$$\dot{y} = \frac{1}{c} (x - by + a). \tag{6.11}$$

It is characterized by the linearity of g whereas in the case of the Hindmarsh-Rose,

g includes a quadratic dependence on x :

$$\dot{x} = c \left(x - \frac{x^3}{3} - y \right) \quad (6.12)$$

$$\dot{y} = \frac{1}{c} (x^2 + dx - by + a) . \quad (6.13)$$

In the above equations a , b , c and d are system parameters. In Fig. 6.9 the nullclines $f(x, y) = 0$ (black) and $g(x, y) = 0$ (magenta) of both models are plotted. In the case of the FitzHugh-Nagumo model (left plot of Fig. 6.9), for given parameters, there exists a stable fixed point marked by the intersection of the two nullclines. Shifting the straight nullcline ($x = a$) to the right, the fixed point becomes unstable and a limit cycle is born through a Hopf bifurcation at $a = 1$. In the Hindmarsh-Rose model (right plot of Fig. 6.9) the nullcline $g(x, y) = 0$ is a parabola and intersects the nullcline $f(x, y) = 0$ at three points, a stable, an unstable and a saddle-point. Shifting the parabola downwards (by tuning a), the saddle-point and the stable fixed point disappear through a saddle-node bifurcation and a limit cycle is born (*SNIPER*).

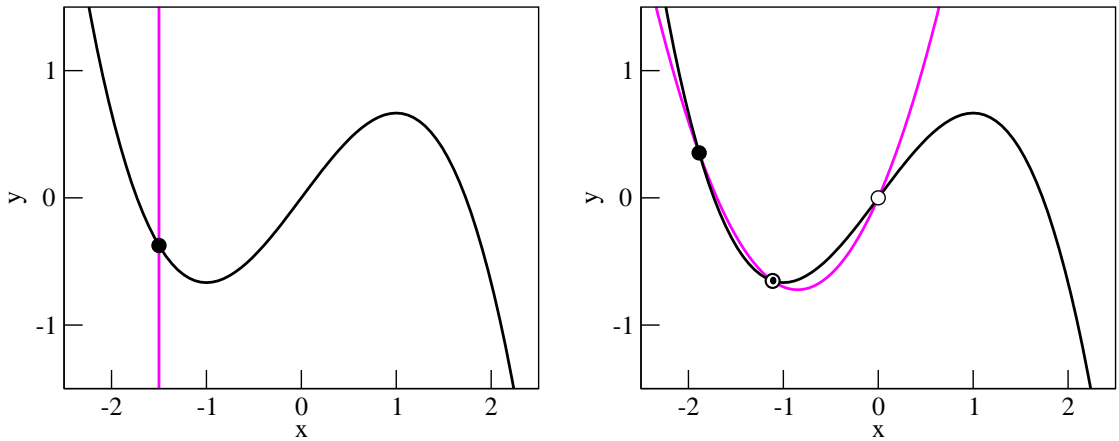


Figure 6.9: Left: Nullclines of FitzHugh-Nagumo model according to Eqs. (6.10), (6.11) with $a = 1.5$ and $b = 0$. Full circle denotes stable fixed point. Right: Nullclines of Hindmarsh-Rose model according to Eqs. (6.12), (6.13) with $a = 0$, $b = 1$ and $d = 0.7$. Full circle denotes stable fixed point, double circle denotes saddle-point and open circle denotes unstable fixed point.

The above analysis motivates why we should study the generic model presented in this chapter. Since it is prototype for type I neuronal excitability it may find applications in the field of neuroscience.

6.3.2 Connection to the superlattice

In the superlattice, which is the focal point of this work, the *SNIPER* was first reported in a slightly different model in [Pat98]. The effect of noise is qualitatively the same as that on the generic model and basically is demonstrated through coherence resonance [Hiz06]. The next step is to study to what extent time-delayed feedback generates similar dynamics to both complicated (superlattice) and simple (generic) system. We have already shown how delay acts on the superlattice below the *SNIPER*. In the next chapter we will be able to interpret these results by investigating the generic model with delay.

7 Delay-induced multistability in the generic model

In Chapter 5, time-delayed feedback was applied in order to control various features of the noise-induced dynamics observed in the superlattice in two different dynamical regimes, below the Hopf bifurcation and below the *SNIPER*. Whereas control of noise-induced oscillations below a Hopf bifurcation has been extensively studied, ([Jan03] and further references in Chapter 5), less has been done for the case of a global bifurcation and in particular for the saddle-node bifurcation on a limit cycle. In both cases, the idea is to prepare the system in a stable fixed point, turn on Gaussian white noise inducing, thus, stochastic oscillations and then try to control features such as coherence and time scales by appropriately tuning the two control parameters, the time delay and the control amplitude. Time-delayed feedback, however, is itself able to *create* additional dynamics which are then simply smeared-out by noise.

Already in Chapter 5, we saw that delay may induce bifurcations in a certain regime of the parameter space. The tracking of delay-induced bifurcations is a reasonable thing to do before switching noise on. Below the Hopf bifurcation a great deal of work on delay-induced dynamics has been carried out not only for simple systems but for spatially extended systems as well [Ste05a]. In the case of a global bifurcation, the role of delay is less known. In Chapter 5 we presented the effect of delay in the superlattice below the *SNIPER*. In order to understand those findings and the underlying mechanisms better, in the following we use the prototype model for such a bifurcation (introduced in Chapter 6) and examine the effect of time-delayed feedback [Hiz07].

7.1 The delay equations

We extend the model of the previous chapter by incorporating time-delayed feedback according to the Pyragas [Pyr92] scheme. The equations are the following:

$$\dot{x} = x(1 - x^2 - y^2) + y(x - b) - K(x - x_\tau) \quad (7.1)$$

$$\dot{y} = y(1 - x^2 - y^2) - x(x - b) - K(y - y_\tau). \quad (7.2)$$

Here x_τ and y_τ are the delayed variables at time $t - \tau$, with τ and K being the time delay and control strength, respectively. This kind of control is called *diagonal* because the control force may be written in the form of a unity matrix.

7.1.1 Linear stability analysis

We prepare the system slightly below the bifurcation ($b = 0.95$) and switch on the control ($K \neq 0$). The first question that arises concerns the stability of the three fixed points and how this changes, or not, due to delay. For this, we perform a standard linear stability analysis and derive the characteristic equation for the roots, Λ , which determine the stability of the fixed points. The linearized system can be written as:

$$\frac{d}{dt}\mathbf{X}(\mathbf{t}) = A\mathbf{X}(\mathbf{t}) + B\mathbf{X}(\mathbf{t} - \tau), \quad \mathbf{X}(\mathbf{t}) = \begin{pmatrix} x(t) \\ y(t) \end{pmatrix}, \quad (7.3)$$

with

$$A = \begin{pmatrix} 1 - 3x^{*2} - y^{*2} + y^* - K & -2x^*y^* + x - b \\ -2x^*y^* - 2x^* + b & 1 - x^{*2} - 3y^{*2} - K \end{pmatrix} \quad (7.4)$$

$$B = \begin{pmatrix} K & 0 \\ 0 & K \end{pmatrix}, \quad (7.5)$$

where x^* and y^* are the coordinates of the fixed point under consideration. With the ansatz $\delta x(t) = \delta y(t) = e^{\Lambda t}$ it holds that $\delta x(t - \tau) = \delta y(t - \tau) = e^{\Lambda t} e^{-\Lambda \tau}$. The characteristic equation is then given by solving the equation:

$$\Delta(\Lambda) = \det(A + e^{-\Lambda \tau} B - \Lambda \mathbf{I}) = 0. \quad (7.6)$$

For the unstable focus $(x^*, y^*) = (0, 0)$, the characteristic equations is as follows :

$$(1 - K + Ke^{-\Lambda \tau} - \Lambda)^2 + b^2 = 0. \quad (7.7)$$

Due to the presence of the delay, Eq. (7.7) has infinitely many solutions. However, the stability of the fixed points is determined by a finite number of critical roots with largest real parts. Using the Lambert function W , which is defined as the inverse function of $g(z) = ze^z$ for complex z [Hal71, Cor96, Ama05], the solution of Eq. (7.7) can be expressed as:

$$\Lambda = \frac{1}{\tau} W[K\tau e^{\tau(K-1\pm b)}] - K + 1 \mp ib. \quad (7.8)$$

In the case of the saddle-point $(x^*, y^*) = (b, +\sqrt{1-b^2})$ and the stable node $(x^*, y^*) = (b, -\sqrt{1-b^2})$, the characteristic equation is as follows:

$$\begin{aligned} 0 &= \Lambda_{s,n}^2 - 2K\Lambda_{s,n}e^{-\Lambda_{s,n}\tau} + 2\Lambda_{s,n}K \mp \Lambda_{s,n}\sqrt{1-b^2} + 2\Lambda_{s,n} \\ &\quad - 2K^2e^{-\Lambda_{s,n}\tau} + K^2e^{-2\Lambda_{s,n}\tau} + K^2 \pm \sqrt{1-b^2}Ke^{-\Lambda_{s,n}\tau} \\ &\quad - 2Ke^{-2\Lambda_{s,n}\tau} \mp \sqrt{1-b^2}K + 2K - 2\sqrt{1-b^2} \\ 0 &= (\Lambda_{s,n} + K)^2 \mp \sqrt{1-b^2}(\Lambda_{s,n} + K) + 2(\Lambda_{s,n} + K) \mp 2\sqrt{1-b^2} \\ &\quad + e^{-\Lambda_{s,n}\tau} \left[-K(\Lambda_{s,n} + K \mp \sqrt{1-b^2}) - K(\Lambda_{s,n} + 2 + K) \right] + K^2e^{-2\Lambda_{s,n}\tau} \\ 0 &= (\Lambda_{s,n} + K + 2) \left(\Lambda_{s,n} + K \mp \sqrt{1-b^2} \right) \\ &\quad - Ke^{-\Lambda_{s,n}\tau} \left(\Lambda_{s,n} + K \mp \sqrt{1-b^2} \right) - Ke^{-\Lambda_{s,n}\tau} (\Lambda_{s,n} + K + 2) + K^2e^{-2\Lambda_{s,n}\tau}. \end{aligned}$$

The subscripts “s” and “n” denote the saddle-point (upper sign) and the node (lower sign), respectively. Equation (7.9) can be factorized into two equations:

$$\Lambda + K + 2 - Ke^{-\Lambda\tau} = 0 \quad (7.9)$$

$$\Lambda_{s,n} + K \mp \sqrt{1-b^2} - Ke^{-\Lambda_{s,n}\tau} = 0, \quad (7.10)$$

with solutions:

$$\Lambda^1 = \frac{1}{\tau} W[K\tau e^{\tau(2+K)}] - 2 - K \quad (7.11)$$

$$\Lambda_{s,n}^2 = \frac{1}{\tau} W[K\tau e^{\tau(K \mp \sqrt{1-b^2})}] - K \pm \sqrt{1-b^2}. \quad (7.12)$$

Figure 7.1 shows the real parts of the eigenvalues Λ as a function of τ for a fixed value of K for all three fixed points. One may see the eigenvalues of the uncontrolled system at $\tau = 0$, and their interaction with the delay-induced modes

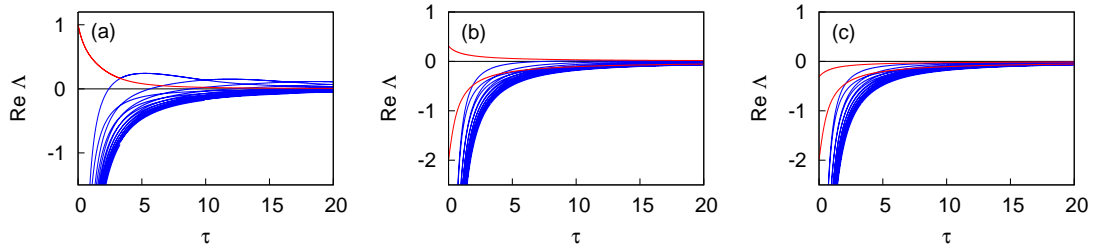


Figure 7.1: Real parts of the complex eigenvalues Λ as a function of τ , for fixed $K = 1$ and $b = 0.95$. For the (a) unstable focus, (b) the saddle-point and (c) the stable node. The modes emerging from the uncontrolled system and the delay-induced modes are marked red and blue, respectively.

(blue) with increasing τ . In all three cases, control is unable to change the stability of the fixed point: In the case of the unstable focus, the mode with the largest real part (red) tends to very small values with increasing delay, remaining however positive. The same holds for the unstable mode of the saddle-point. Symmetric behaviour is observed for the stable modes of both saddle-point and node: They tend to zero as a function of τ but remain negative. The picture does not change qualitatively even for other values of K and therefore one might conclude that delay induces no change in the stability of the fixed points.

7.2 Global bifurcation analysis

However, the above local analysis gives no information on the global changes in phase space that delay potentially induces. A numerical investigation shows, in fact, that there exists bistability in a certain parameter regime in the K - τ plane: Trajectories starting close to the saddle-point are attracted by a delay-induced limit cycle, whereas trajectories starting elsewhere end up in the stable node.

7.2.1 Delay-induced homoclinic bifurcation

Keeping $\tau = 3$ fixed we find the critical value K_c of K for which this delay-induced limit cycle is born and observe a scaling $T \sim \ln|K - K_c|$ in the period T of the corresponding oscillations, typical for the case of a homoclinic bifurcation (see Chapter 6). In Fig. 7.2 phase portraits of the system below, at and above the bifurcation are shown. Trajectories with different initial conditions are shown: One starting from the vicinity of the unstable focus in the origin (blue) and one from the vicinity of the saddle-point (red). Bistability is revealed in Fig. 7.2(c)

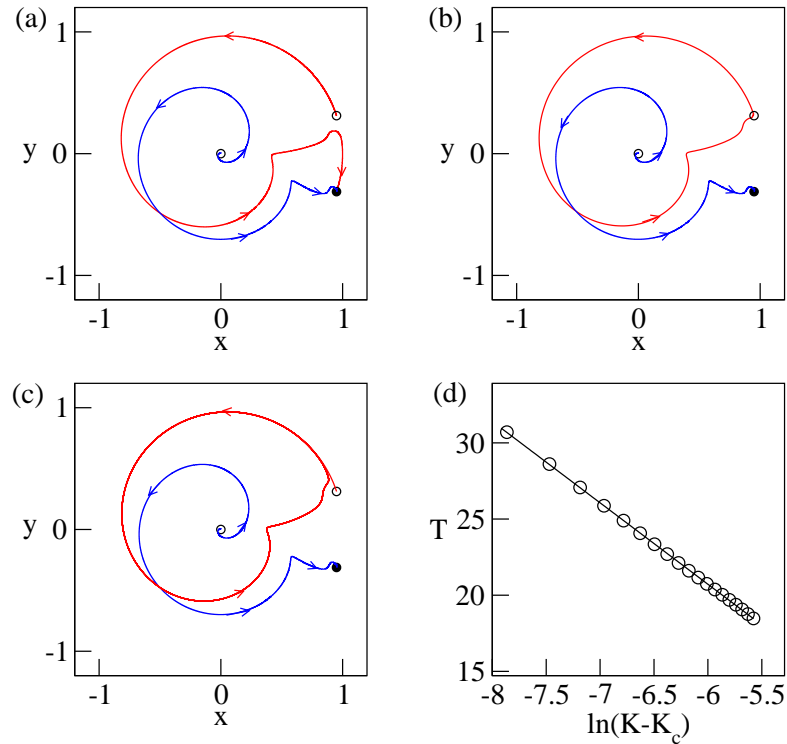


Figure 7.2: (a) Two dimensional projection of the phase space below the homoclinic bifurcation ($K = 0.335$). (b) Homoclinic orbit (red) achieved at $K_c = 0.3401$. (c) Delay-induced limit cycle (red) above the homoclinic bifurcation ($K = 0.3438$). (d) Scaling of the oscillation period T above but close to the critical point K_c (crosses: simulation data, solid line: linear fit). Full and open circles mark stable and unstable fixed points, respectively. Parameters: $b = 0.95$, $\tau = 3$.

where two attractors (the stable node and the delay-induced limit cycle) coexist. The “kink” in the trajectory shortly before the loop closes is due to the control: The control force starts acting at $t = 3$ when the system is still moving on the slow part of the unit circle. Therefore, its effect is not so noticeable. As the system moves faster the control force attains higher values and the trajectory starts deviating from its deterministic path at $t = 13$. This deviation becomes large at $t = 18$ where the trajectory, shortly before settling in the stable node, appears to be “attracted” to the saddle-point, resulting in this “kink” in the x - y projection. Also, as K approaches the critical value, the trajectory passes closer and closer to the saddle-point on its way to the stable node. This ends in a homoclinic orbit at $K = K_c$, (Fig. 7.2(b)) from which a periodic orbit is generated (Fig. 7.2(c)). The period of the born limit cycle scales according to $T \approx (\text{Re}\Lambda_u)^{-1} \ln|K - K_c|$, where Λ_u is the

least unstable eigenvalue of the saddle-point (i. e. the one closest to the imaginary axis). One may calculate this from Eq. (7.11) and find $\Lambda_u^{-1} = 0.1739^{-1} = 5.75$. This is in rather good agreement with the slope of the solid line in Fig. 7.2(d) which equals 5.35. An analogous mechanism was also found in the case of the superlattice (Chapter 5).

Next we use a bifurcation continuation tool, DDE-BIFTOOL [Eng02, Eng01], and follow the homoclinic bifurcation in the K - τ plane. The produced bifurcation curve can be seen in Fig. 7.3 (left). It consists of two main curves: One running through points A - E and a second tongue-like curve. In the white area the system

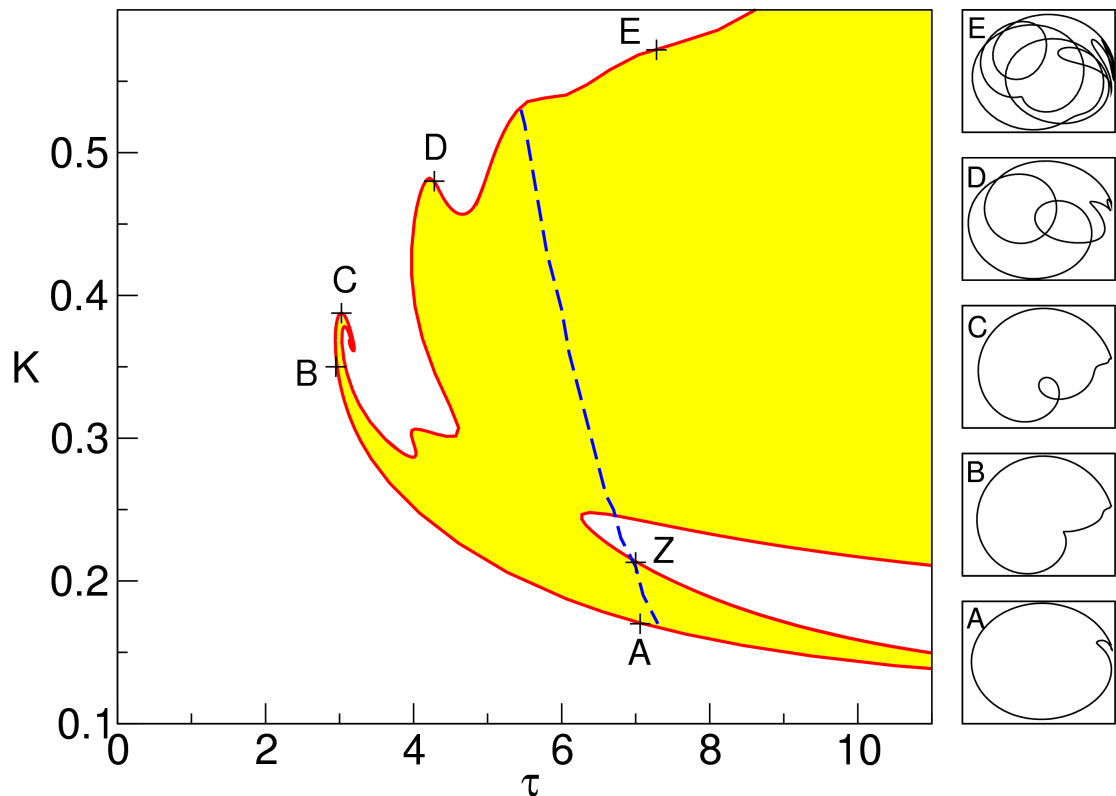


Figure 7.3: Curve of homoclinic bifurcations (red) in the K - τ plane (left). A - E label various points with homoclinic orbits, which are shown in the x - y phase plane in the panel on the right. Delay-induced limit cycles exist, in addition to the stable fixed point, in the yellow area. The blue dashed curve separates the regions $\sigma_0 < 0$ (left) and $\sigma_0 > 0$ (right)

is monostable (stable fixed point) while in the yellow area a delay-induced periodic attractor is born via a homoclinic bifurcation marked by the red curves.

7.2.2 The role of the saddle quantity

At this point one should emphasize the role of the saddle-point: Due to the delay, the saddle-point possesses no longer two distinct eigenvalues (one positive, i.e. unstable, and one negative, i.e. stable) but infinitely many. Moreover, complex eigenvalues come into play as well. The eigenvalues, however, that determine the behaviour of the colliding homoclinic orbit, are the leading ones, i.e. those closest to the imaginary axis. In Fig. 7.4 one can see the eigenvalue spectrum for two

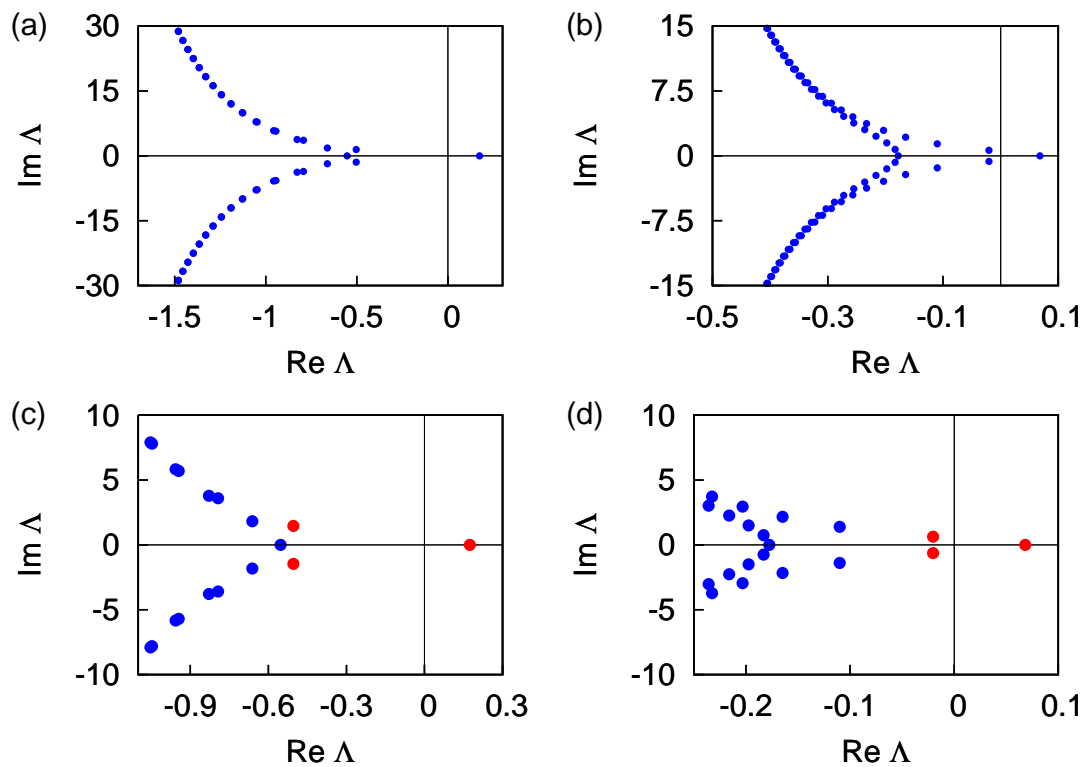


Figure 7.4: Spectra of the eigenvalues Λ of the saddle-point for two points on the homoclinic bifurcation line: (a) $K = 0.3401, \tau = 3$ (B in Fig. 7.3) and (b) $K = 0.57, \tau = 7.28$ (E in Fig. 7.3). (c) and (d) show the leading eigenvalues (red) of the spectra of (a) and (b) respectively. The saddle quantity $\sigma_0 = \text{Re}(\Lambda_s) + \text{Re}(\Lambda_u)$ is negative in (c) whereas in (d) it is positive. ($b = 0.8$)

points on the homoclinic bifurcation curve and notice that the leading eigenvalues of the saddle-point (red) are a positive real eigenvalue, as in the original uncontrolled system, and a complex conjugate pair with negative real parts, generated by the delay. This means that the saddle-point may turn into a *saddle-focus* for

certain values of K and τ . In Fig. 7.5 a schematic figure illustrates the three types of saddle-foci. Homoclinic orbits attached to a saddle-focus corresponding

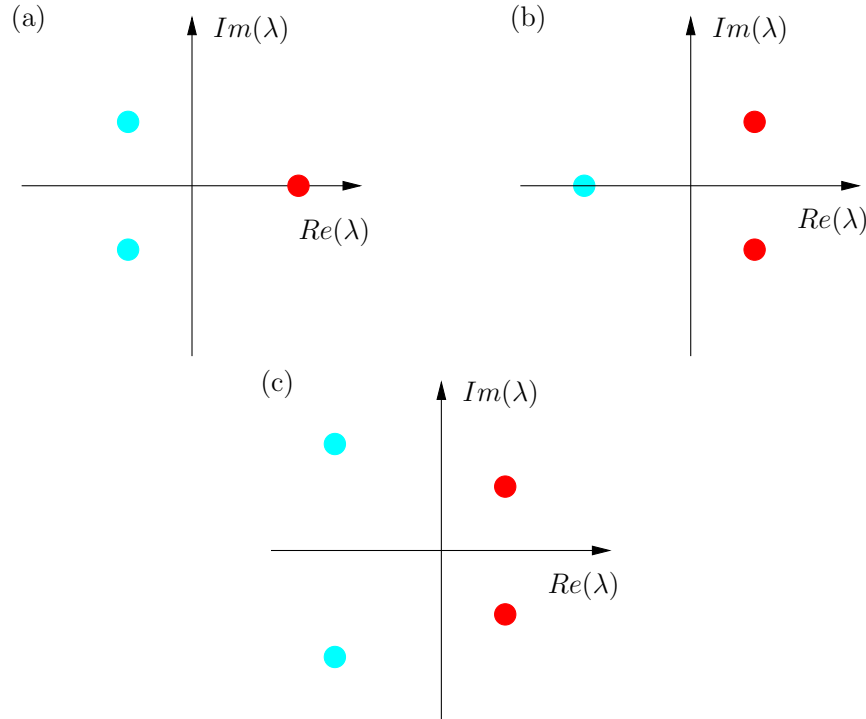


Figure 7.5: Saddle-foci are characterized by their leading characteristic eigenvalues. (a) Leading stable eigenvalues are complex conjugate, (b) leading unstable eigenvalues are complex conjugate and (c) both stable and unstable leading eigenvalues are complex conjugate (bi-focus).

to Fig. 7.5(a) approach the fixed point in an oscillating manner. This explains the phase portraits in Fig. 7.3 (right) which become more and more complicated as K increases.

From the above, it is clear that the two basic ingredients responsible for the delay-induced dynamics in our system, are the homoclinic orbits and the saddle-foci. The theory of homoclinic bifurcations for ordinary differential equations has been well developed [Kuz95, Guc86, Wig88]. As already mentioned, global bifurcations are strongly related to excitability and therefore one expects to encounter them in excitable systems. Various physical systems such as modulation-doped semiconductor heterostructures [Doe92], semiconductor lasers [Wie02, Kra03a], neuron models [Feu00] and chemical systems [Bor06] have been studied in this respect, both theoretically and experimentally. On the other hand, less work has been carried out for systems with delay undergoing such nonlocal bifurcations [Set06].

It is therefore appropriate to analyze a generic system like the one studied here which, despite its simplicity, exhibits rich delay-induced dynamics with a homoclinic bifurcation as key component.

7.3 Delay-induced multistability

In what follows we will apply the theorems on homoclinic orbits connecting to saddle-foci as developed by Shilnikov [Kuz95]. According to them, the so-called saddle quantity is crucial for the homoclinic bifurcations occurring in high-dimensional systems. The saddle quantity is defined as $\sigma_0 = \text{Re}(\Lambda_s) + \text{Re}(\Lambda_u)$, where Λ_s and Λ_u are the leading stable and unstable eigenvalues, respectively. Shilnikov proved, among other, that negative σ_0 results in the birth of a unique stable limit cycle from a homoclinic orbit. On the other hand, for $\sigma_0 > 0$, a wide variety of homoclinic bifurcations may occur, some of which involve infinitely many periodic orbits in the vicinity of the homoclinic orbit. The blue dashed curve in Fig. 7.3 shows the condition $\sigma_0 = 0$. Along the homoclinic bifurcation line in Fig. 7.3 the saddle quantity changes sign, thereby allowing for both scenarios to take place. Figure 7.4 shows the eigenvalue spectra for two different points (B and E) on the bifurcation line corresponding to negative and positive saddle quantities, respectively.

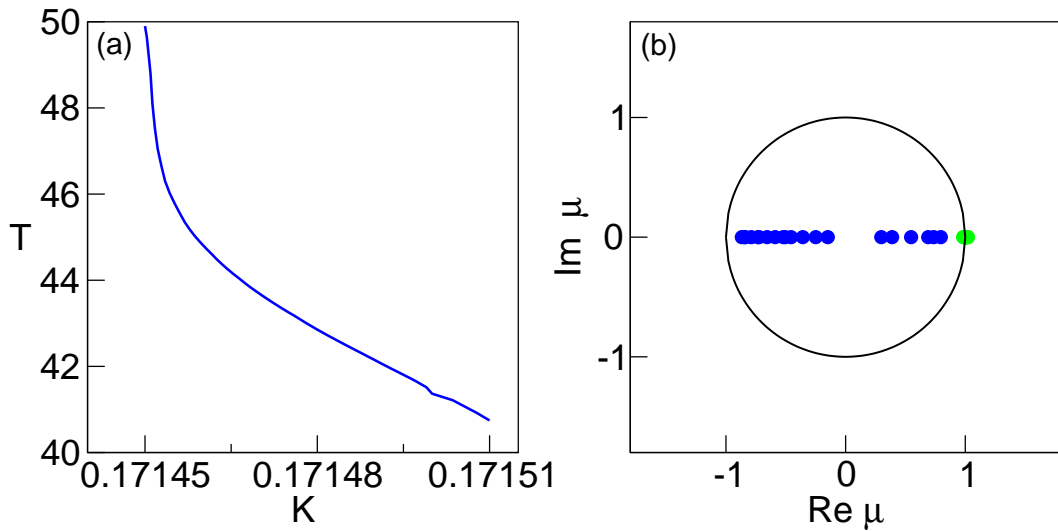


Figure 7.6: (a) Period T of limit cycle born in a homoclinic bifurcation at $(K, \tau) = (0.17145, 7)$ (point A in Fig. 7.3, $\sigma_0 < 0$). (b) The two leading Floquet multipliers of the periodic orbit $\mu_1 = 1$ (green) and μ_2 (blue) with T as a parameter, in the complex plane. $b = 0.95$.

7.3.1 Negative saddle quantity $\sigma_0 < 0$

For $\tau = 7$, a homoclinic bifurcation takes place at $K = 0.17145$ (point A in Fig. 7.3). In this case $\sigma_0 = -0.0116$, and the bifurcation creates one stable limit cycle, with Floquet multipliers within the unit circle (Fig. 7.6(b)). The period T of this limit cycle increases monotonically as the bifurcation point is approached (Fig. 7.6(a)), according to Shilnikov's theory.

7.3.2 Positive saddle-quantity $\sigma_0 > 0$

Moving further along $\tau = 7$ other homoclinic bifurcation curves are crossed, e.g. at $K = 0.213$ (Fig. 7.7(b), cf. point Z in Fig. 7.3). There, the saddle quantity

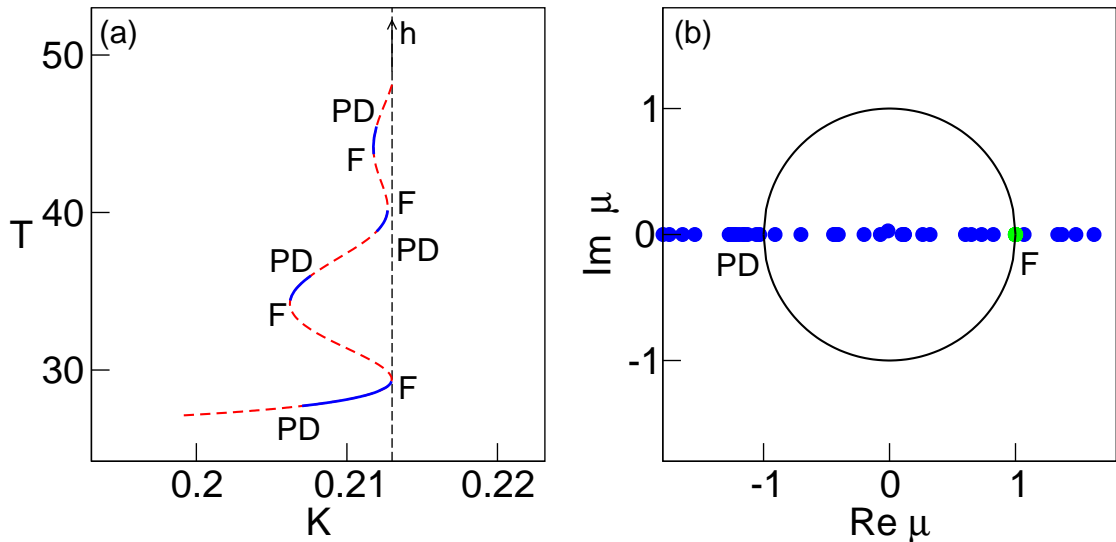


Figure 7.7: (a) Period T of limit cycle born in a homoclinic bifurcation at $(K, \tau) = (0.213, 7)$ point Z in Fig. 7.3, $\sigma_0 > 0$), undergoing infinitely many fold (F) and period-doubling (PD) bifurcations, before ending in a homoclinic orbit h for $T \rightarrow \infty$ at $K = 0.213$. Solid blue and dashed red lines denote stable and unstable limit cycles, respectively. (b) The two leading Floquet multipliers of the periodic orbit $\mu_1 = 1$ (green) and μ_2 (blue) with T as a parameter, in the complex plane. $b = 0.95$.

is positive ($\sigma_0 = 0.0023$, calculated analytically from Eq. (7.12)), and the picture is much more complicated: An infinite number of bifurcations take place, which are related to saddle-node (fold) bifurcations of pairs of stable and unstable limit cycles, and additional period-doubling (flip) bifurcations of the stable limit cycles. The dependence of the period T of the limit cycles upon K is a nonmonotonic

multivalued function, whose turning points are associated with saddle-node bifurcations. The solid blue lines correspond to stable periodic solutions which coexist for a fixed value of K .

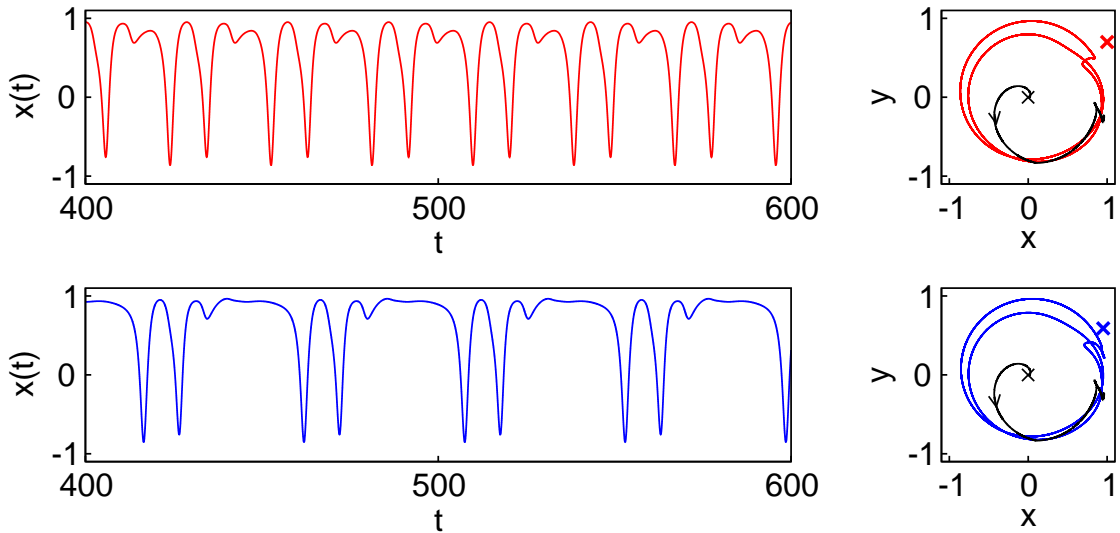


Figure 7.8: Right: Two coexisting periodic attractors corresponding to two different stable branches of Fig. 7.7(a). Crosses mark initial conditions: $(x, y) = (1, 0.7)$, $(x, y) = (0.95, 0.59)$ and $(x, y) = (-0.001, -0.001)$ for red, blue and black trajectory, respectively. Left: Time series of x variable of the corresponding limit cycles. Periods are $T = 28.63$ and $T = 45.56$ for red and blue limit cycle, respectively. $K = 0.212$ and $\tau = 7$.

In Fig. 7.8 an example of two such coexisting orbits for $K = 0.212$ is shown. In addition to the black trajectory, which asymptotically approaches the stable fixed point, there exist two periodic orbits with different period T (red and blue) which can be reached by choosing two different initial conditions. In between the fold bifurcations of the stable limit cycles, pairs of forward and inverse period doubling bifurcations occur. In Fig. 7.7(b) the trivial Floquet multiplier $\mu_1 = 1$ and the leading Floquet multiplier μ_2 of the periodic orbit are plotted. It can be seen how μ_2 changes as T is varied along the multivalued function in the main figure, showing how fold and flip bifurcations occur, at $\mu_1 = 1$ and $\mu_1 = -1$, respectively. One should also expect other bifurcations near the critical point due to secondary homoclinic orbits.

7.4 Summary and comparison to the superlattice

We have presented a mechanism for delay-induced multistability in a system near a global bifurcation. In addition to the fixed point attractor which the uncontrolled system already possesses, a time-delayed feedback in the form of Pyragas difference control induces one or more coexisting limit cycle attractors. Depending upon the feedback control strength K and the delay time τ , either a single stable limit cycle is born in a homoclinic global bifurcation, or an infinite number of (stable and unstable) periodic orbits is induced undergoing a rich menagerie of bifurcation scenarios including period doubling and fold bifurcations. We have shown that the key ingredient in the observed dynamics is a homoclinic orbit connected to a saddle-focus created by delay. A bifurcation continuation in the K - τ plane was performed. Moreover, we were able to verify Shilnikov's theory of homoclinic bifurcations in a certain parameter regime. The excitable nature of the system and the infinite-dimensional phase space, due to delay, appear to play a crucial role in the induced homoclinicity. The results partly find application to the superlattice

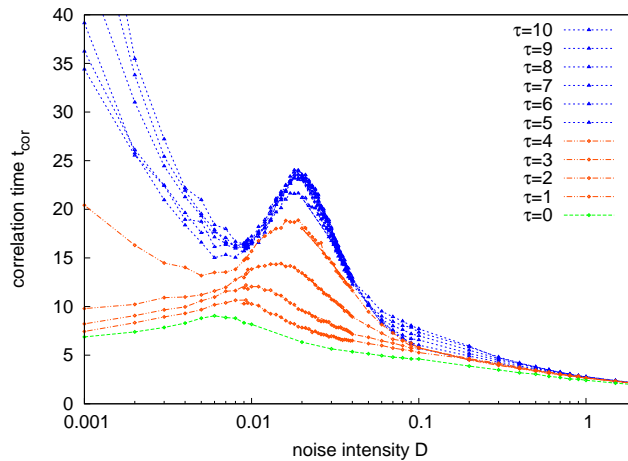


Figure 7.9: Correlation time in dependence on the noise intensity for increasing time delay in the controlled generic model. $b = 0.95$ and $K = 0.25$. Green corresponds to the free system, red corresponds to the regime where no delay-induced oscillations occur and blue corresponds to the regime where delay induces oscillations. (After [Aus07]).

model where, as shown in Chapter 5, a delay-induced homoclinic bifurcation is reported in agreement to the generic model studied in this chapter. In Chapter 5, moreover, the interaction of control with noise was also discussed. One can refer to [Aus07] for comparison to the findings for the generic model, which we briefly summarize here. As in the case of the superlattice, the effect of noise inside and

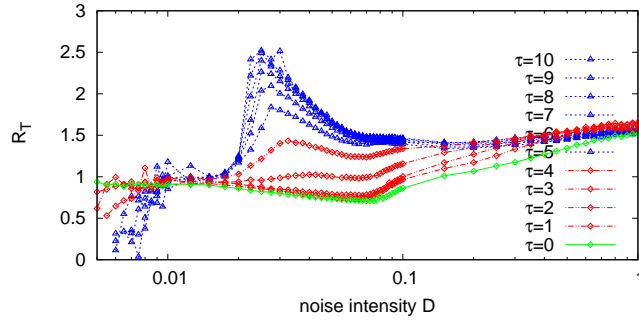


Figure 7.10: Normalized fluctuation of pulse durations in dependence on the noise intensity for increasing time delay in the controlled generic model. Parameters and colour coding as in Fig. 7.9. (After [Aus07]).

outside the regime of the delay-induced oscillations, was studied. It was found that outside this regime the coherence resonance is enhanced, exhibiting however a maximum at higher values of the noise-intensity. For parameters chosen inside the delay-induced oscillations regime, coherence resonance is enhanced due to the delay-induced regularity, like in the case of the superlattice (see Figs. 7.9 and 7.10). The dependence, however, of the time scales and coherence upon the time delay τ does not exhibit an oscillatory behaviour (see Fig. 7.11). This may have to do with the fact that the selected range of τ was too small and therefore this point requires further investigation.

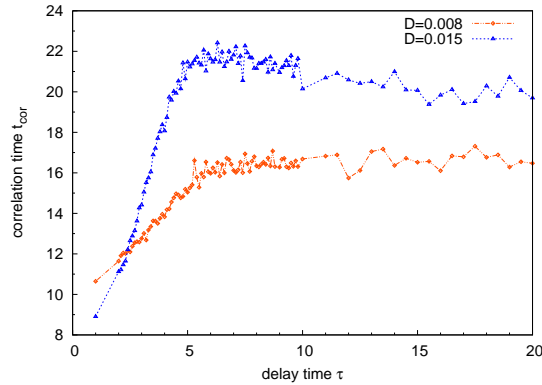


Figure 7.11: Correlation time in dependence on the time delay for two different values of the noise intensity D in the controlled generic model. Non-optimal $D = 0.008$ (red line) and optimal $D = 0.015$ (blue line). $b = 0.95$ and $K = 0.25$. (After [Aus07]).

8 Conclusions and outlook

The deterministic bifurcation scenarios governing the transition from stationary to moving electron charge density fronts and field domains in semiconductor superlattices have been studied. The bifurcation analysis was done in terms of two bifurcation parameters, the applied voltage which gives rise to a global constraint and the conductivity of the emitting contact. It was found that for low conductivities a supercritical Hopf bifurcation is responsible for the transition from stationary to oscillatory current densities, the amplitude of which scales with the characteristic square-root scaling law. In the spatio-temporal picture these oscillations are associated with weak front motion around the deterministic stable fixed point.

For higher conductivities the transition from stationarity to front motion was found to be related to a global bifurcation, namely a saddle-node bifurcation on a limit cycle (*SNIPER*). In this case, front motion through the whole device was observed and the period of the associated current oscillations exhibited an inverse square-root scaling law and tended to infinity while the amplitude was constant and finite at the birth of the limit cycle. By following the saddle-node bifurcation line in the bifurcation parameter plane we obtained a saw-tooth formed line of alternating “tongues” corresponding to limit cycle oscillations and a stable fixed point, respectively. In the vicinity of this bifurcation the system is excitable.

Considering the system under the influence of noise in both dynamical regimes, we found that noise induces current oscillations of increasing amplitude below the Hopf bifurcation. We quantified characteristics of these oscillations such as coherence and time scales. The regularity decreases with increasing noise level in terms of various measures, namely correlation times and Fourier power spectral density widths. The time scales, on the other hand, are hardly affected yielding the deterministic Hopf frequency robust against noise. Below the *SNIPER*, noise manages to induce front motion through the entire device. The existence of two time scales in the noisy front motion reflects the underlying deterministic bifurcation and is strongly connected to excitability. The latter is responsible for coherence resonance, i. e. there is an optimal noise level at which the motion is most regular. The period of the noise-induced current oscillations depends strongly upon the noise level, exhibiting a monotonic decrease for increasing noise.

By applying a time-delayed feedback global scheme of the voltage to the system, the effect of control in both dynamical regimes was studied. First, in the absence of noise, delay-induced bifurcations were tracked in the control parameter space. In the first regime there is a delay-induced Hopf bifurcation. In the presence of noise, the influence of control upon the coherence and the time scales in dependence of the time delay and the noise intensity was studied. It was found that the coherence by variation of the noise level is enhanced due to control. Moreover, it was shown that for a fixed control strength, the correlation time and the basic period of the noise-induced motion is modulated by variation of the time delay. Below the *SNIPER*, control induces another global bifurcation, namely a homoclinic bifurcation. Scanning a wide range of time delay values, we found an oscillatory dependence of the coherence and the time scales on the delay. Furthermore, for various combinations of the control parameters both enhancement and destruction of the coherence resonance effect in dependence on the noise intensity was found.

By introducing a generic model for the *SNIPER* we made direct comparisons to the noise- and delay-induced dynamics observed in the superlattice. Control induced here, as well, a homoclinic bifurcation which we were able to follow in the control parameter plane, obtaining an interesting bifurcation line. Along this line the homoclinic orbits exhibited increasing complexity which is related to the associated saddle-foci to whom they are connected. We were able to verify Shilnikov's theorems on homoclinic bifurcations for high-dimensional systems. By numerical and analytical estimation of the saddle-quantity, we were able to determine and demonstrate the two homoclinic bifurcation scenarios.

An interesting extension of this work would be the experimental verification of the *SNIPER* in the superlattice, where the emerging of moving fronts could be achieved by fixing the conductivity within an allowed range and by tuning the external voltage as more easily accessible parameter. Once the parameters are fixed below the *SNIPER*, noise can be added to the emitter in order to show the noise-induced front motion as well. We expect to see the same effects as reported theoretically in this work. Although here noise was added to each well locally, as explained in Chapter 3, the boundary determines the observed dynamics anyway.

Moreover, a more sophisticated bifurcation analysis of the superlattice could be carried out both with and without delay, using a bifurcation continuation numerical tool. A linear stability analysis would also be useful to calculate eigenvalues and in particular the saddle-quantity, which in the case of the delay-induced homoclinic orbit plays a crucial role.

In addition, the control of the noise-induced dynamics in both superlattice and generic model should be accurately compared, considering different choices for the values of the control parameters as well. Thus, having compared an abstract to a

physical model, one can obtain a fuller view of the dynamics with delay and noise, below a global bifurcation. Finally, in the spirit of [Pra07], an analytical theory of time-delayed feedback control of excitable systems could be developed.

Acknowledgments

First of all I would like to thank my supervisor Prof. Ekehard Schöll for giving me the opportunity to do my Ph. D. thesis in his group. His guidance, working method and support have been valuable over the years.

I would like to thank Dr. Andreas Amann for offering me insight into the superlattice model and always being willing to discuss and help with scientific problems.

I am grateful to Dr. Alexander Balanov for a fruitful and very pleasant collaboration during his various visits at our group.

Many thanks go to all former and current members of the AG Schöll for a very creative working environment. It has been a pleasure.

Finally, I would like to thank Prof. Harald Engel for doing the second assessment of my thesis.

This work was supported by the DFG in the framework of Sfb 555.

List of Figures

2.1	Sketch of the energy band structure in the superlattice	6
2.2	Homogeneous current-field characteristic	8
3.1	Spatio-temporal pattern of the electron density and the electric field and corresponding current density time series in the superlattice . .	15
3.2	Comparison of boundary characteristics with homogeneous current- field characteristic	16
3.3	Bifurcation diagram in the (σ, U) plane	17
3.4	Spatio-temporal electron density plots near the Hopf bifurcation . .	18
3.5	Times series and phase portraits above the Hopf bifurcation	19
3.6	Square-root scaling law of the amplitude above the Hopf bifurcation	20
3.7	Times series and spatio-temporal plots in the vicinity of the <i>SNIPER</i>	21
3.8	Spatio-temporal plots of the electric field in the vicinity of the <i>SNIPER</i>	22
3.9	Scaling law of the period above the <i>SNIPER</i> in the superlattice . .	23
3.10	Dynamics below the <i>SNIPER</i> in the superlattice	24
3.11	Bifurcation diagram in the (σ, U) plane with <i>SNIPER</i> line separat- ing stationary fronts from moving fronts regime	25
3.12	Electron density profiles and spatio-temporal plots showing the shift in the position of the stationary accumulation fronts by variation of the voltage	26
4.1	Noise induced oscillations and corresponding spatio-temporal pat- terns below the Hopf bifurcation in the superlattice	31
4.2	Autocorrelation function and Fourier power spectral density with Lorentzian fit for one noise realization	33
4.3	Correlation time versus the noise intensity below the Hopf bifurcation	34

4.4	Spectral properties of the noise-induced oscillations below the Hopf bifurcation in dependence on the noise intensity	35
4.5	Fourier power spectral density of the noise-induced current density oscillations below the Hopf bifurcation and corresponding Lorentzian fits for various noise intensities	36
4.6	Noise-induced front motion below the <i>SNIPER</i>	38
4.7	Noise-induced oscillations below the <i>SNIPER</i>	40
4.8	Normalized variance of the interspike interval, mean interspike interval and frequency of the noise-induced oscillations below the <i>SNIPER</i> in dependence on the noise intensity	41
4.9	Correlation time and coherence factor versus the noise intensity	42
4.10	Fourier power spectral density of the noise-induced current density oscillations below the <i>SNIPER</i> bifurcation	43
5.1	Global time-delayed feedback control scheme in the superlattice	49
5.2	Delay-induced Hopf bifurcation in the control parameter plane	50
5.3	Correlation time in dependence on the time delay for three values of the control strength	52
5.4	Fourier power spectral densities of the noisy total current density for various time delays below the Hopf bifurcation	53
5.5	Correlation time in dependence on the noise intensity in the controlled superlattice	54
5.6	Main period in dependence on the time delay for three different values of the control strength	55
5.7	Phase plots and electron density time series below the delay-induced homoclinic bifurcation	58
5.8	Blow-up of electron density phase portrait as the delay-induced homoclinic bifurcation is approached	59
5.9	Current density time series and spatio-temporal plots as delay-induced homoclinic bifurcation is approached	59
5.10	Period scaling of the delay-induced homoclinic bifurcation with the control strength as bifurcation parameter	60
5.11	Bifurcation diagram in the control parameter plane below the <i>SNIPER</i>	61
5.12	Period and period scaling law of the delay-induced limit cycle as a function of the time delay	62

5.13	Mean interspike interval and correlation time versus the time delay	63
5.14	Correlation time and normalized fluctuation of pulse durations as a function of the noise intensity of the controlled superlattice below the <i>SNIPER</i>	64
5.15	Fourier power spectral densities of the noisy total current density for various time delays below the <i>SNIPER</i>	65
6.1	Saddle-node bifurcation on a limit cycle	68
6.2	Homoclinic bifurcation	68
6.3	Homoclinic orbit to saddle-focus	69
6.4	Fold bifurcation of cycles	70
6.5	Period-doubling bifurcation of cycles	71
6.6	<i>SNIPER</i> on the circle in the generic model and phase portraits of the polar coordinate	72
6.7	Time series and phase portraits below and above the <i>SNIPER</i> in the generic model	74
6.8	Scaling law of frequency in the generic model for the <i>SNIPER</i>	75
6.9	Nullclines of the Fitzugh-Nagumo and the Hindmarsh-Rose model	77
7.1	Real parts of the complex eigenvalues of the delayed generic model as a function of the time delay	82
7.2	Phase portraits of the delay-induced homoclinic orbit in the generic model and corresponding period scaling law	83
7.3	Bifurcation diagram in the control parameter plane of the generic model	84
7.4	Spectra of the eigenvalues of the saddle-point for negative and positive saddle quantity	85
7.5	Schematic diagram of the saddle-foci	86
7.6	Period of delay-induced limit cycle in dependence of the control strength and corresponding two leading Floquet multipliers for negative saddle quantity	87
7.7	Delay-induced periodic solutions undergoing fold and flip bifurcations in dependence of the control strength and corresponding two leading Floquet multipliers for positive saddle quantity	88

7.8	Coexisting periodic orbits verifying multistability in the generic model with delay	89
7.9	Correlation time as a function of the noise intensity in the controlled generic model	90
7.10	Normalized fluctuation of pulse durations as a function of the noise intensity in the controlled generic model	91
7.11	Correlation time in dependence on the time delay in the controlled generic model	91

Bibliography

- [Adl73] R. Adler: *A study of locking phenomena in oscillators*. Proc. IEEE **61**, 1380 (1973).
- [Alo01] S. Alonso, I. Sendiña-Nadal, V. Pérez-Mañuzuri, J. M. Sancho, and F. Sagués: *Regular Wave Propagation Out of Noise in Chemical Active Media*. Phys. Rev. Lett. **87**, 078302 (2001).
- [Ama01] A. Amann, A. Wacker, L. L. Bonilla, and E. Schöll: *Dynamic scenarios of multi-stable switching in semiconductor superlattices*. Phys. Rev. E **63**, 066207 (2001).
- [Ama02] A. Amann, A. Wacker, and E. Schöll: *Tripole current oscillations in superlattices*. Physica B **314**, 404 (2002).
- [Ama02a] A. Amann, J. Schlesner, A. Wacker, and E. Schöll: *Chaotic front dynamics in semiconductor superlattices*. Phys. Rev. B **65**, 193313 (2002).
- [Ama03] A. Amann, K. Peters, U. Parlitz, A. Wacker, and E. Schöll: *Hybrid Model for Chaotic Front Dynamics: From Semiconductors to Water Tanks*. Phys. Rev. Lett. **91**, 066601 (2003).
- [Ama03a] A. Amann, J. Schlesner, A. Wacker, and E. Schöll: *Self-generated chaotic dynamics of field domains in superlattices*. In *Proc. 26th International Conference on the Physics of Semiconductors (ICPS-26), Edinburgh 2002*, edited by J. H. Davies and A. R. Long (2003).
- [Ama03c] A. Amann: *Nonlinear and chaotic front dynamics in semiconductor superlattices*. Ph.D. thesis, Technische Universität Berlin (2003).
- [Ama04] A. Amann and E. Schöll: *Bifurcations in a system of interacting fronts*. J. Stat. Phys. **119**, 1069 (2005).
- [Ama05a] A. Amann and E. Schöll: *Coupled lateral and vertical electron dynamics in semiconductor superlattices*. Phys. Rev. B **72**, 165319 (2005).

- [Ama05] A. Amann, E. Schöll, and W. Just: *Some basic remarks on eigenmode expansions of time-delay dynamics*. Physica A **373**, 191 (2007).
- [Ani99] V. S. Anishchenko, A. B. Neiman, F. Moss, and L. Schimansky-Geier: *Stochastic resonance: noise-enhanced order*. Phys. Usp. **42**, 7 (1999).
- [Aus07] R. Aust: *Multiple time-delayed feedback control of the coherence resonance in a model showing a global bifurcation*. Master's thesis, TU Berlin (2007).
- [Bab02] N. Baba, A. Amann, E. Schöll, and W. Just: *Giant improvement of time-delayed feedback control by spatio-temporal filtering*. Phys. Rev. Lett. **89**, 074101 (2002).
- [Bal04] A. G. Balanov, N. B. Janson, and E. Schöll: *Control of noise-induced oscillations by delayed feedback*. Physica D **199**, 1 (2004).
- [Bal05] A. G. Balanov, N. B. Janson, and E. Schöll: *Delayed feedback control of chaos: Bifurcation analysis*. Phys. Rev. E **71**, 016222 (2005).
- [Bal06] A. G. Balanov, V. Beato, N. B. Janson, H. Engel, and E. Schöll: *Delayed feedback control of noise-induced patterns in excitable media*. Phys. Rev. E **74**, 016214 (2006).
- [Bec02] O. Beck, A. Amann, E. Schöll, J. E. S. Socolar, and W. Just: *Comparison of time-delayed feedback schemes for spatio-temporal control of chaos in a reaction-diffusion system with global coupling*. Phys. Rev. E **66**, 016213 (2002).
- [Ben81] R. Benzi, A. Sutera, and A. Vulpiani: *The mechanism of stochastic resonance*. J. Phys. A **14**, L453 (1981).
- [Bla00] Y. M. Blanter and M. Büttiker: *Shot noise in mesoscopic conductors*. Phys. Rep. **336**, 1 (2000).
- [Bon00] L. L. Bonilla, G. Platero, and D. Sánchez: *Microscopic derivation of transport coefficients and boundary conditions in discrete drift-diffusion models of weakly coupled superlattices*. Phys. Rev. B **62**, 2786 (2000).
- [Bon02] L. L. Bonilla: *Theory of nonlinear charge transport, wave propagation, and self-oscillations in semiconductor superlattices*. J. Phys.: Condens. Matter **14**, R341 (2002).

- [Bon02a] L. L. Bonilla, O. Sánchez, and J. Soler: *Nonlinear stochastic discrete drift-diffusion theory of charge fluctuations and domain relocation times in semiconductor superlattices*. Phys. Rev. B **65**, 195308 (2002).
- [Bon04] L. L. Bonilla: *Theory of charge fluctuations and domain relocation times in semiconductor superlattices*. Physica D **199**, 105 (2004).
- [Bon05] L. L. Bonilla and H. T. Grahn: *Non-linear dynamics of semiconductor superlattices*. Rep. Prog. Phys. **68**, 577 (2005).
- [Bor06] G. Bordyugov and H. Engel: *Creating bound states in excitable media by means of nonlocal coupling*. Phys. Rev. E **74**, 016205 (2006).
- [Bro05] I. N. Bronstein, K. A. Semendjajew, G. Musiol, and H. Mühlig: *Taschenbuch der Mathematik* (Verlag Harri Deutsch, Frankfurt/Main, 2005), 6 edn.
- [Bul95] O. M. Bulashenko and L. L. Bonilla: *Chaos in resonant-tunneling superlattices*. Phys. Rev. B **52**, 7849 (1995).
- [Cad94] J. F. Cadiou, J. Guena, E. Penard, P. Legaud, C. Minot, J. F. Palmier, H. L. Person, and J. C. Harmand: *Direct optical injection locking of 20GHz superlattice oscillators*. Electronics Letters **30**, 1690 (1994).
- [Car88] C. E. Carr and M. Konishi: *Axonal delay lines for time measurement in the owl's brainstem*. Proc. Natl. Acad. Sci. USA **85**, 8311 (1988).
- [Chr95a] D. J. Christini and J. J. Collins: *Controlling nonchaotic neural noise using chaos control techniques*. Phys. Rev. Lett. **75**, 2782 (1995).
- [Cor96] R. M. Corless, G. H. Gonnet, D. E. G. Hare, D. J. Jeffrey, and D. E. Knuth: *On the Lambert W Function*. Adv. Comput. Math **5**, 329 (1996).
- [Dah07] T. Dahms, P. Hövel, and E. Schöll: *Control of unstable steady states by extended time-delayed feedback*. Phys. Rev. E **76**, 056201 (2007).
- [Dit94] T. Ditzinger, C. Z. Ning, and G. Hu: *Resonancelike responses of autonomous nonlinear systems to white noise*. Phys. Rev. E **50**, 3508 (1994).
- [Doe02] E. J. Doedel, R. C. Paffenroth, A. R. Champneys, T. F. Fairgrieve, Y. A. Kuznetsov, B. E. Oldeman, B. Sandstede, and X. Wang: *AUTO2000: Continuation and bifurcation software for ordinary differential equations (with HOMCONT)*. Concordia University, Montreal (2002).

- [Doe92] R. Döttling and E. Schöll: *Oscillatory bistability of real-space transfer in semiconductor heterostructures*. Phys. Rev. B **45**, 1935 (1992).
- [Dou93] J. K. Douglass, L. Wilkens, E. Pantazelou, and F. Moss: *Noise enhancement of information transfer in crayfish mechanoreceptors by stochastic resonance*. Nature **365**, 337 (1993).
- [Dub99] J. L. A. Dubbeldam, B. Krauskopf, and D. Lenstra: *Excitability and coherence resonance in lasers with saturable absorber*. Phys. Rev. E **60**, 6580 (1999).
- [Ein05] A. Einstein: *Über die von der molekular-kinetischen Theorie der Wärme geforderte Bewegung von in ruhenden Flüssigkeiten suspendierten Teilchen*. Ann. Phys. (Leipzig) **17**, 549 (1905).
- [Eng01] K. Engelborghs, T. Luzyanina, and G. Samaey: *DDE-BIFTOOL v. 2.00: a Matlab package for bifurcation analysis of delay differential equations*. Tech. Rep. TW-330, Department of Computer Science, K.U.Leuven, Belgium (2001).
- [Eng02] K. Engelborghs, T. Luzyanina, and D. Roose: *Numerical bifurcation analysis of delay differential equations using DDE-BIFTOOL*. ACM Transactions on Mathematical Software **28**, 1 (2002).
- [Esa70] L. Esaki and R. Tsu: *Superlattice and Negative Differential Conductivity in Semiconductors*. IBM J. Res. Develop. **14**, 61 (1970).
- [Fau83] S. Fauve and F. Heslot: *Stochastic Resonance in a bistable system*. Phys. Lett. **97A**, 5 (1983).
- [Feu00] U. Feudel, A. Neimann, X. Pei, W. Wojtenek, H. A. Braun, M. Huber, and F. Moss: *Homoclinic bifurcations in a Hodgkin-Huxley model of thermally sensitive neurons*. Chaos **10**, 231 (2000).
- [Fie07] B. Fiedler, V. Flunkert, M. Georgi, P. Hövel, and E. Schöll: *Refuting the odd number limitation of time-delayed feedback control*. Phys. Rev. Lett. **98**, 114101 (2007).
- [Fit61] R. FitzHugh: *Impulses and physiological states in theoretical models of nerve membrane*. Biophys. J. **1**, 445 (1961).
- [Flu06] V. Flunkert, P. Hövel, and E. Schöll: *Coherence Resonance - a Mean Field Approach*. Poster at the Workshop Constructive Role of Noise in Complex Systems (2006).

- [Flu07] V. Flunkert and E. Schöll: *Suppressing noise-induced intensity pulsations in semiconductor lasers by means of time-delayed feedback*. Phys. Rev. E **76**, 066202 (2007).
- [Flu07b] V. Flunkert, P. Hövel, and E. Schöll: *private communication* (2007).
- [Fra99] G. Franceschini, S. Bose, and E. Schöll: *Control of chaotic spatiotemporal spiking by time-delay autosynchronisation*. Phys. Rev. E **60**, 5426 (1999).
- [Gam98] L. Gammaitoni, P. Hänggi, P. Jung, and F. Marchesoni: *Stochastic resonance*. Rev. Mod. Phys. **70**, 223 (1998).
- [Gar02] C. W. Gardiner: *Handbook of Stochastic Methods for Physics, Chemistry and the Natural Sciences* (Springer, Berlin, 2002).
- [Gas90] P. Gaspard: *Measurement of the instability rate of a far-from-equilibrium steady state at an infinite period bifurcation*. J. Physical Chem. **94**, 1 (1990).
- [Gar99] J. García-Ojalvo and J. M. Sancho: *Noise in Spatially Extended Systems* (Springer, New York, 1999).
- [Gol03] D. Goldobin, M. G. Rosenblum, and A. Pikovsky: *Controlling oscillator coherence by delayed feedback*. Phys. Rev. E **67**, 061119 (2003).
- [Gra95d] H. T. Grahn, ed.: *Semiconductor Superlattices, Growth and Electronic Properties* (World Scientific, Singapore, 1995).
- [Guc86] J. Guckenheimer and P. Holmes: *Nonlinear Oscillations, Dynamical Systems, and Bifurcations of Vector Fields* (Springer, Berlin, 1986).
- [Hal71] J. K. Hale: *Functional Differential Equations* (Applied Mathematical Sciences Vol. 3, Springer, New York, 1971).
- [Hau06] B. Hauschildt, N. B. Janson, A. G. Balanov, and E. Schöll: *Noise-induced cooperative dynamics and its control in coupled neuron models*. Phys. Rev. E **74**, 051906 (2006).
- [Hin82] J. L. Hindmarsh and R. M. Rose: *A model of the nerve impulse using two first-order differential equations*. Nature **296**, 162 (1982).
- [Hiz05] J. Hizanidis, A. G. Balanov, A. Amann, and E. Schöll: *Noise-induced oscillations and their control in semiconductor superlattices*. Int. J. Bifur. Chaos **16**, 1701 (2006).

- [Hiz06] J. Hizanidis, A. G. Balanov, A. Amann, and E. Schöll: *Noise-induced front motion: signature of a global bifurcation*. Phys. Rev. Lett. **96**, 244104 (2006).
- [Hiz07] J. Hizanidis, R. Aust, and E. Schöll: *Delay-induced multistability near a global bifurcation*. Int. J. Bifur. Chaos (2008). In print (arXiv:nlin/0702002v2).
- [Hiz08] J. Hizanidis and E. Schöll: *Control of noise-induced spatiotemporal patterns in superlattices*. phys. status solidi (c) **5**, 207 (2008).
- [Hod48] A. L. Hodgkin: *The local electric changes associated with repetitive action in a medullated axon*. J. Physiol. **107**, 165 (1948).
- [Hof96] K. Hofbeck, J. Grenzer, E. Schomburg, A. A. Ignatov, K. F. Renk, D. G. Pavel'ev, Y. Koschurinov, B. Melzer, S. Ivanov, S. Schaposchnikov, and P. S. Kop'ev: *High-frequency self-sustained current oscillation in an Esaki-Tsu superlattice monitored via microwave emission*. Phys. Lett. A **218**, 349 (1996).
- [Hoe05] P. Hövel and E. Schöll: *Control of unstable steady states by time-delayed feedback methods*. Phys. Rev. E **72**, 046203 (2005).
- [Hu93a] G. Hu, T. Ditinger, C. Z. Ning, and H. Haken: *Stochastic resonance without external periodic force*. Phys. Rev. Lett. **71**, 807 (1993).
- [Jan03] N. B. Janson, A. G. Balanov, and E. Schöll: *Delayed Feedback as a Means of Control of Noise-Induced Motion*. Phys. Rev. Lett. **93**, 010601 (2004).
- [Jan07] N. B. Janson, A. G. Balanov, and E. Schöll: *Control of noise-induced dynamics*. In *Handbook of Chaos Control*, edited by E. Schöll and H. G. Schuster (Wiley-VCH, Weinheim, 2008). Second completely revised and enlarged edition.
- [Joh28] J. B. Johnson: *Thermal Agitation of Electricity in Conductors*. Phys. Rev. **32**, 97 (1928).
- [Jus97] W. Just, T. Bernard, M. Ostheimer, E. Reibold, and H. Benner: *Mechanism of time-delayed feedback control*. Phys. Rev. Lett. **78**, 203 (1997).
- [Kad98] S. Kádár, J. Wang, and K. Showalter: *Noise-supported travelling waves in sub-excitable media*. Nature **391**, 770 (1998).
- [Kap95a] R. Kapral and K. Showalter, eds.: *Chemical Waves and Patterns* (Kluwer, Dordrecht, 1995).

- [Kas94] J. Kastrup, H. T. Grahn, K. Ploog, F. Pregel, A. Wacker, and E. Schöll: *Multistability of the current-voltage characteristics in doped GaAs-AlAs superlattices*. Appl. Phys. Lett. **65**, 1808 (1994).
- [Kas95] J. Kastrup, R. Klann, H. T. Grahn, K. Ploog, L. L. Bonilla, J. Galán, M. Kindelan, M. Moscoso, and R. Merlin: *Self-oscillations of domains in doped GaAs-AlAs superlattices*. Phys. Rev. B **52**, 13761 (1995).
- [Kie03b] G. Kießlich, A. Wacker, and E. Schöll: *Shot Noise of coupled Semiconductor Quantum Dots*. Phys. Rev. B **68**, 125320 (2003).
- [Kie04] G. Kießlich, H. Sprekeler, A. Wacker, and E. Schöll: *Positive correlations in tunnelling through coupled quantum dots*. Semicond. Sci. Technol. **19**, S37 (2004).
- [Kie05a] G. Kießlich, P. Samuelsson, A. Wacker, and E. Schöll: *Counting statistics and decoherence in coupled quantum dots*. Phys. Rev. B **73**, 033312 (2006).
- [Kie07b] G. Kießlich, E. Schöll, T. Brandes, F. Hohls, and R. J. Haug: *Noise enhancement due to quantum coherence in coupled quantum dots*. Phys. Rev. Lett. **99**, 206602 (2007).
- [Kie07a] G. Kießlich, E. Schöll, F. Hohls, and R. J. Haug: *Coulomb-mediated electron bunching in tunneling through coupled quantum dots*. phys. status solidi (c) **5**, 166 (2008).
- [Kil03] N. Kilic: *Chaotische Dynamik in Halbleiterübergittern und ihre Kontrolle*. Master's thesis, Technische Universität Berlin (2003).
- [Kit95] A. Kittel, J. Parisi, and K. Pyragas: *Delayed feedback control of chaos by self-adapted delay time*. Phys. Lett. A **198**, 433 (1995).
- [Kra40] H. A. Kramers: *Brownian motion in a field of force and the diffusion model of chemical reactions*. Physica **7**, 284 (1940).
- [Kra03a] B. Krauskopf, K. Schneider, J. Sieber, S. Wiczorek, and M. Wolfrum: *Excitability and self-pulsations near homoclinic bifurcations in semiconductor laser systems*. Opt. Commun. **215**, 367 (2003).
- [Kro31] R. d. L. Kronig and W. G. Penney: *Quantum Mechanics of Electrons in Crystal Lattices*. Proc. Royal Soc. A **130**, 499 (1931).
- [Kuz95] Y. A. Kuznetsov: *Elements of Applied Bifurcation Theory* (Springer, New York, 1995).

- [Lan97] P. S. Landa, A. A. Zaikin, M. G. Rosenblum, and J. Kurths: *Control of noise-induced oscillations of a pendulum with a randomly vibrating suspension axis*. Phys. Rev. E **56**, 1465 (1997).
- [Lin99] K. Lin and D. C. Chrzan: *Kinetic Monte Carlo simulation of dislocation dynamics*. Phys. Rev. B **60**, 3799 (1999).
- [Lin99a] B. Lindner and L. Schimansky-Geier: *Analytical approach to the stochastic FitzHugh-Nagumo system and coherence resonance*. Phys. Rev. E **60**, 7270 (1999).
- [Lin03] B. Lindner, A. Longtin, and A. Bulsara: *Analytic expression for rate and CV of a type I neuron driven by white Gaussian noise*. Neural Computation **15**, 1761 (2003).
- [Lin04] B. Lindner, J. García-Ojalvo, A. Neiman, and L. Schimansky-Geier: *Effects of noise in excitable systems*. Phys. Rep. **392**, 321 (2004).
- [Lon97] A. Longtin: *Autonomous stochastic resonance in bursting neurons*. Phys. Rev. E **55**, 868 (1997).
- [Luo98b] K. J. Luo, H. T. Grahn, K. H. Ploog, and L. L. Bonilla: *Explosive Bifurcation to Chaos in Weakly Coupled Semiconductor Superlattices*. Phys. Rev. Lett. **81**, 1290 (1998).
- [Luo99] K. J. Luo, S. W. Teitworth, H. Kostial, and H. T. Grahn: *Controllable bistabilities and bifurcations in a photoexcited GaAs/AlAs superlattice*. Appl. Phys. Lett. **74**, 3845 (1999).
- [Maj07] N. Majer: *Mehrzeitige Rückkopplungskontrolle der resonanten Tunnel-diode unter Rauschen*. Master's thesis (2007).
- [Man91] Y. Manor, C. Koch, and I. Segev: *Effect of geometrical irregularities on propagation delay in axonal trees*. Biophys J **60**, 1424 (1991).
- [Mas02] C. Masoller: *Noise-Induced Resonance in Delayed Feedback Systems*. Phys. Rev. Lett. **88**, 034102 (2002).
- [Mcn88] B. McNamara, K. Wiesenfeld, and R. Rajarshi: *Observation of stochastic resonance in a ring laser*. Phys. Rev. Lett. **60**, 2626 (1988).
- [Mik90] A. S. Mikhailov: *Foundations of Synergetics Vol. I* (Springer, Berlin, 1990).

- [Mor81] C. Morris and H. Lecar: *Voltage oscillations in the barnacle giant muscle fiber*. Biophys. J. **35**, 193 (1981).
- [Nag62] J. Nagumo, S. Arimoto, and S. Yoshizawa.: *An active pulse transmission line simulating nerve axon*. Proc. IRE **50**, 2061 (1962).
- [Nei65] J. Neimark and L. Shilnikov: *A case of generation of periodic motions*. Soviet. Math. Dokl. **6**, 305 (1965).
- [Nei97] A. Neiman, P. I. Saporin, and L. Stone: *Coherence resonance at noisy precursors of bifurcations in nonlinear dynamical systems*. Phys. Rev. E **56**, 270 (1997).
- [Nic81] C. Nicholson and J. D. Phillips: *Ion diffusion modified by tortuosity and volume fraction in the extracellular microenvironment of the rat cerebellum*. J. Physiol. **321**, 225 (1981).
- [Nic81b] C. Nicolis: *Solar variability and stochastic effects on climate*. Solar Physics **74**, 473 (1981).
- [Nyq28] H. Nyquist: *Thermal Agitation of Electric Charge in Conductors*. Phys. Rev. **32**, 110 (1928).
- [Ott90] E. Ott, C. Grebogi, and J. A. Yorke: *Controlling Chaos*. Phys. Rev. Lett. **64**, 1196 (1990).
- [Pat98] M. Patra, G. Schwarz, and E. Schöll: *Bifurcation analysis of stationary and oscillating field domains in semiconductor superlattices with doping fluctuations*. Phys. Rev. B **57**, 1824 (1998).
- [Pei89] J. Peinke, U. Rau, W. Clauss, R. Richter, and J. Parisi: *Critical Dynamics Near the Onset of Spontaneous Oscillations in p-Germanium*. Europhys. Lett. **9**, 743 (1989).
- [Pik97] A. Pikovsky and J. Kurths: *Coherence Resonance in a Noise-Driven Excitable System*. Phys. Rev. Lett. **78**, 775 (1997).
- [Pom05a] J. Pomplun, A. Amann, and E. Schöll: *Mean field approximation of time-delayed feedback control of noise-induced oscillations in the Van der Pol system*. Europhys. Lett. **71**, 366 (2005).
- [Pom07] J. Pomplun, A. G. Balanov, and E. Schöll: *Long-term correlations in stochastic systems with extended time-delayed feedback*. Phys. Rev. E **75**, 040101(R) (2007).

- [Pou03] V. Pouyet and E. R. Brown: *Shot-Noise Reduction in Multiple-Quantum-Well Resonant Tunneling Diodes*. IEEE Transactions on Electron Devices **50**, 1063 (2003).
- [Pra07] T. Prager, H. P. Lerch, L. Schimansky-Geier, and E. Schöll: *Increase of Coherence in Excitable Systems by Delayed Feedback*. J. Phys. A **40**, 11045 (2007).
- [Pre94] F. Prengel, A. Wacker, and E. Schöll: *Simple model for multistability and domain formation in semiconductor superlattices*. Phys. Rev. B **50**, 1705 (1994). Ibid **52**, 11518 (1995).
- [Pyr92] K. Pyragas: *Continuous control of chaos by self-controlling feedback*. Phys. Lett. A **170**, 421 (1992).
- [Rap94] W. J. Rappel and S. H. Strogatz: *Stochastic resonance in an autonomous system with a nonuniform limit cycle*. Phys. Rev. E **50**, 3249 (1994).
- [Rin89] J. Rinzel and G. B. Ermentrout: *Analysis of neural excitability and oscillations*. In *Methods in neuronal modeling*, edited by C. Koch and I. Segev (MIT Press, Cambridge, MA, 1989).
- [Rog01] M. Rogozia, S. W. Teitworth, H. T. Grahn, and K. H. Ploog: *Statistics of the domain-boundary relocation time in semiconductor superlattices*. Phys. Rev. B **64**, 041308 (2001).
- [Rog02a] M. Rogozia, S. W. Teitworth, H. T. Grahn, and K. H. Ploog: *Relocation dynamics of domain boundaries in semiconductor superlattices*. Phys. Rev. B **65**, 205303 (2002).
- [Sag07] F. Sagués, J. M. Sancho, and J. García-Ojalvo: *Spatiotemporal order out of noise*. Rev. Mod. Phys. **79**, 829 (2007).
- [Sch18] W. Schottky: *Über spontane Stromschwankungen in verschiedenen Elektrizitätsleitern*. Ann. Phys. (Leipzig) **57**, 541 (1918).
- [Sch87] E. Schöll: *Nonequilibrium Phase Transitions in Semiconductors* (Springer, Berlin, 1987).
- [Sch96a] G. Schwarz, A. Wacker, F. Prengel, E. Schöll, J. Kastrup, H. T. Grahn, and K. Ploog: *The Influence of imperfections and weak disorder on domain formation in superlattices*. Semicond. Sci. Technol. **11**, 475 (1996).
- [Sch96b] G. Schwarz and E. Schöll: *Field Domains in Semiconductor Superlattices*. phys. status solidi (b) **194**, 351 (1996).

- [Sch99c] H. G. Schuster, ed.: *Handbook of Chaos Control* (Wiley-VCH, Weinheim, 1999).
- [Sch99h] E. Schomburg, R. Scheuerer, S. Brandl, K. F. Renk, D. G. Pavel'ev, Y. Koschurinov, V. M. Ustinov, A. E. Zhukov, A. R. Kovsh, and P. S. Kop'ev: *InGaAs/InAlAs superlattice oscillator at 147 GHz*. *Electronics Letters* **35**, 1491 (1999).
- [Sch01] E. Schöll: *Nonlinear spatio-temporal dynamics and chaos in semiconductors* (Cambridge University Press, Cambridge, 2001). Nonlinear Science Series, Vol. 10.
- [Sch02r] J. Schlesner: *Nichtlineare Oszillationen in Halbleiterübergittern unter zeitverzögerter Rückkopplung*. Master's thesis, Technische Universität Berlin (2002).
- [Sch03a] J. Schlesner, A. Amann, N. B. Janson, W. Just, and E. Schöll: *Self-stabilization of high frequency oscillations in semiconductor superlattices by time-delay autosynchronization*. *Phys. Rev. E* **68**, 066208 (2003).
- [Sch04] E. Schöll: *Pattern formation in semiconductors: control of spatio-temporal dynamics*. *Ann. Phys. (Leipzig)* **13**, 403 (2004). Special Topic Issue, ed. by R. Friedrich, T. Kuhn and S. Linz.
- [Sch03c] E. Schöll: *Nonlinear Dynamics and Pattern Formation in Semiconductor Systems*. In *Collective Dynamics of Nonlinear and Disordered Systems*, edited by G. Radons, W. Just, and W. Häussler, pp. 39–59 (Springer, Berlin, 2005).
- [Sch04b] E. Schöll, A. G. Balanov, N. B. Janson, and A. Neiman: *Controlling stochastic oscillations close to a Hopf bifurcation by time-delayed feedback*. *Stoch. Dyn.* **5**, 281 (2005).
- [Sch06a] S. Schikora, P. Hövel, H. J. Wünsche, E. Schöll, and F. Henneberger: *All-optical noninvasive control of unstable steady states in a semiconductor laser*. *Phys. Rev. Lett.* **97**, 213902 (2006).
- [Sch06c] J. Schlesner, V. Zykov, H. Engel, and E. Schöll: *Stabilization of unstable rigid rotation of spiral waves in excitable media*. *Phys. Rev. E* **74**, 046215 (2006).
- [Sch06] E. Schöll, J. Hizanidis, P. Hövel, and G. Stegemann: *Pattern formation in semiconductors under the influence of time-delayed feedback*

- control and noise*. In *Analysis and control of complex nonlinear processes in physics, chemistry and biology*, edited by L. Schimansky-Geier, B. Fiedler, J. Kurths, and E. Schöll, pp. 135–183 (World Scientific, Singapore, 2007).
- [Sch07] E. Schöll and H. G. Schuster, eds.: *Handbook of Chaos Control* (Wiley-VCH, Weinheim, 2008). Second completely revised and enlarged edition.
- [Sch08a] E. Schöll, N. Majer, and G. Stegemann: *Extended time delayed feedback control of stochastic dynamics in a resonant tunneling diode*. *phys. stat. sol. (c)* **5**, 194 (2008).
- [Sco04] A. Scott, ed.: *Encyclopedia of Nonlinear Science* (Routledge, London, 2005).
- [Set06] G. C. Sethia and A. Sen: *Excitable dynamics in the presence of time delay*. *Phys. Lett. A* **359**, 285 (2006).
- [Shi63] L. Shilnikov: *Some cases of generation of periodic motions from singular trajectories*. *Mat. Sbornik* **61**, 443 (1963).
- [Shi65] L. Shilnikov: *A case of existence of a countable number of periodic motions*. *Math. Dokl.* **6**, 163 (1965).
- [Shi96] Y. H. Shiau and Y. C. Cheng: *Boundary effect induced nonhysteretic transition caused by saddle-node bifurcation on a limit cycle in n-GaAs*. *Solid State Communications* **99**, 305 (1996).
- [Sig89] D. Sigeti and W. Horsthemke: *Pseudo-Regular Oscillations Induced by External Noise*. *J. Stat. Phys.* **54**, 1217 (1989).
- [Sim97] E. Simonotto, M. Riani, C. Seife, M. Roberts, J. Twitty, and F. Moss: *Visual Perception of Stochastic Resonance*. *Phys. Rev. Lett.* **78**, 1186 (1997).
- [Soc94] J. E. S. Socolar, D. W. Sukow, and D. J. Gauthier: *Stabilizing unstable periodic orbits in fast dynamical systems*. *Phys. Rev. E* **50**, 3245 (1994).
- [Son03] W. Song, E. E. Mendez, V. Kuznetsov, and B. Nielsen: *Shot noise in negative-differential-conductance devices*. *Appl. Phys. Lett.* **82**, 1568 (2003).
- [Ste05] G. Stegemann, A. G. Balanov, and E. Schöll: *Noise-induced pattern formation in a semiconductor nanostructure*. *Phys. Rev. E* **71**, 016221 (2005).

- [Ste05a] G. Stegemann, A. G. Balanov, and E. Schöll: *Delayed feedback control of stochastic spatiotemporal dynamics in a resonant tunneling diode*. Phys. Rev. E **73**, 016203 (2006).
- [Str63] R. L. Stratonovich: *Topics in the Theory of Random Noise*, vol. 1 (Gordon and Breach, New York, 1963).
- [Tas02] P. Tass: *Effective desynchronization with bipolar double-pulse stimulation*. Phys. Rev. E **66**, 036226 (2002).
- [Tro06] V. Z. Tronciu, H. J. Wünsche, M. Wolfrum, and M. Radziunas: *Semiconductor Laser under Resonant Feedback from a Fabry-Perot: Stability of Continuous-Wave Operation*. Phys. Rev. E **73**, 046205 (2006).
- [Unk03] J. Unkelbach, A. Amann, W. Just, and E. Schöll: *Time-delay autosynchronization of the spatiotemporal dynamics in resonant tunneling diodes*. Phys. Rev. E **68**, 026204 (2003).
- [Ush05] O. V. Ushakov, H. J. Wünsche, F. Henneberger, I. A. Khovanov, L. Schimansky-Geier, and M. A. Zaks: *Coherence Resonance Near a Hopf Bifurcation*. Phys. Rev. Lett. **95**, 123903 (2005).
- [Wac95c] A. Wacker, G. Schwarz, F. Prengel, E. Schöll, J. Kastrup, and H. T. Grahn: *Probing growth-related disorder by high-field transport in semiconductor superlattices*. Phys. Rev. B **52**, 13788 (1995).
- [Wac98] A. Wacker: *Vertical transport and domain formation in multiple quantum wells*. In *Theory of Transport Properties of Semiconductor Nanostructures*, edited by E. Schöll, chap. 10 (Chapman and Hall, London, 1998).
- [Wac02] A. Wacker: *Semiconductor Superlattices: A model system for nonlinear transport*. Phys. Rep. **357**, 1 (2002).
- [Wan37] G. H. Wannier: *The Structure of Electronic Excitation Levels in Insulating Crystals*. Phys. Rev. **52**, 191 (1937).
- [Wan00] W. Wang, I. Z. Kiss, and J. L. Hudson: *Experiments on arrays of globally coupled chaotic electrochemical oscillators: Synchronization and clustering*. Chaos **10**, 248 (2000).
- [Wie02] S. Wiczorek, B. Krauskopf, and D. Lenstra: *Multipulse excitability in a semiconductor laser with optical injection*. Phys. Rev. Lett. **88**, 063901 (2002).
- [Wig88] S. Wiggins: *Global Bifurcations and Chaos* (Springer, New York, 1988).

-
- [Xu04] J. Xu and P. Yu: *Delay-induced bifurcations in a nonautonomous system with delayed velocity feedbacks*. Int. J. Bifur. Chaos **14**, 2777 (2004).
- [Zeu96a] S. Zeuner, S. J. Allen, K. D. Maranowski, and A. C. Gossard: *Photon-assisted tunneling in GaAs/AlGaAs superlattices up to room temperature*. Appl. Phys. Lett. **69**, 2689 (1996).
- [Zha96] Y. Zhang, J. Kastrup, R. Klann, K. H. Ploog, and H. T. Grahn: *Synchronization and Chaos Induced by Resonant Tunneling in GaAs/AlAs Superlattices*. Phys. Rev. Lett. **77**, 3001 (1996).
- [Zha00] X. G. Zhao and D. W. Hone: *Zener transitions between dissipative Bloch bands. II Current response at finite temperature*. Phys. Rev. B **62**, 5010 (2000).